BIORECOVERY OF RARE EARTH ELEMENTS AND CRITICAL MINERALS VIA *GLUCONOBACTER OXYDANS*

by

Kendall Rhea Kessler

A thesis in partial fulfillment
of the requirements for the degree

of

Master of Science

in

Bioengineering

MONTANA STATE UNIVERSITY
Bozeman, Montana

May 2024

DEDICATION

I dedicate this thesis to my wonderful family who have provided a great deal of love and support throughout the entirety of my time in this program. I would not be the person I am today without them.

ACKNOWLEDGEMENTS

Thank you to my committee members Dr. Ryan Anderson, Dr. Ross Carlson, and Dr. David Reed who have provided a great amount of support throughout the entirety of my Master's program. I would like to acknowledge the College of Engineering for providing the funds to send me to the Idaho National Laboratory for a summer internship, as well as the Critical Minerals Institute at INL for hosting me.

I would also like to thank the Geology/Environmental Science Department, including David Mogk, Colin Shaw, and Madison Myers for providing their guidance, equipment, and expertise. Thank you to ICAL and their staff Sara Zacher and Bret Davis. Lastly, thank you to the Carlson lab.

TABLE OF CONTENTS

TABLE OF CONTENTS CONTINUED

TABLE OF CONTENTS CONTINUED

LIST OF TABLES

Table Page

LIST OF TABLES CONTINUED

Table Page

LIST OF TABLES CONTINUED

Table Page

LIST OF TABLES CONTINUED

Table Page

LIST OF TABLES CONTINUED

Table Page

LIST OF FIGURES

Figure Page

LIST OF FIGURES CONTINUED

Figure Page

LIST OF FIGURES CONTINUED

Figure Page

LIST OF FIGURES CONTINUED

Figure Page

LIST OF FIGURES CONTINUED

Figure Page

LIST OF FIGURES CONTINUED

Figure Page

LIST OF FIGURES CONTINUED

Figure Page

ABSTRACT

The depletion of high-grade ore deposits, accumulation of electronic waste, and the geopolitical challenges in sourcing critical materials have emphasized the need for sustainable metal recovery methods and recycling efforts in the United States. Conventional metal recovery approaches, including pyrometallurgy and hydrometallurgy, are not only environmentally unsustainable but also inadequate for the retrieval of metals from low-grade deposits. Biorecovery, defined by microorganism-mediated metal recovery, provides an advantageous alternative to traditional recovery methods due to increased sustainability, lower operational costs, and high efficiencies observed for the recovery of low-grade feedstocks. This study investigates the potential of bioleaching as an eco-friendly alternative in the recycling of two distinct waste feedstocks: magnetic swarf and lithium-ion batteries (LIBs). Cultivation of *Gluconobacter oxydans* was investigated under varying growth medium compositions, wherein increased concentrations of yeast extract were substituted for KH_2PO_4, to determine the subsequent impact on the base metal and rare earth element recovery through the application of the cell-free biolixiviant. This substitution resulted in increased growth yields and enhanced recovery with respect to magnetic swarf, whereas negligible improvement was observed for LIBs. Biorecovery has also been demonstrated for the recovery of metals from ore, where yields are a function of comminution and concentration efficiencies. Typical compressive comminution practices account for the largest proportion of energy expenditures in a mining process. Transcritical CO_2 (tCO_2) comminution, wherein ore is fractured through overcoming a rock's tensile strength, was examined to determine whether physical differences in particle generation were present as compared to traditional fracture techniques. An ore deposit in British Columbia, rich in a nickel-iron alloy mineral phase called awaruite, was examined through scanning electron microscopy, backscatter electron imaging, and energy dispersive spectroscopy to determine the impact of comminution method on awaruite recovery. Image processing was used to investigate shape factors for the individual particles. Preliminary evidence indicates despite a lack of distinct particle differences, tCO_2 comminution resulted in increased liberation and recovery of awaruite ore. Abiotic leaching studies were conducted to determine whether the method of comminution impacted leaching efficiencies. Although samples could not be quantitatively measured, initial qualitative results indicate tCO_2 comminution provides increased yields.

INTRODUCTION

Critical minerals, as defined in Executive Order 13817, are sourced from vulnerable supply chains and are essential for manufacturing, with their absence posing significant consequences for the United States' economy and national security [1]. The United States' growing reliance on critical minerals has been further compounded by rapid industrialization and increasing efforts towards sustainable energy technologies, where rare earth elements (REEs) play a prominent role. The concentration of mining and production of critical minerals, including REEs, in a few countries globally exposes the United States to supply risks associated with geopolitical tensions and foreign reliance [1]. To address these challenges, a large emphasis has been placed on the exploration of domestic low-grade deposits and the promotion of recycling electronic waste [1].

Biorecovery has gained interest due to increased sustainability and its promising advantage toward low-grade ore recovery [2] and the recycling of waste feedstocks [3]. Conventional metal recovery techniques, including pyrometallurgy and hydrometallurgy, require high energy expenditures and high solvent consumption, often inorganic acids and water [3]. Consequently, these techniques are both unsuitable for low-grade recovery resulting from high operational costs, as well as unsustainable due to hazardous gas emissions and wastewater treatment requirements [4].

Bioleaching is defined as the mobilization of metal cations by biologically mediated complexation and oxidation processes [5]. Although a variety of organisms have been applied toward bioleaching processes, the current study implements the gram-negative, strictly aerobic bacteria *Gluconobacter oxydans* to explore its efficacy in the recycling of two distinct waste

feedstocks. The presence of membrane-bound dehydrogenases, wherein glucose is directly oxidized into gluconic acid, makes *G. oxydans* a viable candidate for bioleaching applications [6]. This organism has demonstrated efficient recovery from NiMH batteries [7], blast furnace slag [8], cracking catalysts [9], and lithium-ion batteries [3].

The current study also delves into the optimization of mining processes to further enhance sustainability. The high energy expenditures often associated with the mining industry, specifically in comminution or rock fracture steps, can be improved to make the overall process more sustainable [10]. Transcritical CO_2 comminution has demonstrated an ability to fracture rock through overcoming tensile forces in the lattice structure, thus substantially decreasing the energy input required [10]. The implementation of this technology could increase the overall sustainability of mining processes, but it is currently unknown how downstream recovery process would be impacted. A recently discovered deposit in British Columbia hosts awaruite, a nickel iron alloy [11]. Despite the lack of a current awaruite processing operation, the high proportion of nickel contained in the awaruite ore makes this deposit attractive for future nickel recovery [11].

This thesis aims to investigate how the manipulation of culture medium composition impacts *G. oxydans* growth, metabolite production, as well as subsequent bioleaching efficiencies from the generated biolixiviant. The implementation of a non-contact approach, wherein cell-free supernatant is applied for bioleaching processes, allowed for the independent examination of metabolite production and leaching yields. The microbial culture medium was adjusted through variations in phosphorus source, including KH_2PO_4 and YE concentrations. The biolixiviant was then applied to two distinct waste feedstocks, lithium-ion batteries and magnetic

swarf, following microbial cultivation under the varying growth conditions. The leaching yields were assessed to determine how growth conditions ultimately impacted subsequent metal solubilization efficiencies.

Additionally, comminution was investigated as a means of further increasing sustainability. Awaruite ore, supplied from the Baptiste deposit, was fractured through traditional comminution, including crushing and grinding processes, and through tCO_2 comminution. Scanning electron microscopy was used to investigate how the method of comminution impacted concentration efforts, achieved through magnetic separation. Abiotic leaching studies were then performed on the different comminution samples to determine the viability of leaching and ultimately determine the impact of comminution method on downstream metal solubilization efforts.

LITERATURE REVIEW

Critical Materials

In September of 2020, the U.S. Geological Survey (USGS) released a report investigating the country's reliance on foreign adversaries with a focus on distribution potential of critical minerals. Critical minerals, as defined in Executive Order 13817, describes a nonfuel mineral or mineral material that is 1) essential to the economic and national security of the United States, 2) from a supply chain that is vulnerable to disruption, and 3) serves an essential function in the manufacturing of a product, the absence of which would have substantial consequences for the U.S. economy or national security. Since the 1990s, the U.S. has become increasingly reliant on the import of critical minerals to meet domestic demands [1]. Although the reliance has extended over the last few decades, the recent COVID-19 pandemic exposed the United States' dependence on the import of these crucial materials and the volatility of the supply chain.

Net import reliance (NIR) is a metric used to determine the U.S. reliability on foreign sources for mineral commodities, with a score of 100 indicating the consumption of a commodity necessitates foreign sources and a complete lack of domestic production, ultimately leading to foreign reliance. Notably, the number of mineral commodities with at least a 25% NIR has increased from 21 to 58 mineral commodities from 1954 to 2019, respectively [1]. Contributing to an increase in NIR scores is the lack of domestic infrastructure for downstream processing. Often native ore and unprocessed minerals are sent abroad for downstream processing and metal purification due to this lack of domestic infrastructure [1]. Another primary factor compounding this substantial increase in NIR is the rapid industrialization and a shift towards renewable energy.

The implementation of renewable energy has resulted in a considerable increase in the demand for heavy metals. Some of these key elements include rare earth elements (REEs) due to their unique properties, including but not limited to luminescence, ferromagnetism, and superconductivity [12]. REEs are widely implemented in electronic devices and a variety of low-carbon technologies such as electric vehicles and wind turbine generators. As global initiatives push towards a carbon neutral future, the use of these low-carbon technologies is only expected to expand. Although REEs are distributed globally, China accounts for the largest reserves, as well as the greatest proportion of global production with an 80% stake [13]. Alternatively, Russia possesses large proportions of global iron, manganese, chromium, nickel, platinum, titanium, and copper, among other strategic metals and minerals [12]. Electronic waste is the fastest growing waste stream in the world, with 11.3 metric tons generated in 2016 just by the United States [14]. The recycling of these wastes would provide a self-sustained circular economy of critical minerals, wherein the reliance on foreign countries would substantially decrease.

An increase in demand, as well as depletion of high-grade resources and supply constraints, necessitates the investigation into both recovery from low-grade deposits and the recycling of industrial wastes, with the primary focus on feedstocks sourced within the United States.

Traditional Metal Recovery Techniques

Extractive metallurgy operations often include pyrometallurgy, hydrometallurgy, or a mix of the two. Pyrometallurgical processes involve the imposition of high temperature conditions, ranging between 800 to 1200°C, to recover metals from the feedstock, or metal containing material [15]. The induction of high temperatures functions to convert the metals from the solid

phase to a liquid phase, allowing for their subsequent recovery. This refinement method is widely adopted and accounts for 16.5 million metric tons of copper, 1812 million metric tons of crude steel, and 4.8 million metric tons of lead as of 2018 [16]. The two most widely used smelting methods include flash smelting and bath smelting, wherein flash smelting is often more economically feasible [16]. Flash smelting is defined by the use of oxygenated air, which is used to promote autogenous conditions [16]. Alternatively, bath smelting refers to a molten pool containing both the slag and matte phases [16]. Although widely implemented, these processes suffer from high energy consumption and the emission of hazardous gases, including dioxin and furans, resulting in high amounts of environmental pollution [17]. As a result of the high operational costs associated with pyrometallurgy, this method is often reserved for the application toward high-grade ore [4].

Hydrometallurgy involves the application of aqueous solutions to ore bodies for metal recovery [18]. The process is often simple, efficient, and inexpensive [19]. There are three general steps in this process including extraction, concentration, and recovery [20]. Hydrometallurgical reactions can proceed via one or several basic reactions including precipitation, hydrolysis, electrochemical, conversion, complexation, solvation, and ionic dissociation [20]. Metal recovery is ultimately achieved through electrolysis, gaseous reduction, and precipitation to yield the final high value product [20]. Leaching reagents often include inorganic acids, organic acids, alkaline solutions, reductants, oxidants, and complexing agents [21]. Although hydrometallurgy is less energy intensive than pyrometallurgy, it often involves high accumulations of acidic wastewater that require treatment prior to environmental release [22].

Biorecovery

Motivation for Biorecovery

As high-grade ore deposits become scarcer, metal recovery necessitates investigation into viable methods to recover critical minerals from low-grade ore deposits, mine processing wastes, and through the recycling of waste products. Biorecovery, also referred to interchangeably as bioleaching or biomining in the literature, is an alternative to traditional metal recovery techniques. Bioleaching describes cell mediated metal solubilization, a bio-based method of hydrometallurgy. Microbial cultures either directly interact with the metal-containing feedstock and/or excrete metabolic intermediates capable of recovering the elements of interest through metal solubilization. Biological methods of metal extraction can be both more cost-effective and environmentally benign than traditional physiochemical and pyrometallurgical methods [23].

Traditionally used metal recovery techniques have several disadvantages including high acid/base consumption, high temperature requirements resulting in process complexity, and high rates of energy consumption [23]. Treatment of low-grade ore by pyrometallurgy is not suitable due to the large amount of energy required to melt the gangue minerals. Alternatively, bioleaching can employ microbially produced organic acids to solubilize metals from the feedstock. Organic acids, opposed to typically utilized inorganic acids, are more biodegradable and have less severe environmental repercussions. Table 1 compares organic acids and inorganic acids, often associated with hydrometallurgical practices.

Table 1. Comparison of the characteristics of organic and inorganic acids in leaching processes, adopted from [4].

Parameter	Organic Acids (OA)	Inorganic acids (IA)
Reuse potential	Can be reused more than once in metal recovery processes	Cannot be reused in metal recovery processes
Emissions	Lower emission of hazardous gases	High emission of sulfur, chloride, and nitrous oxides
Biodegradability	Biodegradable	Non-biodegradable
Equipment corrosion	Delayed corrosion, expanding the lifetime of equipment	Quickly corrodes equipment
Cost	More costly with respect to IA	Lower cost
Function	Solely acts as leaching agent thus separation and purification required	Solely acts as leaching agent thus separation and purification required
Process manipulation	Less risky manipulation during the process	Risky manipulation during the process
Environmental impact	Serves for soil nutrient acquisition and mineral weathering; therefore, wastewater treatment is not required prior to environmental release	Leads to high water and chemical consumption

The utilization of both inorganic and organic acids requires further processing to separate and purify the metals once they have been solubilized from the feedstock. Although organic acids are often costlier than inorganic acids, this cost is offset by the decreased environmental impacts [4]. For example, the implementation of bioleaching processes in the recovery of spent FCC catalysts was reported to profit $855,000 per year as compared to reported negative profits of -$7.1M, -$7.75M, and -$5.46M per year when H_2SO_4 is utilized [24]. Inorganic acids result in hazardous wastewater streams that require treatment prior to environmental release. Ultimately, because of the decreased environmental impact exhibited with bioleaching practices, it is viewed as a viable alternative for metal recovery.

Theory of Biorecovery

Bioleaching describes the process of metal solubilization through microbial action, wherein a microorganism produces and excretes metabolites, often organic acids, capable of extracting the metals. Alternatively, biooxidation involves the release of metals in sulfidic ores through the oxidation of iron and sulfur [2]. The umbrella term bioleaching is often used to describe both processes. Bioleaching can be divided into two primary subsets, chemolithoautotrophic and heterotrophic bioleaching. The choice of feedstock often dictates the type of bioleaching, thus determining the types of organisms suitable for leaching. Chemolithoautotrophic bioleaching requires sulfidic minerals whereas heterotrophic bioleaching is often implemented on non-sulfide containing feedstocks [2].

Chemolithoautotrophic bioleaching describes cell-mediated leaching using chemolithoautotrophic archaea or bacteria. These are archaea or gram-negative bacteria that utilize atmospheric CO_2 as their source of carbon and derive energy from the oxidation of reduced or partially reduced sulfur compounds [2]. The sulfur compounds can include sulfides, elemental sulfur, and thiosulfate with sulfate being the final oxidation product [2]. The organisms applied for chemolithoautotrophic processes are described in more detail in the following sections.

Heterotrophic bioleaching incorporates the use of heterotrophic bacteria, archaea, and/or fungi that produce metabolic byproducts capable of leaching metals from the feedstock [2]. The supplementation of organic carbon in the forms of sugars, alcohols, and hydrocarbons allow heterotrophic bacteria to produce and excrete organic acids [2]. These organic acids leach metals from the feedstock, making heterotrophic bioleaching applicable to non-sulfidic ores and waste products.

Microbial Leaching Techniques

Bioleaching can be accomplished through one of the following methods, including one-step, two-step, or spent culture media. One-step bioleaching is the introduction of both the feedstock and cell culture, added simultaneously to the growth medium. Two-step bioleaching is the process of allowing the microbial culture to establish growth prior to the introduction of the feedstock. This method provides time for adequate growth and biolixiviant, or leaching solution, production prior to the introduction of the feedstock, which may inhibit growth. Both one-step and two-step bioleaching can be simply described as contact, or direct, bioleaching. Alternatively, non-contact or spent culture bioleaching is the use of cell-free biolixiviant to achieve metal solubilization [25].

There are advantages and disadvantages to each leaching method. Contact bioleaching can inhibit microbial growth and metabolic activity due to the presence of potentially toxic compounds present in the feedstock. As metals are solubilized, the concentration of toxic metals increases and can hamper the organisms' growth as well as inhibit the production of valuable leaching products [25]. Often at the cost of heightened metabolite production, contact bioleaching is more easily applied toward large scale applications due to the limited number of processing steps. The use of a cell-free biolixiviant can increase the processing costs, requiring multiple units for cultivation and leaching [2]. Although processing costs can be increased, depending on the organism the leachate concentrations may be increased. Ultimately, the implementation of a non-contact approach, where the microbial cultivation and leaching steps occur independently, allows for the optimization of both metabolite production and leaching processes thus increasing the potential for higher metal recovery yields.

Leaching techniques can be divided by the working volume of the process. Laboratory, or bench scale, refers to volumes <0.01 m^3, pilot scale refers to volumes <10 m^3, and industrial scale refers to volumes >10 m^3 [26].

Laboratory-Scale and Pilot-Plant Bioleaching Techniques

Percolator leaching was the first implemented bacterial leaching technique [2]. The percolator consists of a vertical glass tube. At the bottom of the tube, a sieve plate is filled with the solid particles. The ore is flooded with the nutrients inoculated with bacteria. Compressed sterile air is pumped through the bottom of the system to provide aeration. Liquid samples are taken in intervals to monitor the progress of the leaching process [2]. Due to poor oxygen supply and surface interactions resulting from poor mixing, percolator leaching is not very efficient and typically exhibited lengthy leaching times, lasting up to 100-300 days [2].

Submerged leaching uses fine particles (<100 μm) suspended in the leaching liquid. The medium is stirred or shaken to keep the medium in motion [2]. The suspension can be carried out in Erlenmeyer flasks or a bioreactor. Higher rates of aeration along with more accurate monitoring and control of favorable growth parameters makes the reaction times and metal extraction yields of submerged leaching substantially greater than percolator leaching [2]. The application of submerged bioleaching resulted in leaching times of around 50 days, as compared to the 100-300 required for percolator leaching [2]. One of the primary constraints in these systems is the pulp density, or the amount of solids relative to the volume of lixiviant. These systems are often limited to a pulp density of 20%, wherein application of greater amounts results in inefficient gas transfer and an induction of increased shear forces on the cells [27]. A combination of pulp density limitations as well as higher capital and operational costs than heap

reactors has resulted in the restriction of stirred tank reactors towards high-value concentrates [27].

Column leaching operates under the same principles as percolator leaching and is often used to model dump or heap leaching. There is versatility of the column material, depending on the application. The column can be constructed of glass, plastic, lined concrete, or steel. The capacity of column leaching is greater than both percolator and submerged leaching, ranging between a few kilograms to a few tons [2]. The column system can be outfitted with various monitoring devices, including temperature, pH, humidity, oxygen, or carbon dioxide. These devices can be located throughout the column, increasing the versatility of the system. The data collected from these devices can provide key information on the optimization of heap and dump leaching [2]. Bioreactors and columns enable batch-wise, semi-continuous or continuous addition of the substrate and removal of the leached metals [5].

Industrial-Scale Leaching Techniques

Bioleaching has been applied at the industrial scale for low-grade ores, consisting of metal concentration lower than 0.5% (w/w) [2]. The main industrial scale orientations include dump leaching, heap leaching, and in-situ leaching.

Dump leaching is the oldest of the industrial processes. The material is piled or "dumped," with the top of the pile sprinkled continuously or flooded temporarily with lixiviant. Depending on the composition of the material, the lixiviant can be water, acidified water, or acid ferric sulfate solution from other leaching operations on the same mining property. The lixiviant is recirculated after passing through an oxidation basin where the bacteria and ferric iron are regenerated [2].

Heap leaching is the simplest bioleaching process. In heap leaching, the material is piled, and water is allowed to trickle through the heap. The runoff is collected, consisting largely of the leachate, and recirculated. The recirculation allows for slower bioleaching processes to be conducted. The process of heap leaching is very similar to dump leaching, but pipes can be placed strategically to provide deeper portions of the heap with enough oxygen [2]. Table 2 demonstrates some current commercial heap applications for copper extraction. Heap bioleaching systems are cheap to construct and are often suitable for lower-grade ore [27], adding benefit towards the recovery of minerals that otherwise would be too expensive to extract.

Table 2. Representation of commercial copper and gold concentrate bioleaching operations. Adapted from [28].

Commercial copper bioheap plants		
Plant and Location	**Size (t/day)**	**Years in operation**
Lo Aguirre, Chile	16,000	1980-1996
Gunpowder's Mammoth Mine, Australia	1.2 M	1991-Present
Mt. Leyshon, Australia	1,370	1992-1997
Cerro Colorado, Chile	16,000	1993-Present
Girilambone, Australia	2,000	1993-Present
Ivan-Zar, Chile	1,500	1994-Present
Quebrada Blanca, Chile	17,300	1994-Present
Adacollo, Chile	10,000	1996-Present
Dos Amigo, Chile	3,000	1996-Present
Cerro Verde, Peru	15,000	1996-Present
Zalidvar, Chile	20,000	1998-Present
S&K Copper Project, Myanmar	15,000	1998-Present

In-situ leaching is typically performed in abandoned mines, where the ore deposits are not economically viable for further processing due to their low-grade. This was common in the

1960s for the application toward industrial-scale uranium recovery [27]. Uranium recovery was performed through the spraying of the walls with acid mine drainage and in-situ irrigation of fractured underground ore deposits [27].

Tank leaching is the most efficient bioleaching process, although it is more expensive to construct and operate. Tank leaching set-ups mimic submerged leaching, but at greater volumes [2].

Mechanisms of Bioleaching

There are three main mechanisms that control bioproduct-mediated metal recovery. These include redoxolysis, acidolysis, and complexolysis. Either one or several of these mechanisms can work to solubilize insoluble metals from the feedstock.

Redoxolysis

Redoxolysis results from the microorganisms production of compounds that regulate the oxidation potential of the solution [2]. Fe^{3+} is the most common redoxolysis agents in leaching systems. The production of Fe^{3+} by iron oxidizers, for example *Acidothiobacillus*, is reduced through the leaching reactions to Fe^{2+} and thus reoxidized to Fe^{3+} by the organism [2]. This reaction is cyclic. The presence of Fe^{3+} acts as an oxidizing agent, oxidizing metals resulting in their solubilization [2]. Redoxolysis is most often observed with chemoautotrophic bioleaching practices. It has been noted that this reaction may be inhibited under acidic conditions [29].

Acidolysis

Acidolysis is one of the dominant mechanisms of heterotrophic bioleaching. Acidolysis is proton-promoted dissolution of metals. The presence of organic acids, excreted by the

microorganisms, results in a drop of pH. Dissociation of the organic acids provides protons capable of participating in acidolysis [4]. Meanwhile, anions participate in complexolysis [4]. The release of protons into the leaching medium and around the surface of the metallic compound contribute to the metal solubilization. In the presence of water, the protons weaken the metal-ion bond resulting in the solubilization of the metal. Acidolysis is most successful when metal ion-organic acid bonds are stronger than those of the metal ions and solid particles from the matrix. Solubilization occurs via the protonation of the metal compounds. Protonation makes the metal less available to the metal cation, thus promoting dissolution. This process is often considered one of the most important of heterotrophic bioleaching. An example of the dissociation of an organic acid, gluconic acid, is represented in Equation 1. The availability of a proton allows the solubilization of a metal contained in the feedstock as a metal oxide (Eq 2).

$$C_6H_{12}O_7 \rightarrow C_6H_{11}O_7^- + H^+ \quad (1)$$

$$MeO + 2H^+ \rightarrow Me^{2+} + H_2O \quad (2)$$

MeO represents a metal oxide.

Complexolysis

The complexolysis mechanism relies on chelation of organic acids with the metals of interest. Chelation is a reversible reaction, thus the solution pH and the stability constants of the metal-organic acid chelates impacts the solubilization potential and effectiveness of complexation driven metal recovery [4]. When an organic acid dissociates, the proton participates in acidolysis driven solubilization, whereas the anion is available for chelation. When the bonds between the metal ions and the organic acid ligands are stronger than the lattice bonds between the metal ions within the solid structure, the metal can successfully be leached

[30]. An example of the complexolysis reaction resulting from gluconic acid ($C_6H_{12}O_7$) is represented in Equation 3.

$$n[C_6H_{11}O_7^-] + M^{n+} \rightarrow M[C_6H_{11}O_7]_n \quad (3)$$

Microorganisms

The choice of microorganism is governed chiefly by the feedstock. Although chemolithoautotrophic organisms are commonly implemented in the bioleaching of sulfidic minerals, the addition of a reducing agent can promote their use in the biorecovery of non-sulfidic minerals.

Chemolithoautotrophic Archaea

Chemolithoautotrophic bioleaching describes the cell-mediated leaching using chemolithoautotrophic bacteria or archaea. Chemolithoautotrophic bacteria are gram-negative bacteria that utilize atmospheric CO_2 as their source of carbon and derive energy from the oxidation of reduced or partially reduced iron or sulfur compounds. The sulfur compounds can include sulfides, elemental sulfur, and thiosulfate with sulfate being the final oxidation product [2]. The genus of *Thiobacillus* is the most widely implemented group of microorganisms used for bioleaching processes [2]. Two of the most important organisms composed within this genus are *Acidithiobacillus ferrooxidans* and *Acidithiobacillus thiooxidans*. Their capacity to thrive under acidic conditions is beneficial because solubilization of metals increases as the pH decreases [2]. *A. thiooxidans* rapidly oxidizes sulfur to generate sulfuric acid. The production of sulfuric acid results in further decomposition of the feedstock and contributes to the solubilization of the metals as sulfate complexes. Due to the generation of H_2SO_4, which can lead to the production of

large volumes of acidic wastewater, the wastewater requires treatment prior to release into the environment.

A. ferrooxidans, although having a much slower rate of oxidation of elemental sulfur, differs from all other thiobacilli through its capability to use ferrous iron as a final electron acceptor [2]. The utilization of this organism broadens chemolithoautotrophic application to feedstocks bearing iron. A majority of the chemolithoautotrophic bacteria exhibit a high tolerance to metal toxicity, making them viable candidates for contact bioleaching [25].

Alternatively, some archaeal species are known to thrive in bioleaching environments [31]. Archaea utilization can be distinguished by microbial temperature preferences [31]. Under moderate to slightly increased temperatures (< 55 ºC), members of the *Thermoplasmatales* genera, including *Ferroplasma*, *Acidiplasma*, and *Cuniculiplasma*, are relevant to bioleaching applications [31]. These organisms, although not strictly chemolithoautotrophic, are able to oxidize iron. They are classified as mixotrophic archaea due to the requirement of organic carbon supplementation to facilitate growth [31]. A group of extremely thermophilic sulfur and iron oxidizers have been demonstrated as effective under high temperature (> 60 ºC) bioleaching applications. The dominant genera for these applications include *Sulfolobus*, *Sulfuracidifex*, *Acidianus*, *Metallosphaera*, and *Sulfurisphaera* [31].

Heterotrophic Bacteria

Heterotrophic bacteria require supplementation of carbon such as sugars, alcohols, and hydrocarbons for their source of carbon and energy [2]. Heterotrophic bacteria do not benefit from metal leaching, and often exhibit higher metal toxicity [2]. As a result, often 2-step or non-contact bioleaching is applied to optimize microbial metabolite production and therefore

subsequent leaching efficiencies. The applications of these organisms are often non-sulfidic containing material, where chemolithoautrophic organisms would require supplementation of sulfur or iron.

Some heterotrophic bacteria that have been used for bioleaching applications include *Pseudomonas putida*, *Acetobacter methanolicus*, *Acidiphilium cryptum*, and *Gluconobacter oxyans* [25]. Members of the genus *Bacillus* are considered to be the most effective for metal solubilization [2]. Table 3 demonstrates the primary organic acids produced for various heterotrophic bacterial species. Ultimately, the microbial cultivation conditions can be optimized primarily through medium composition to promote increased organic acid production.

Table 3. Organic acid production by different bacterial organism during fermentation (bacteria).

Microorganism	**Organic acid**	**Reference**
Pseudomonas putida	Citric acid, gluconic acid	[26]
Gluconobacter oxydans	Gluconic acid, citric acid, acetic acid, xylonic acid	[32]
Arthrobacter sp.	Formic acid, acetic acid, oxalic acid, malonic acid, citric acid, pthalic acid	[33]
Bacillus megaterium	Citric acid	[26]

Heterotrophic Fungi

The utilization of fungal species in bioleaching offers several advantages, such as shorter lag phases, increased tolerance to heavy metals, faster leaching rates, and the capacity to grow in acidic or alkaline environments [25]. Various fungal species, including *Aspergillus niger*, *Aspergillus tubingensis*, *Penicillium simplicissimum*, *Penicillium chrysogenum,* and *Candida bombicola*, have been employed for metal extraction. Notably, *A. niger* is favored for bioleaching applications due to its simplistic growth and harvesting process, accompanied with

higher efficiencies [25]. Sucrose and glucose are often used as the primary carbon and energy source for fungal bioleaching [25]. Through the Kreb's cycle or glycolysis pathway, a variety of organic acids, mainly citric, oxalic, malic, fumaric, succinic, lactic, and pyruvic acids are produced [25]. Table 4 summarizes the primary organic acids produced by fungal species employed in bioleaching processes. Similar to heterotrophic bacteria, heterotrophic fungal species require the supplementation of organic carbon to promote both growth and organic acid production [34].

Table 4. Organic acid production by different organisms through fermentation (fungi).

Microorganism	**Organic acid**	**Reference**
Aspergillus spp.	Oxalic acid, citric acid	[35]
Aspergillus niger	Oxalic acid, citric acid, gluconic acid	[36]
Fusarium spp.	Oxalic acid, malic acid, pyruvic acid, oxaloacetic acid	[37]
Streptomyces spp.	Formic acid, acetic acid, oxalic acid, malonic acid, citric acid, phthalic acid	[33]
Penicillium spp.	Citrate, oxalate, gluconate	[26]

Bioleaching has been demonstrated on various feedstocks using a variety of organisms. Table 5 illustrates several examples of biorecovery applications utilizing different organisms, leaching conditions, and feedstocks to demonstrate the versatility of biorecovery processes.

Table 5. Applications of bioleaching to different feedstocks of varying elemental compositions using various organisms and conditions.

Feedstock	Organism(s)	Leaching agent (mM)	Contact/Non contact	Conditions	Elements Recovered (%)	References
Stone coal	Mixed aerobic sludge collected from Bejing Gaobeidian Wastewater Treatment Plant	Not reported	Contact	5 mL sludge 2% (w/v) 30 days 22°C	5.43% V	[38]
Calamine (Zi) Garnierite (Ni)	*Aspergillus niger.*	4-8 mM Citric 2-4 mM Oxalic	Contact	5% (w/v) 30°C 200 RPM 15 days	62% Zi 78% Ni	[39]
			Non contact	5% (w/v) 30°C 200 RPM 15 days	54% Zi 83% Ni	
Fluid catalytic cracking catalyst	*Aspergillus niger*	98 mM Citric 34 mM Gluconic 8 mM Oxalic	Contact	60°C 21 days 1% (w/v)	55% V 16.5% Ni	[40]
		21 mM Citric 43 mM Gluconic 11 mM Oxalic	Non-contact	60°C 5 days 1% (w/v)	18% V 4.7% Ni	
Nickel laterite	*Bacillus subtilis*	Not reported	Contact	30oC 7 days 100 RPM 0.25-1% (w/v)	Non heat-treated ore 8.1% Ni	[41]
					Heat-treated ore 26.4% Ni	

Parameters Influencing Bioleaching Efficiencies

There are several parameters that can impact both the microbial cultivation and physiochemical properties that further impact overall bioleaching yields [5]. Metabolite production is impacted by several conditions including medium composition, pH, temperature, and aeration [5]. The physiochemical leaching efficiencies are also impacted by both temperature and pH, as well as particle size, pulp density, leachate composition, and contact time [5]. It is important to note that in non-contact bioleaching practices, the microbial metabolite production can be optimized independently from the conditions that promote optimal leaching yields. The metal tolerance of the species used need to be considered in determining whether a cell-free biolixiviant will generate increased performance.

Composition of Culture Media

The composition of the growth medium plays an important role on the metabolism, growth, and metabolite production of microorganisms. To optimize bioleaching efficiencies, the nutrients supplied in the culture media should support the production of the primary metabolites necessary to promote high metal solubilization. Depending on the microorganism used, the culture medium will vary. For Fe/S-oxidizing chemolithoautotrophic bacteria, inorganic reduced iron and sulfur compounds are required [5]. If not present in the feedstock, these compounds need to be present in the growth medium. The addition of sulfur or pyrite as well as acidification of the medium is necessary for both optimal growth and metal solubilization [5]. Although Fe^{2+} is a growth substrate for these organisms, particularly *A. thiooxidans* and *A. ferrooxidans*, high concentrations can be toxic to the organisms [5]. For example, it has been reported that the

growth of *A. ferrooxidans* can be inhibited by concentrations of Fe^{3+} less than 36 mM and the oxidation of Fe^{2+} can become inhibited by concentrations of Fe^{3+} greater than 358 mM, leading to lysis of the cells [42].

Alternatively, heterotrophic organisms can be utilized to perform bioleaching on non-sulfidic feedstocks. In this case, the supplementation of inorganic sulfur and iron is not required as the organisms do not require these components for sustained growth. Heterotrophs require the supplementation of organic carbon. Depending on the microorganism used, the carbon source can be varied to promote increased production of desired metabolites. Economic analysis of heterotrophic bioleaching, using *Gluconobacter oxydans*, indicated that the using glucose as a carbon source accounted for 44% of the total processing costs and 98% of the medium component costs [24]. This information indicates that investigation into alternative carbon substrates, such as agricultural waste, is important. Additionally, the use of surplus sugars should be avoided to prevent unnecessary processing costs.

pH

Optimal pH can enable both increased biolixiviant production as well as enhance metal leaching efficiencies [5]. As the microorganism produces leaching products, metals will begin to be leached into the medium and further impact the pH. In choosing the microorganism to be used, the impact of the growth medium pH must be considered. The pH can impact the metabolites produced by the microorganism. For example, the medium pH impacts the conversion of glucose to gluconic acid and further oxidation to keto acids (2,5-ketogluonic acid, 5-ketogluconic acid, and 2-ketogluconic acid) in *Gluconobacter oxydans* [43]. By controlling the pH between 3.5-4, an 87% conversion of gluconic acid to 5-ketogluconic acid (5-KGA) was

achieved [43]. At a pH of 5, 2-ketogluconic acid (2-KGA) production was most favorable [43]. Alternatively, at a pH lower than 3, the production of gluconic acid was most favorable [43]. By controlling the medium pH, selectivity of a favorable metabolite production could be achieved. *Aspergillus niger* has demonstrated a propensity to produce different organic acids when the pH is varied. At low pH values, ≤ 2, the fungus preferentially produces citric acid. At higher pH values, ≥4, it produces mainly gluconic and oxalic acids [5]. The medium pH can not only increase preferential metabolite production but is also an important consideration for microbial growth rate.

Metal solubilization is also affected by the pH of the biolixiviant. Increased leaching yields are often associated with higher concentrations of acids, corresponding to low pH values [5]. Lower pH values are often associated with an increased concentration of organic acids. Consequently, a lower medium pH can be indicative of greater concentrations of the leaching agent and thus correspond with higher metal solubilization yields.

Temperature

The relationship between temperature and the rate of chemical reactions is described by the Arrhenius equation (Eq. 4). As temperature is increased, the rate of the reaction is exponentially increased.

$$k = Ae^{\frac{-E_a}{RT}} \quad (4)$$

Where k is the rate constant, T is the absolute temperature, E_a is the activation energy, R is the universal gas constant (8.314 J K^{-1} mol^{-1}), and A is a preexponential factor related to the frequency of correctly oriented collisions of the reactants. Studies have indicated this relationship to hold true for bioleaching, with increased efficiencies demonstrated as the

temperature of the leaching process is increased [5]. Not only does the temperature impact the rate of leaching reactions but also the solubility of metals and REE salts. Increased leaching efficiencies associated with increased temperatures contrasts the reduced solubilities of most REE salts with increased temperatures [5]. In contact bioleaching, the temperature requirements of the microorganisms require consideration. The temperature tolerance of microorganisms is impacted by the rate of enzyme degradation [5]. Temperature settings outside of the range for microbial growth, described by the Ratkowsky equation (Eq 5) [5], will minimize the concentrations of biolixiviant production and thus negatively impact the metal solubilization yields achieved.

$$\sqrt{\frac{1}{t}} = b(T - T_{min})\left(1 - e^{(c(T - T_{max}))}\right) \quad (5)$$

Where t is the doubling time, T is the temperature, T_{min} and T_{max} are theoretical minimum and maximum temperatures for growth, and b and c are fitting parameters. Determining optimal temperature requirements is important because as the temperature of the system is increased, the energy requirements and thus cost is also increased.

Metal Resistance of Microorganisms

As metals are leached from the feedstock, increased concentrations of those metals are solubilized into the growth medium. Microorganisms have varying tolerances to heavy metals, wherein heavy metals are defined as metallic elements and metalloids with high atomic weight and density at least 5 times greater than water [44]. Both eukaryotes and prokaryotes have the ability to incorporate metal ions present in the external environment for various internal functions [30]. Heavy metal toxicity is caused by the breaking of enzymatic functions, reacting

as redox catalysts in the production of reactive oxygen species, destructing ion regulation, and by directly affecting the formation of DNA and proteins.

Consideration of the metal tolerance of the species used is necessary for determining whether one-step or two-step bioleaching is beneficial. Both one-step and two-step bioleaching are considered contact bioleaching, where the microorganism is cultivated in the presence of the feedstock. Microorganisms with a low metal tolerance may be poor candidates for contact bioleaching, as the presence of the heavy metals in the growth medium will inhibit growth and thus metabolite production. Alternatively, it is possible to adapt microorganisms to higher metal concentrations through repeated subculturing with increased metal concentrations in the medium [45]. This has been demonstrated by the repeated subculturing of *Penicillium simplicissimum* and *Aspergillus foetidus*, resulting in the generation of mutants and an adaptation of the fungi within 8 days [45, 46].

Particle Size of Feedstock

As the size of a particle decreases, a greater surface area-to-volume ratio is achieved. This increase in surface area leads to an increase in the contact area between the solid particle and the leachate, thus enhancing leaching yields. In the mining industry, decreased particle size is also often associated with increased mineral liberation, wherein the desired mineral phases are exposed to the surface resulting in increased solubilization potential [47]. Consequently, finer particle size generation not only benefits surface interactions but promotes leaching efficiencies through increased mineral liberation. Determining the optimal particle size is crucial because as particles are crushed and ground into finer grains, there is a corresponding increase in the amount of energy required. Additionally, the employment of finer particle sizes can result in increased

particle collision. When contact bioleaching is employed, particle collision can result in lysing of the cells, thus decreasing efficiencies [48].

Feedstock Pulp Density

Pulp density, or the solid to liquid ratio, is an important consideration specifically for shake flask and stirred tank reactor bioleaching. Much like particle size, pulp density can impact the contact area between the biolixiviant and the solid particle. For contact bioleaching, increased pulp densities typically inhibit microbial leaching performance due to the elevated concentrations of toxic compounds, insufficient agitation, and/or limitations in mass transfer [5].

Stir Rate

Mixing can induce beneficial surface interactions for metal leaching reactions, as well as provide proper oxygen supply for the growth of the microorganism. For most aerobic microorganisms, adequate oxygen supply promotes growth and metabolic activity. During bench and pilot scale applications, adequate oxygen can be supplied through aeration, stirring, and/or shaking [2].

Bioleaching Period

Bioleaching, compared to conventional treatment techniques, requires a greater period of time to achieve high yields [5]. The length of a bioleaching process is dependent on the growth rate of the microorganism used, the concentrations and efficiencies of the metabolites produced, and for contact bioleaching, the heavy metal tolerance of the organism. Fungal species often have a shorter lag phase [25]. This may result in a faster leaching rate and a shorter bioleaching period. Alternatively, the *Thiobacilli* genus consists of slower growing bacteria which may result

in a prolonged bioleaching process. The exposure to inhibitory metals may also result in a prolonged leaching period, resulting in a stunted microbial metabolism and a longer lag phase. Determination of the adequate bioleaching period will depend on the microorganisms used, the growth medium, as well as the feedstock composition.

Current Issues/Knowledge Gaps in Biorecovery

Bioleaching has had a slow introduction to industry, with most research studies conducted at the bench scale. It is estimated that biomining accounts for ~15% or global copper production, 5% of gold, and small percentages of other metals [49]. This is largely due to the slower rates exhibited with bioleaching technology as compared to typical chemical leaching technologies using inorganic acids [5]. Tank leaching often takes several days to complete, heap leaching requires 1-3 years, whereas dump leaching can last up to at least 5 years [49].

The performance of bioleaching processes is often lower than thermochemical processes. Thermochemical methods have noted REE extraction efficiencies from monazite ore at 89-98%, whereas the utilization of *Aspergillus* species is only capable of achieving 3-5% [50]. Metal recovery efficiencies are affected by several different variables, including pH, feedstock particle size, solid pulp density, substrate concentration, O_2 and CO_2 concentrations, bioleaching duration, shaking speed, and temperature. Process optimization would require the investigation of each of these parameters on each feedstock, which inevitably becomes very expensive and time consuming. As a result, one of the main hinderances in the adoption of bioleaching is the proper selection of experimental conditions [17].

Gluconobacter oxydans

This thesis implements the obligate aerobe bacterium *Gluconobacter oxydans* for bioleaching applications. The unique metabolism associated with this organism makes it biotechnologically relevant. Both glycolysis and TCA cycle are incomplete due to the absence of the phosphofructokinase and succinate dehydrogenase enzymes, respectively [6]. As a result, pentose phosphate pathway is highly important to its catabolism [6]. Additionally, this organism is known to incompletely oxidize various alcohols and carbohydrates due to the presence of membrane-bound dehydrogenases [51]. These dehydrogenases are responsible for the oxidation reactions resulting in high product yields. *G. oxydans* preferentially oxidizes and secretes organic acids opposed to integrating carbon into the cell, resulting in high product yields along with low growth [52]. Although the organism can produce a variety of organic acids, the high conversion of glucose to gluconic acid makes it relevant for biorecovery. Notably, abiotic gluconic acid application exhibits lower yields as compared to the biolixiviant produced through *G. oxydans* cultivation [50], indicating there are undetermined parameters contributing to its leaching effectiveness.

The application of *G. oxydans* has been demonstrated in several different feedstocks, reaching relatively high efficiencies due to the high abundance of gluconic acid produced by the organism (Table 6). By adapting cells to increasing concentrations of granulated blast furnace slag, an increased production of gluconic acid was observed. Ultimately, the concentration reached up 564.2 mM with 5% pulp density and 457.6 mM with 10% pulp density after 40 days, as compared to non-adapted cells which only achieved 172.2 mM and 343.2 mM, respectively [8]. Antonick et al. determined *G. oxydans* was capable of higher recovery efficiencies of

Yttrium from phosphogypsum than sulfuric, phosphoric acid, and commercial gluconic acids, reaching efficiencies of 91.2% [53].

Table 6. Use of *G. oxydans* toward varying feedstocks for biorecovery application. The feedstock, leaching conditions, and reported leaching efficiencies are demonstrated.

Feedstock	Conditions	Leaching Efficiencies	References
NiMH batteries	1% (wt/v) 20 mL biolixiviant 27°C 150 RPM 7 days	YE medium: 28.8% Mn, 52.8% Fe, 22.9% Co, 12% Ni, 0.9% Cu, 7.8% Zn, 19.5% REEs	[7]
		Phosphate medium: 17.3% Mn, 28.8% Fe, 19.5% Co, 7.7% Ni, 0.6% Cu, 8.5% Zn, 3.3% REEs	
Blast Furnace Slag	5% (wt/v) 35°C 120 RPM 12 days	Non-adapted cells 13% La, 19.4% Ce, 18.6% Nd, 11.2% Er	[8]
		Adapted Cells 43.4% La, 58.1% Ce, 67.4% Nd, 37.3% Er	
Phosphogypsum	2% (wt/v) 25°C 150 RPM 24 h 220 mM lixiviant	91.2% Y, 36.7% Ce, 42.8% Nd, 73.2% Sm, 50% Eu, 83.7% Yb	[53]
FCC Catalysts	1.5% (w/v) 30°C 24 h 150 RPM	50% REEs	[9]
Phosphor Powder	1.5% (w/v) 30°C 24 h 150 RPM	2% REEs	[9]

The application of *G. oxydans* supernatant toward phosphor powder and FCC cracking catalyst did not result in high yields. The supplementation of tryptone in the culturing media resulted in increased growth yields, correlated with increased total organic acid production

except in the case of *G. oxydans* strain NRRL B58 [9]. Ultimately, tryptone supplementation in the growth medium resulted in increased REE leaching efficiencies [9]. Through variation of the phosphorus source in the culture media, Rasoulnia et al. determined the leaching efficiencies of NiMH positively impacted [7]. Substitution of phosphate with yeast extract resulted in increased yields for both base metals and REEs, with the difference most pronounced in REE recovery [7].

Analytical Techniques

The purpose of this section is to provide background on the methods used to analyze feedstock samples and analyze leaching efficiencies presented in the later work.

X-ray Diffraction

X-ray diffraction (XRD) is a commonly used technique to identify crystal structures and atomic spacing within a sample of interest [54]. It is a non-destructive test commonly implemented for mineral identification in geological research. The sample is irradiated with X-rays, generated by a cathode ray tube, and filtered to produce monochromatic radiation. When conditions satisfy Bragg's law (Eq 6), the interaction between the incident rays and the sample produce a constructive interference and a diffracted ray [54].

$$n\lambda = 2d\sin\theta \tag{6}$$

where n is an integer, λ is the wavelength of the X-rays, d is the interplanar spacing of the crystal layers generating the diffraction (path difference), and q is the diffraction angle. Bragg's law states that when a crystal is bombarded with X-rays of a fixed wavelength and at certain incident angles, intense reflected X-rays are production when the wavelengths of the scattered X-rays interfere constructively. For the waves to interfere constructively, the difference in the travel path

must be equal to integer multiples of the wavelength. When this constructive interference occurs, a diffracted beam of X-rays will leave the crystal at an angle equal to that of the incident beam. Under the assumption that a powder sample is randomly oriented, the scanning of the sample through a range of 2θ allows for all possible diffraction directions of the lattice to be detected [54]. The random orientation assumption presents issues with sample preparation. As a result, sample preparation is important to minimize preferred mineral orientations. Standard reference patterns are often used to convert diffraction patterns to d-spacings. This allows for the identification of the compound due to the unique d-spacings associated with compounds [54]. The characteristic X-ray spectra are generated once enough energy is generated to dislodge inner shell electrons from the sample [54].

Quantitation is difficult because it necessitates the accurate identification of each phase within the sample [55]. Methods including the use of an internal standard, external standard, fully pattern summation, reference intensity ratio, and the Rietveld method have been implemented to overcome the issue. The full pattern summation method assumes that the diffraction pattern observed is the sum of all signals from the individual phases encompassed in the sample [55]. The Rietveld method is a refinement process between the observed and calculated patterns using partial least squares regression based on a crystal structure database [55]. In this process, the weight of each phase in a sample is obtained from the optimal value of the scale factor during refinement [55]. The reference intensity ratio, or matrix flushing, depends on the intensity of an individual peak as a reflection of the mineral content by means of the RIR values [55].

XRD has a unique capability to distinguish between different phases on the basis of their crystal structure and their chemistry [56]. It has been used increasingly in the field of mineral processing to characterize minerals, track their behavior, and to optimize the performance of metallurgical processes [56]. XRD can also be utilized to identify phases in e-waste powder samples [57].

X-ray Fluorescence

Total reflection X-ray fluorescence (tXRF) spectroscopy allows for the direct analysis of elemental composition [58]. It is ideal for the measurement of elemental concentrations in biological, medicinal, microelectronic, and environmental samples [59]. Total XRF (tXRF) involves the application of XRF toward thin sample sections. The primary difference between XRF and tXRF is tXRF requires small amount of sample for a full analysis to be performed. Samples must be prepared in thin sections for this method to be effective [59]. As a result of the small penetration depth, X-rays are able to efficiently penetrate and excite the sample thus reducing matrix effects that are commonly attributed to XRF analyses [59]. Additionally, by decreasing the sample thickness, photoelectrons have an increased probability of escaping the sample without getting scattered, resulting in a decreased background signal. This technique is capable of achieving sensitivities on the order of parts per billion, ultimately reaching limits 1000x lower than exhibited with XRF [59].

The sample is irradiated with X-rays, resulting in the partial absorption of photons by atoms in the sample and thus ejection of an electron. During the subsequent rearrangement of electrons, element-specific X-ray photons are emitted. The instrument will pick up X-ray counts at specific energies to determine elemental composition as well as concentration [59].

Scanning Electron Microscopy

Scanning electron microscopy (SEM) can be used to analyze metal containing materials due to its simple sample preparation and ability to capture high resolution images [60]. Multiple different analyses can be performed within the same instrument due to the presence of different detectors. Secondary electrons, used for high resolution imaging and surface characterizations, utilize a secondary electron detector. Backscatter electrons (BSE), measured with a backscatter electron detector, can differentiate between heavy and light elements. The instrument can also be equipped with an energy dispersive spectrometer, capable of providing a semi-quantitative element analysis. Within the instrument, an electron beam is generated and directed at the sample, ranging in energy from 0.1-30 keV [60]. The electron beam strikes the sample, interacting with a depth of about 1 μm, and generates a signal that can be read by the detector [60]. The two main ways that the electron beam and sample interact are through elastic and inelastic scattering [60].

Elastic scattering, also referred to as backscattering, results from beam electrons leaving the sample. Backscatter electrons are generated by incident electron scattering by the nucleus of the sample [60]. As the atomic number of an element within the sample increases, the yield of the backscatter electrons also increases [60]. The contrast of a BSE image thus reflects the distribution of heavy and light elements within the sample [60]. This analysis is key for geological research, allowing for the determination of the degree of liberation in the ore sample. When coupled with energy dispersive X-ray spectroscopy (EDS), the elemental distribution can also be determined.

Inelastic scattering generates signals of secondary electrons, auger electrons, characteristic X-rays, and cathodoluminescence [60]. These signals can be used to analyze the surface topography, crystallography, and composition of the sample. Secondary electrons are electrons emitted from a sample with less than 50 keV of energy [60]. These electrons are produced from a depth range of 5-50 nm, thus secondary electrons are only relevant to the surface topography of the sample [60].

EDS enables the analysis of the distribution of elements within the sample. X-rays generated by the inelastic incident electron scattering are characteristic of the elements within the sample [60]. The atoms of the inner shell become excited, causing the electrons in the outer shell to transition and produce X-rays characteristic of the elements present [60]. In general, the accelerating voltage of the electron beam should be 2-3 times the X-ray energy of the elements in the sample. As a result, when the characteristic X-ray energy is high within the sample, a higher accelerating voltage should be utilized. Alternatively, when the X-ray energy is low, a lower accelerating voltage can be used to improve spatial resolution.

Cathodoluminescence spectrometry (CL) is generated when incident electrons enter samples, resulting in inelastic scattering. When an electron beam is accelerated at a solid sample, the valence electrons within the sample are excited to a higher energy level or energy band. The excited material produces relaxation light, which can then be measured via a CL detector. There are three different situations that result in an electronic excitation that generates CL. Band-band luminescence is when electrons are excited by additional electrons and they transit from the conduction band to the valence band. Upon returning to the conduction band, the electrons will generate luminescence. Defect luminescence occurs when the excited electrons do not return to

the conduction band. Instead, they arrive at the defect position, resulting in the emission of luminescence. Lastly, impurity luminescence occurs when an inter-band impurity is excited by additional electrons resulting in the generation of luminescence. Many types of minerals, including zircon, feldspar, quartz, apatite, and carbonate can generate cathodoluminescence when excited by electrons.

Electron Backscatter Diffraction Spectroscopy

Electron backscatter diffraction (EBSD) can be utilized to identify crystallographic orientations and spatially discriminated measurements in a sample [61]. Transmission electron microscopy (TEM) can also be used to generate the same information but there is difficulty in collecting large data sets [61]. EBSD is performed within a scanning electron microscope (SEM). When the electron beam strikes the sample surface at a large angle, the sample lattice scatters incident electrons and generates a lattice channel effect caused by backscatter electrons [60]. By tilting the sample mount at an angle of ~70° and using both the BSE and EDS detectors, the mineral phases and crystal structure information of the sample can be determined. EBSD requires more intensive surface preparation than typically required for samples analyzed in SEM [60]. Detailed crystallographic characteristics of a sample can be obtained at the micron or nanometer scale [60].

To prevent misalignments, the sample is finely polished through both mechanical polishing and chemo-mechanical polishing [61]. Enhanced sample preparation creates a sharper image and lattice patterns can be generated. Depending on the sample phase composition, the polishing time and strength will vary [60].

To minimize sample charging, samples often applied to SEM analyses are coated with a conductive material such as carbon, iridium, or gold [60]. To minimize charging, while also enhancing image results for EBSD applications, a low pressure or variable pressure vacuum can be applied [61]. Variable pressure allows the intensity, contrast, and clarity of EBSD patterns to be reduced slightly. Alternatively, porous minerals can be coated initially with a thick coat of gold, repolished, and coated with carbon. The gold produces conductivity across the void spaces [61].

Inductively Coupled Plasma Mass Spectrometry

Inductively coupled plasma mass spectrometry (ICP-MS) enables highly sensitive elemental and isotopic analyses to be performed. ICP-MS has been successfully implemented in a variety of research fields including geochemistry, environmental, and life sciences, and the chemical, semiconductor, and nuclear industries [62]. Mass spectrometry, more generally, is an analytical tool used to measure the mass to charge ratio (m/z) of the molecules present in a sample. This measurement allows for the molecular weight to be calculated and the molecules or elements present in a sample to be identified. A mass spectrometer is composed of 3 main components: an ionization source, a mass analyzer, and a detector. An ICP-MS instrument utilizes inductively coupled plasma to ionize the sample [62]. The plasma, often argon, is formed using a quartz torch in a high frequency electric field [63], heated to temperatures up to 5000^{o}C. Within the torch are three concentric tubes: a nebulizer gas that carries the analyte flows through the center tube; an auxiliary gas flows around the center tube; and a coolant gas flow through the outer tube [63]. The plasma is formed through radio-frequency, forming an oscillating magnetic field [63]. A spark source functions to seed electrons into the plasma gas, generating energy high

enough to ionize atoms in the field. Further ionization results from the collision of electrons with gaseous atoms and ions. When the sample comes into contact with the plasma, it is desolvated, vaporized, atomized, and ionized [63]. The sensitivity of this technique is due largely in part to the ionization source, capable of breaking all chemical bonds in the sample thus allowing for the total content of an element within the sample to be quantified [62]. The sensitivity of this analytical method can be impacted by the presence of organic solvents and matrix effects from the sample [62]. To overcome matrix effects, a reference compound can be used for accurate quantitation [63]. For geological and e-waste samples, the minerals must be first digested to be incorporated into the liquid chromatography delivery system. This typically entails a series of acid digestion steps to dissolve the minerals. ICP-MS can achieve low detection limits, achieve multielement capability, and give isotopic information [63].

Incorporation of laser ablation (LA) allows in-situ analyses to be performed directly on solid samples [64]. In LA-ICPMS, a focused laser beam ablates the sample to generate fine particles. The ablated particles are transported to the secondary excitation source of the ICP-MS for digestion and ionization [64]. This method of element detection avoids the issues related to sample digestion, including time, incomplete digestion, and poor stability of some elements in dilute acid solutions [64]. This method can characterize elemental compositions down to the part per billion level without the need for sample preparation. The two main drawbacks to the application of LA-ICPMS for solid samples include the abundance of ions detected after m/z separation often are not entirely representative of the composition of the sample. This is due to the ablation occurring on the surface of the sample. Depending on the thickness of the solid sample, the analysis will only represent the top layer.

Atomic Absorption Spectrometry

Atomic absorption spectrometry (AAS) uses characteristic wavelengths of electromagnetic radiation from a light source to detect elements in either liquid or solid samples [65]. The method is based off the fact that every atom is comprised of a nucleus, surrounded by electrons. Every element has a specific number of electrons, which are associated in an orbital structure unique to every element [65]. The lowest energy configuration is named the ground state. When energy is applied at the correct magnitude, the energy will be absorbed by the atom resulting in an excitation state, wherein an outer electron will transition to a less stable configuration [65]. Following excitation, the atom will return to ground state and radiant energy will be emitted. This energy is equivalent to the amount of energy absorbed in the excitation process. In AAS processes, the amount of light at the resonant wavelength which is absorbed is measured. As a result, the characteristic absorbance of wavelengths by individual elements or atoms can be measured [66]. This analytical method is an easy, high-throughput, and inexpensive tool that can be used for the detection of metal in ore and e-waste samples as well as solubilized metal in leachate samples. The limit of detection is determined by the magnitude of absorbance observed and the stability of the absorbance signal [65].

AAS has been applied to environmental, clinical, pharmaceutical, food and beverage, mining and metallurgy, and petrochemical industries. Sample preparation techniques could involve use of a hot plate, microwave digestion, acid digestion or high-pressure digestion. Depending on the sample and the method of AAS, sample preparation may vary.
The interferences associated with AAS are well document and often easy to control [65]. A variety of different atomizers make this analytical technique flexible [65]. The primary interferences include matrix interference, chemical interference, ionization interference, and

background absorption. Matrix interferences can be considered in sample preparation. Additionally, the use of an internal standard can be implemented. Chemical and ionization interferences can be compensated for with the use of an appropriate releasing agent, ionization buffer, or substitution with an alternative flame type [65]. Background absorption can be removed through instrument correction techniques [65]. Some competing techniques include direct current plasma (DCP) emission, ICP emission, and ICP-MS [65]. Although increased sensitivity may be demonstrated in ICP-MS approaches, there is a significant cost and method development required for their implementation [65].

METHODS

Recycling of Lithium Ion Battery and Magnetic Swarf Waste

Spent Magnetic Swarf and LIB Powders

The spent magnetic swarf and lithium-ion battery (LIB) powders were provided by the Critical Materials Institute (CMI) group at the Idaho National Laboratory. The total REE and base metal content of the magnetic swarf was measured in house by the INL team using inductively coupled plasma mass spectrometry (ICP-MS) (Table 7). Milled swarf with a particle size of less than 0.33 mm was used in the bioleaching experiments. Samples contained primarily Fe, with lower concentrations of the REEs Nd, Pr, and Nd in a descending order.

Table 7. Composition of the milled magnetic swarf powder used in the bioleaching experiments, analyzed via ICP-MS.

Element	**Magnetic swarf content (wt%)**
Fe	73.6
Nd	16.3
Pr	6.6
Dy	2.1
Co	1.4

The LIB black mass used in this study was originally provided by Retriev Technologies (Trail, British Columbia, Canada). The black mass used in the studies reported here contained 3.61% lithium, 30.25% cobalt, 7.05% manganese, and 8.78% nickel, by mass (Table 8).

Table 8. Composition of the spent LIB powder used in the bioleaching experiments, analyzed via ICP-MS.

Element	**Black mass content (wt%)**
Graphite	39.97
Co	30.25
Al	9.25
Ni	8.78
Mg	7.05
Li	3.61
Fe	0.31
Cu	0.31
Sn	0.31
Zn	0.16

Biolixiviant Production

Gluconobacter oxydans strain NRRL B58, originally obtained from the Agricultural Research Service, USDA (Peoria, IL), was provided by INL [9]. Cultures were inoculated directly from frozen glycerol stocks of *G. oxydans*. Four media types were investigated: a modified Pikovaskaya's medium [9], a complex medium containing only yeast extract with a mass ratio to glucose of 0.08, a phosphorus-limited salts medium containing KH_2PO_4 as the sole phosphorus (2 mM), and a phosphorus-limited, complex medium containing a total phosphorus concentration of 2 mM (Table 9). Glucose concentrations (40 g L^{-1}) were held constant across all media types.

Table 9. Summary of the media used in the growth study (g L^{-1}). *G. oxydans* was inoculated with each media type and the supernatant was collected for subsequent bioleaching studies. Phosphorus content was approximated through literature review [67].

Medium component	Pikovaskaya's modified medium (Pkm)*	mPkm1**	mPkm2***	mPkm3****
Glucose	40	40	40	40
YE	0.5	3.2	-	2.48
$CaCl_2 * 2H_2O$	0.046	0.046	0.046	0.046
$(NH_4)_2SO_4$	0.5	0.5	0.5	0.5
KCl	0.2	0.2	0.2	0.2
$MgSO_4$	0.1	0.1	0.1	0.1
KH_2PO_4	0.37	-	0.27	-
$MnSO_4$	0.0001	0.0001	0.0001	0.0001
$FeSO_4$	0.0001	0.0001	0.0001	0.0001
Phosphorus content (mM)	3.12	2.58	2.00	2.00

*Pkm, a modification of the Pikovaskaya phosphate medium, substitutes the insoluble calcium phosphate with KH_2PO_4 and $CaCl_2$ [9]. This media type was used as the basis for comparison to understand the impact of bacterial growth, acid production, and subsequent bioleaching efficiencies resulting from alternative phosphorus conditions.
**mPkm1 substitutes KH_2PO_4 with yeast extract at an optimized YE/G mass ratio of 0.08 [7].
***mPkm2 had a phosphorus content of 2 mM in the form of KH_2PO_4 for a direct comparison between phosphorus in the phosphate form and encompassed in yeast extract (mPkm3) on the growth, acid production, and bioleaching efficiencies.
****mPkm3 used a phosphorus content of 2 mM in the form of yeast extract for a direct comparison between phosphorus in the phosphate form (mPkm2) and encompassed in yeast extract on the growth, acid production, and bioleaching efficiencies.

Frozen glycerol stocks of G. oxydans, 20 µL, were used to inoculate 1 L unbaffled conical flasks containing 200 mL of the appropriate medium. Each growth condition was tested in triplicate, with a control to validate there was no contamination. The flasks were incubated at 30°C at 150 RPM for 72 h. The optical density, measured at 600 nm, and pH were monitored over the course of the growth period. Samples were also collected for HPLC analysis. At 24 and 48 h, additional 15 mL samples were collected, filtered (0.22 µm), and stored at 4°C for analysis

in bioleaching experiments. The bacterial supernatant was collected at the end of the 72 h incubation period, centrifuged at 10000 x g for 10 minutes, filtered (0.22 μm), and stored at 4°C for future bioleaching experiments.

Bioleaching of REEs from Magnetic Swarf

Once HPLC analysis was performed on the *G. oxydans* supernatant, replicate flasks from each growth condition were combined to allow for standardization across leaching conditions. Bioleaching experiments were conducted with filtered (0.22 μm) biolixiviant diluted with nanopore water to 105 mM gluconic acid and applied to the magnetic swarf at 1.5 wt% solid to liquid ratio (w/w). The optimal leaching conditions were previously determined by the INL team [24]. Samples were incubated in sealed flasks at 30°C for 24 h on an orbital shaker at 150 RPM.

Bioleaching of Base Metals from Black Mass

Bioleaching experiments were conducted with filtered (0.22 μm) biolixiviant diluted with nanopore water to 75 mM gluconic acid and applied to the black mass (Retriev Technologies) at 2.5 wt% solid to liquid ratio (w/w). Ferrous sulfate, at 4.3 wt% solid to liquid ratio (w/w), was used as a reducing agent to promote Co, Ni, and Mn dissolution. The bioleaching conditions were selected from a previous optimization study [3]. Samples were incubated in sealed flasks at 55°C for 30 h on an orbital shaker at 150 RPM.

Analytical Methods

Growth of *G. oxydans* was monitored by optical density at 600 nm (OD600). The relevant growth media was used as the blank. A pH meter, calibrated daily to ensure measurement accuracy, was used to track the pH of the samples. The microbial cultures were

centrifuged and filtered (0.22 μm) and the supernatant was analyzed for organic acid content using HPLC with a BioRad Aminex HPX-87H column (300 mm x 7.8 mm, 5 μm particle size), 0.004 M sulfuric acid as the mobile phase at 0.6 mL min^{-1}, and a column temperature of 35°C. Organic acid detection and quantification was by a UV-vis photodiode array at 210 nm. The microbial cultures were centrifuged and filtered (0.22 μm) prior to HPLC analysis. The organic acid concentrations were determined from a standard curve using gluconic, citric, succinic, formic, and acetic acid standards. Samples from the same conditions, different flask, were combined due to the similarity of the acid concentrations. Following combination, the biolixiviants were diluted with autoclaved npH_2O to 75 mM gluconic acid for LIB bioleaching experiments and 105 mM gluconic acid for magnetic swarf bioleaching experiments.

REE concentrations were measured with total X-ray fluorescence (TXRF) using a Bruker S2 Picofox, with arsenic used as an internal calibrant. Base metal concentrations were measured using atomic absorption spectroscopy (AAS). The samples were filtered (0.22 μm) prior to metal recovery analysis.

Awaruite Processing

Ore processing

Samples were provided by FPX Nickel project from the Baptiste deposit in central British Columbia. A summary of sample preparation prior to receipt is summarized in Table 10. The particle size distribution of Product 1 and Product 2 is represented in Figure 1. Among the products provided were transcritical CO_2 comminuted ore (Product 3), provided by Rockburst Technologies. This ore was processed in a closed cell where CO_2 was cycled between sub-critical

and super critical conditions, leading to ore fracture. A total of 5 cycles were required to achieve a bulk particle size less than 500 μm.

There are a total of 5 different products to investigate the impact of ore concentration and subsequent leaching processes resulting from processing conditions. Product 1, 2, and 4 provide the opportunity to investigate traditional comminution practices, including crushing and grinding. Alternatively, Product 3 was processed through tCO_2 comminution. Overall, Product samples 1 through 4 were able to be analyzed through scanning electron microscopy (SEM) to compare ore concentration across comminution methods. Alternatively, Product 5 is composed of coarse grains used to generate thin section mounts for subsequent EBSD analyses. These analyses are described in more detail in the following sections.

Table 10. Summary of awaruite ore samples provided by the Baptiste deposit.

	Comminution method	**Processing Description**	**Amount**
Product 1	Crushing	Material was crushed down and split. Feed material passed through a jaw crusher and 2 cone crushers. The P80 was 1.9 mm.	5.4 kg
Product 2	Crushing and grinding	Product 1 further processed with a disk mill. A gap setting of 0.5 mm in idle mode as used. The P80 was 0.86 mm.	1.8 kg
Product 3	tCO_2	Transcritical CO_2 comminution to achieve a bulk particle size <500 μm.	485.25 g
Product 4	Crushing and grinding	Around 12 kg of ore was crushed using a jaw, big cone, and small cone crushers. The crushed ore was ground down to 500 μm P80 using a disk mill. The ground ore was subjected to magnetic preconcentration using a Carpco magnetic separator that can be operated wet. The magnetic separation was performed in batches of around 300 g each. The magnetic field intensity was set at 1000 Gauss.	~5 kg
Product 5	Crushing	Processed in a jaw crusher to generate coarse grains. Coarse grains were between 31.5-45 mm.	3 coarse grains

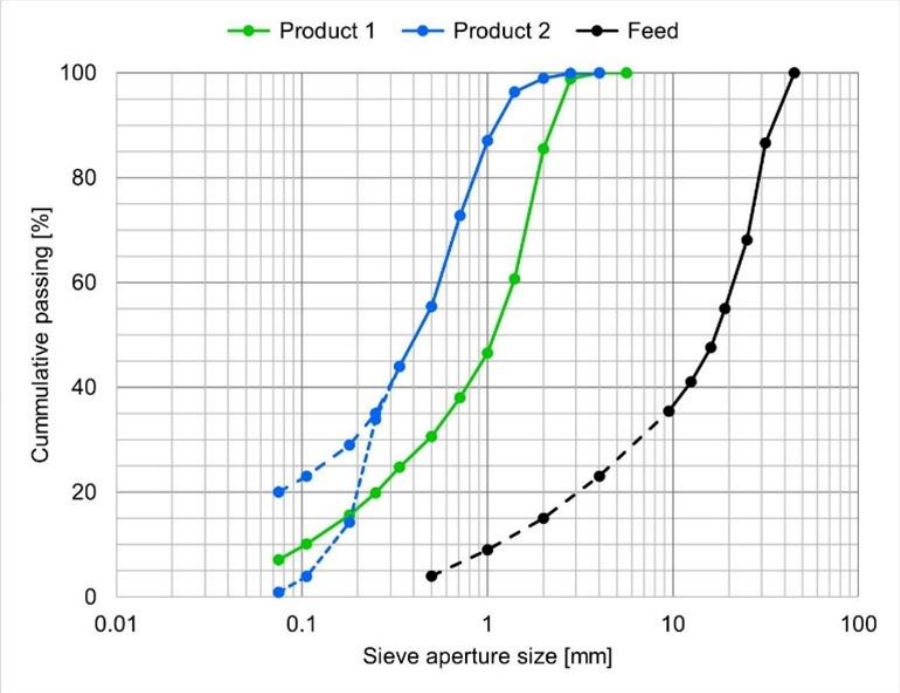

Figure 1. Particle size distribution of feed and end products of sample preparation; FPX nickel ore – Decar (Baptiste) deposit; solid line from feed is measured, dashed line from feed is not measured only assumes; solid line from crushing/grinding products are measured; short-dashed line from Product 2 is measured but heavily affected from sieve blinding; long dashed line from Product 2 is assumed real distribution. Plot and description provided by Max Hesse at UBC.

Prior to arrival, Product 4 was magnetically concentrated. XRF was performed on the product to determine the elemental composition (Table 11). The average Ni concentration of the concentrate and tails was 2029 ppm and 868 ppm, respectively. Elements that were below the limit of detection were omitted from Table 11.

Table 11. Summary of the elemental composition (ppm) of Product 4 concentrate and tails, measured via XRF. Measurements were performed at UBC.

Magnetic Concentrate					
	1	2	3	4	Average
Mg	8172	8290	6541	8845	7836
Al	4212	3935	4284	4181	4149
Si	7249	7488	7297	7977	7435
K	61	55	<LOD	<LOD	33
Ca	1815	2023	2320	2401	2103
Cr	2181	2100	1891	1978	2046
Mn	707	676	683	700	690
Fe	59196	54200	52309	55182	55227
Co	274	276	311	265	284
Ni	2160	1836	2153	1901	2029
Cu	57	38	32	38	42
Zn	57	52	46	46	51
As	4	2	2	<LOD	2
Light Elements	913239	919021	922122	916473	917891
Magnetic Tailings					
	1	2	3	4	Average
Mg	10074	8872	11106	6927	9576
Al	4447	4144	4403	4381	4338
Si	9888	9785	9506	9529	9698
K	75	83	90	101	85
Ca	2530	2930	3173	2875	2877
Cr	1087	1118	1052	1055	1081
Mn	563	572	579	571	571
Fe	25837	25575	26203	24780	25716
Co	178	157	138	150	157
Ni	907	882	852	792	868
Cu	81	104	111	164	108
Zn	46	48	55	61	51
As	5	7	8	7	6
Light Elements	944232	945657	942664	948597	944815

Product 1 samples were further milled with a disk mill. All samples were dried overnight at 60°C to minimize blinding of the fine sieves (< 250 μm). D6913-04 standard sieve protocol [68] was used to prevent the overloading of the sieves. A RoTap vibratory sieve was used to sieve all material. Each sieve run was performed for 20 minutes, aside from the sieving of Product 4 which was performed for 10 minutes. Each grain size fraction was weighed using a Denver Instrument SI-2202 scale. A SE Prospector's Choice 5 lbs hand magnet (Figure 2) was used to roughly concentrate the iron bearing minerals from the serpentines.

Figure 2. SE Prospector's Choice 5 lbs hand magnet used to accomplish magnetic separation of Product 1-3.

SEM of Ore Powder Samples

A Zeiss SUPRA 55VP Field Emission SEM, housed in the Imaging and Chemical Analysis Laboratory (ICAL) facility at Montana State University, was used to capture high resolution surface images through secondary electron detection, high contrast backscatter electron images to differentiate light and heavy minerals, and to run semi-quantitative analyses of selected spots with energy dispersive spectroscopy (EDS). Powder samples were adhered to the sample chuck using a sticky carbon dot. All samples were contained within plastic Ziplock bags. Due to a lack of a sample splitter, the bag was mixed and laid flat to minimize sample bias due to density differences between particles. The carbon dot was placed directly into the bag to

adhere particles to its surface. Nitrogen gas was blown over the sample surface to discard particles that were not properly adhered to the sample chuck.

The samples were then coated using a Pella 108 Series Carbon Coater to achieve a thickness of 20 nm. High resolution images were generated using a 30 µm aperture, 5 nm working distance, and an electron voltage of 1 keV. In the case that sample charging was an issue, samples were coated with an additional layer of Ir using an Emitech Quorum Sputter Coater K575XD. Backscatter images were used to determine the distribution of light and heavy minerals within the powder samples. The electron beam was applied at an electron voltage of 20 keV. The working distance was 8.5 nm, 60 µm aperture, and a high current was used to concentrate the electron beam. Figure 3, with corresponding description in Table 12, depicts an example of carbon coated samples prior to analysis in the SEM.

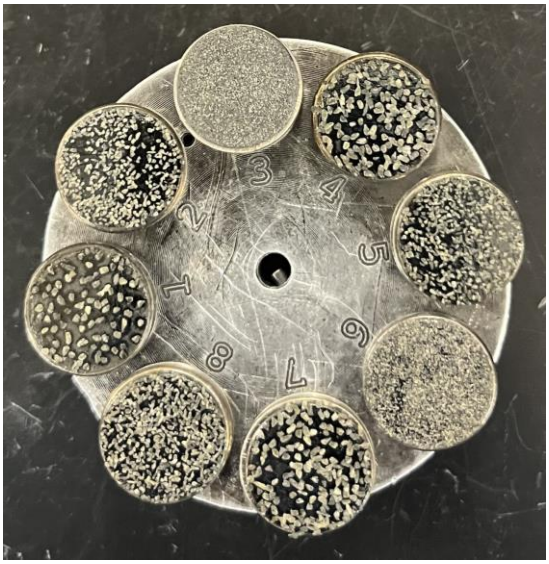

Figure 3. Samples were adhered to a carbon sticky dot and coated in a layer of carbon ~20 nm thick.

Table 12. Description of sample particles in Figure 3. Samples were adhered to a carbon sticky dot and coated in a layer of carbon ~20 nm thick.

Position	Sample	Comminution method	Particle size (μm)
1	Product 3	tCO_2	425-500
2	Product 3	tCO_2	212-300
3	Product 3	tCO_2	90-125
4	Product 4	Traditional	425-500
5	Product 4	Traditional	212-300
6	Product 4	Traditional	75-125
7	Product 1	Traditional	425-500
8	Product 1	Traditional	212-300

EBSD of Baptiste Deposit Thin-Sections

Course single particles (Product 5) were cut into approximately 25 mm x 45 mm x 15 mm thick billets using a rock saw. Thin-section mounts of the billets were generated by mounting, grind side down, to object glass using hot wax. The billets were cut to a thinner size with a Pelcon Automatic Thin Section Machine. The samples were removed from the object glass by melting the hot wax. Acetone was used to clean the samples and remove excess wax. The billets were then mounted onto petrographic glass slides using Three Bond UV curing resin TB 3021. The UV hardening glue was applied to the backside of the samples and the object glass was carefully placed on top, lowering at an angle to prevent the formation of air bubbles. A clamp was applied to adhere the sample to the glass slide evenly and force out any excess glue. After 5 minutes, excess glue was wiped up, without removal of the clamp. The samples were allowed to cure under the UV light for 10 minutes with the clamp still applied. The samples and glass were thoroughly cleaned with acetone to remove excess glue. The clamps were removed, and the samples were placed back under the UV lamp, glass slide up, to cure for an additional 20 minutes.

The sample surfaces were ground using a MetPrep3 PH-3 Grinding/Polishing System and Allied High Tech Products Grit Silicon carbide paper, 8”. The grit was increased at each subsequent run, beginning with 320 until 1200 was reached. In total, the following grits were applied: 320, 400, 600, and 1200. The system settings remained the same at each grit, summarized in Table 13. The instrument was run with complementary motion, a platen speed of 150 RPM, and a sample RPM of 150. The force was applied independently at 3 lbF. Each run was performed for 3 minutes.

Table 13. MetPrep3 Grinding settings.

Platen RPM	150
Sample RPM	150
Run time	3 min
Pressure	Independent Force
Mode	Comp
Reduce time	5 s
Reduce %	70
Force	3 lbF
Fluid	Water

The MetPrep3 PH-3 was used for the initial polishing steps, and the instrument settings are summarized in Table 14. Polishing started with 6 µm diamond. Prior to each polishing step, the diamond pad was saturated with green lube. The corresponding diamond solution was applied following the green lube. Throughout the polishing process, the diamond solution was sprayed on the pad every 30 seconds to ensure the platen remained saturated. In total, the following diamond grits were used for the initial polishing steps: 6 µm, 3 µm, 1 µm, and 0.05 µm.

Table 14. MetPrep3 Polishing settings.

Platen RPM	150
Sample RPM	150
Run time	3 min
Pressure	Independent Force
Mode	Comp
Reduce time	5 s
Reduce %	70
Force	3 lbF
Fluid	None

Ultra-polishing was achieved through vibratory polishing with Buehler Vibromet I Polisher. Colloidal silica was used as the polishing media. A quarter inch of colloidal silica (0.04 μm) was added directly into the instrument. The samples were placed in a mount with a weight applied to keep the samples adhered to the plate during the polishing process. A single weight was used to minimize the force applied. Samples were placed directly onto the plate, submersed in colloidal silver. The instrument was turned on at a high enough speed to maintain steady and continuous sample movement. Polishing was accomplished after 30 minutes.

EBSD was performed on a Zeiss SUPRA 55VP Field Emission SEM under variable pressure to minimize sample charging. A beam voltage of 25 keV was applied at high current for beam concentration. The sample mount was angle at 70^{o} with a working distance of 4.5 mm.

Image Processing

ImageJ was used to process BSE images for the purpose of modal and shape factor analyses. Images were loaded into ImageJ. Scale was set by drawing a line the length of the scale bar. Shape factor analyses were performed by setting measurements (Figure 4). The selection of

shape descriptors allows circularity, aspect ratio, roundness, and solidity to be captured. Selection of Feret's diameter allows the Feret's diameter, FeretAngle, MinFeret, FeretX, and FeretY to be captured. Aspect ratio is a function of the largest diameter and the smallest diameter orthogonal to it (Eq 7)

$$A_R = \frac{d_{min}}{d_{max}} \tag{7}$$

where d_{min} and d_{max} define the particle's minimum and maximum diameter, respectively.

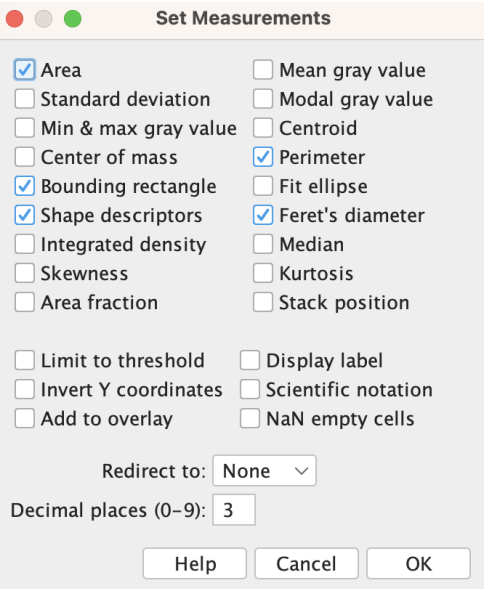

Figure 4. Measurement settings in ImageJ to determine particle shape descriptors.

Roundness captures variation at particle corners that are superimposed. It is defined as the ratio of the surface area of an object to the area of the circle whose diameter is equal to the maximum diameter of the object (demonstrated in Eq 8).

$$\text{Roundness} = \frac{4A}{\pi(d_{max})^2} \tag{8}$$

Where A is the particle area. Circularity (Eq 9) is a measure of a particle's proximity to a circle, with a value of 1.0 indicating a perfect circle.

$$\text{Circ} = \frac{4\pi A}{P^2} \tag{9}$$

where P defines the perimeter of the particle. Solidity is the particle area with respect to the convex hull area (Eq 10).

$$\text{Solidity} = \frac{A}{A_{\text{convex}}} \tag{10}$$

Due to segmentation limitations, the processing of smaller and larger particles deviated. For the larger particles (425-500 μm), once the image was loaded and the scale was set, the image type was converted into an 8-bit. Thresholding was applied manually to capture the particles, with special attention to ensure particles were not over-thresholded. Once the threshold was applied, noise was removed through the despeckle feature. The Watershed function was used to segment touching particles. Particles were then analyzed with those touching the edge removed.

Shape irregularity and limitations of the Watershed segmentation function necessitated a different approach for smaller particles (90-125 μm). Similar to the approach taken with the larger particles, the scale was set and the image was converted into an 8-bit. Interactive H-Watershed was used to generate a threshold mask for segmentation and analysis. This extension allows for the manual manipulation of seed dynamics, intensity threshold, and peak flooding (in %). This allowed for greater control over the differentiation between particles. Within the selection tab, contour overlay was selected to allow for the simultaneous visualization of both the original image as well as the segmented regions. This allowed for validation that region shapes matched the object shape of the original particles. Once region shapes were optimized, the region

mask was exported and utilized for further processing. The Biovoxxel plugin was used to ensure proper segmentation. This plugin enables the manipulation of the erosion cycle number, convexity threshold, and separator size. Preview was selected to validate parameters were selected to promote proper segmentation of particles.

Colorimetric Assay

A nickel colorimetric assay was procured from abcam and run in parallel with a DIY assay to assess assay efficacy. The kit was comprised of two primary components, sodium borate buffer and β-mercaptoethanol (βME). βME standard was developed at 10 wt%. Sodium borate buffer was developed at 4 wt%. A nickel standard (1 mM) was created with $NiCl_2$ and an iron standard was generated (1 mM) using $FeCl_2$. Standard curves were developed using the conditions specified in Table 15. All assay experimentation was performed at room temperature.

Table 15. Nickel colorimetric standard curve conditions. $NiCl_2$ and Sodium Borate Buffer were added to the cuvette to a final volume of 1.5 mL and mixed through pipette.

Standard	$NiCl_2$ Standard (µL)	nmol Ni^{2+}/cuvette	Sodium Borate Buffer (µL)
1	0	0	1500
2	75	75	1425
3	150	150	1350
4	225	225	1275
5	300	300	1200
6	375	375	1125
7	450	450	1050
8	525	525	975

$NiCl_2$ standard and sodium borate buffer were added to the cuvettes at the specified volumes (Table 15). Absorbance at both 330 and 405 nm were measured using a Thermo

Scientific Genesys 150 UV-Vis spectrophotometer. βME was added to each cuvette at a volume of 75 µL. After 30 minutes, the absorbance was measured at 330 and 405 nm. A standard curve was generated for subsequent determination of nickel in the leachate samples. To determine the concentration of samples, varying concentrations were substituted for the nickel chloride standard to ensure the nickel content fell within the linear range of the assay. The concentration of Ni in the sample was determined using the following equation:

$$[Ni^{2+}] = \frac{A_y}{S_v} \quad (11)$$

where A_y is the amount of Ni^{2+} in the sample calculated from the standard curve (nmol) and S_v is the sample volume added to the cuvette (mL).

Awaruite Leaching

Awaruite ore samples were obtained from the Baptiste deposit and processed as previously described in the Ore processing section. A summary of the grain size distributions used for leaching studies is presented in Table 16.

Table 16. Summary of awaruite ore samples applied to leaching experiments.

Comminution method	**Grain size (µm)**
Magnetic Concentrate (Product 4)	75-125 212-300 425-500
tCO_2 (Product 3)	90-125 212-300 425-500

Gluconic acid at concentrations of 75 mM and 105 mM were generated from calcium gluconate. The pH of the standards was measured at 5.97 and 6.03, respectively, for the 75 mM

and 105 mM gluconic acid stock solutions. Samples were weighed at approximately 15% (w/v) into 50 mL conical tubes. All sample conditions were performed in triplicate. 10 mL of gluconic acid standard was added to each conical tube. The samples were placed in a shaking incubator at 30°C, 150 RPM. The leachate was harvested by filtering (0.22 μm). The feedstock was collected, rinsed with deionized water, and dried overnight at 105°C for subsequent SEM or additional analyses. Feedstock obtained through traditional comminution were leached for 1, 3, and 5 days (Table 17), whereas tCO_2 samples were leached for a total of 5 days (Table 18).

Table 17. Summary of the leaching conditions for traditional comminution samples. Each condition was performed in triplicate.

Comminution Method	**Product**	**Particle Size (μm)**	**Gluconic Acid Concentration (mM)**	**Leaching Time (days)**
Traditional	Product 4	75-125	75	1
Traditional	Product 4	75-125	105	1
Traditional	Product 4	212-300	75	1
Traditional	Product 4	212-300	105	1
Traditional	Product 4	425-500	75	1
Traditional	Product 4	425-500	105	1
Traditional	Product 4	75-125	75	3
Traditional	Product 4	75-125	105	3
Traditional	Product 4	212-300	75	3
Traditional	Product 4	212-300	105	3
Traditional	Product 4	425-500	75	3
Traditional	Product 4	425-500	105	3
Traditional	Product 4	75-125	75	5
Traditional	Product 4	75-125	105	5
Traditional	Product 4	212-300	75	5
Traditional	Product 4	212-300	105	5
Traditional	Product 4	425-500	75	5
Traditional	Product 4	425-500	105	5

Table 18. Summary of the leaching conditions for tCO_2 comminution samples. Each condition was performed in triplicate.

Comminution Method	**Product**	**Particle Size (μm)**	**Gluconic Acid Concentration (mM)**	**Leaching Time (days)**
tCO_2	Product 3	90-125	75	5
tCO_2	Product 3	90-125	105	5
tCO_2	Product 3	212-300	75	5
tCO_2	Product 3	212-300	105	5
tCO_2	Product 3	425-500	75	5
tCO_2	Product 3	425-500	105	5

The leachate samples were analyzed by the colorimetric assay as previously discussed. The iron concentration (nmol) was determined using an iron standard curve due to complications with nickel determination, as discussed in more detail in the Awaruite Leaching chapter. The iron concentration was used to determine qualitative trends in leaching efficiencies across the parameters investigated.

RECYCLING OF LITHIUM-ION BATTERIES AND MAGNETIC SWARF WASTE THROUGH BIORECVOERY

Recycling of end-of-life lithium-ion batteries (LIBs) is crucial due to their importance to clean energy and the anticipated depletion of materials required in their construction. Current societal reliance on LIBs is only expected to grow, with the demand projected to outpace the raw material supply by 2030 [3]. The cathode material, consisting of metals such as cobalt, lithium, manganese, and nickel, has the greatest value for recycling. There are currently three main methods employed for LIB recycling including direct recycling, pyrometallurgy, and hydrometallurgy [3]. Direct recycling describes the recovery of materials with minimal processing, maintaining the original cathode material [3]. By preserving the original cathode morphology, recycling costs are significantly reduced [3]. This method is still in its infancy, with its slow adoption to industrial application resulting from the requirement of pre-sorting the cathode by type [3]. Pyrometallurgy uses high temperature treatment to burn off electrolytes, binders, and plastics to isolate cathode containing metals. The metals are reduced to an alloy of copper, cobalt, nickel, and iron [3]. Although this method is simply applied to any cathode configuration, it is energy intensive with high toxic gas emissions and is ultimately insufficient for the final recovery of the components required for LIB manufacture [3]. Additionally, lithium and aluminum are often left in the slag and require additional hydrometallurgical operation for their recovery [3]. Hydrometallurgy uses acids and reductants to leach the metals from the cathode materials. Similar to pyrometallurgy, this method can be applied to an array of cathode types [3]. Hydrometallurgy, although less energy intensive, necessitates high chemical and water consumption [3]. Following the process, the wastewater requires treatment, thus increasing

operational costs [3]. Alternative to the previously aforementioned recycling methods, biohydrometallurgy, or bioleaching, practices have become an attractive replacement. This method is not only environmentally beneficial due to the minimization of waste generated thereby lowering treatment costs, but has also demonstrated high recovery efficiencies [3]. A variety of organisms have been applied to the bioleaching of LIB black mass, including *Aspergillus niger* [69-71], *Gluconobacter oxydans* [3], *Acidithiobacillus thiooxidans* [69, 72], and *Acidithiobacillus ferrooxidans* [73, 74].

Similarly, REEs are susceptible to supply risks due to their limited geographical availability compounded by their growing demand in clean energy applications [75]. The permanent magnet and catalyst industries consume 23% and 24% of all REEs, respectively. Neodymium-iron-boron (NdFeB) magnets, used in electric vehicles, wind turbines and robotics, is the primary type of permanent magnet [76]. Through production of these magnets, 6-73% of swarf is produced [76]. Additionally, commercial processes for recycling REEs are not currently available. Although most REE recycling activities are still in the research and development stage, it is estimated that by 2030 recycled REEs will be the main raw material supplier for magnet production [75]. Various methods for recycling end-of-life NdFeB magnets have been investigated including hydrometallurgical processes, both leaching and bioleaching, pyrometallurgical methods, high temperature processing, and hydrogen processing of magnetic scrap (HPMS) [76].

Determination of environmentally benign, cost effective, and efficient recycling methods of these waste products is crucial for generating a circular supply chain, thus mitigating the

potential risk of resource depletion. Implementation of biorecovery is a promising avenue, making its optimization essential for future industrial application.

There are a variety of factors that can influence bioleaching efficiencies including type and amount of carbon source, produced metabolites, type of minerals and bonding within the solid matrix, as well as the growth and leaching conditions employed. Manipulation of the growth medium has a direct impact on both the concentration and type of metabolites excreted by an organism. Metal dissolution is promoted by either one or several mechanisms, which may include complexation, acidolysis, and redoxolysis [77]. Increased acid production can therefore enhance the potential for metal dissolution by decreasing the pH, thereby increasing potential for acidolysis, or proton promoted dissolution. Additionally, increased acid production results in a greater concentration of the complexing agents within the biolixiviant.

The impact of different phosphorus sources on the growth and organic acid production of *Gluconobacter oxydans* was investigated through the modification of Pikovaskaya's modified medium (Pkm) by varying yeast extract (YE) and KH_2PO_4 concentrations. A modified Pikovaskaya phosphate medium was used as a basis for comparison [9]. However, KH_2PO_4 can result in precipitation of solubilized metals and REEs, thus reducing leaching efficiencies [7]. Substitution of this soluble phosphate source with YE has been proposed to decrease the impact of metal precipitation [78]. Previous work performed by Rasoulnia et al. [7] determined that a mass ratio of YE to glucose (YE/G) of 0.08 was optimal for both the bacterial acid production of *G. oxydans* and the subsequent bioleaching of NiMH batteries. This work was used as the basis for this study to understand the impact of metal solubilization in the different waste feedstocks, with LIB containing base metals and magnetic swarf composed of primarily REEs.

The current study was conducted over a 2-month internship at the Idaho National Laboratory (INL) with the Critical Materials Institute group. Optimization of both microbial acid production and bioleaching are crucial to enable increased REE and base metal dissolution. Optimal growth conditions for the microorganism used may differ from the growth conditions required for increased bioleaching efficiencies. The implementation of a non-contact bioleaching process, where microbial growth and bioleaching processes occur independently, allowed for each process to be analyzed separately. Examination of the supernatant composition produced under the varying cultivation conditions was used to understand its impact on subsequent leaching efficiencies. The objectives were to first determine the influence of phosphorus source on the growth and organic acid production of *G. oxydans*, followed by the investigation of the leaching efficiencies associated with the biolixiviant produced under the variable media conditions. Following the collection and filtration of the *G. oxydans* supernatant, bioleaching studies were conducted on the two different feedstocks, magnetic swarf and black mass (cathode-containing powder prepared from end-of-life lithium-ion batteries).

Results and Discussion

Growth and Acid Production

The impact of different phosphorus sources on the growth and organic acid production of *G. oxydans* was investigated through the modification of the Pikovaskaya's modified medium (Pkm) to vary yeast extract (YE) and KH_2PO_4 concentrations. Four media variations were investigated (outlined in Table 19). A modified Pikovaskaya phosphate medium, containing KH_2PO_4 and $CaCl_2$ instead of $CaPO_4$ [9] was used as a basis for comparison.

Table 19. Summary of the media used in the growth study (g L^{-1}). *G. oxydans* was inoculated with each media type and the supernatant was collected for subsequent bioleaching studies. Phosphorus content was approximated through literature review [67]. Reference Table 9 in the methods for greater detail on media conditions implemented.

Medium component	Pikovaskaya's modified medium (Pkm)*	mPkm1**	mPkm2***	mPkm3****
Glucose	40	40	40	40
YE	0.5	3.2	-	2.48
$CaCl_2 * 2H_2O$	0.046	0.046	0.046	0.046
$(NH_4)_2SO_4$	0.5	0.5	0.5	0.5
KCl	0.2	0.2	0.2	0.2
$MgSO_4$	0.1	0.1	0.1	0.1
KH_2PO_4	0.37	-	0.27	-
$MnSO_4$	0.0001	0.0001	0.0001	0.0001
$FeSO_4$	0.0001	0.0001	0.0001	0.0001
Phosphorus content (mM)	3.12	2.58	2.00	2.00

The use of YE as the sole phosphorus source resulted in increased growth, indicated by the increased biomass formation by mPkm1 and mPkm3 (Figure 5A). Alternatively, the bacteria were unable to grow with KH_2PO_4 (mPkm2) as the sole phosphorus source. This result suggests that the bacteria require the additional nutrients the YE provides, perhaps free amino acids or B vitamins [78]. The high YE containing media, mPkm1 and mPkm3, resulted in around twice the number of cells after 48 h of growth, with OD600 measurements of 1.026 and 0.947, respectively. In contrast, an OD600 measurement of 0.496 was achieved for the Pkm media condition. The growth discrepancy continued to widen throughout the duration of the 72 h cultivation. The cells in the Pkm media reached the stationary phase after 48 h, and the growth rate significantly declining after 40 h, while both high concentration YE media types continued

to grow for at least 72 h. The final OD600 measurements were 0.54, 1.23, and 1.17 for Pkm, mPkm1, and mPkm3, respectively.

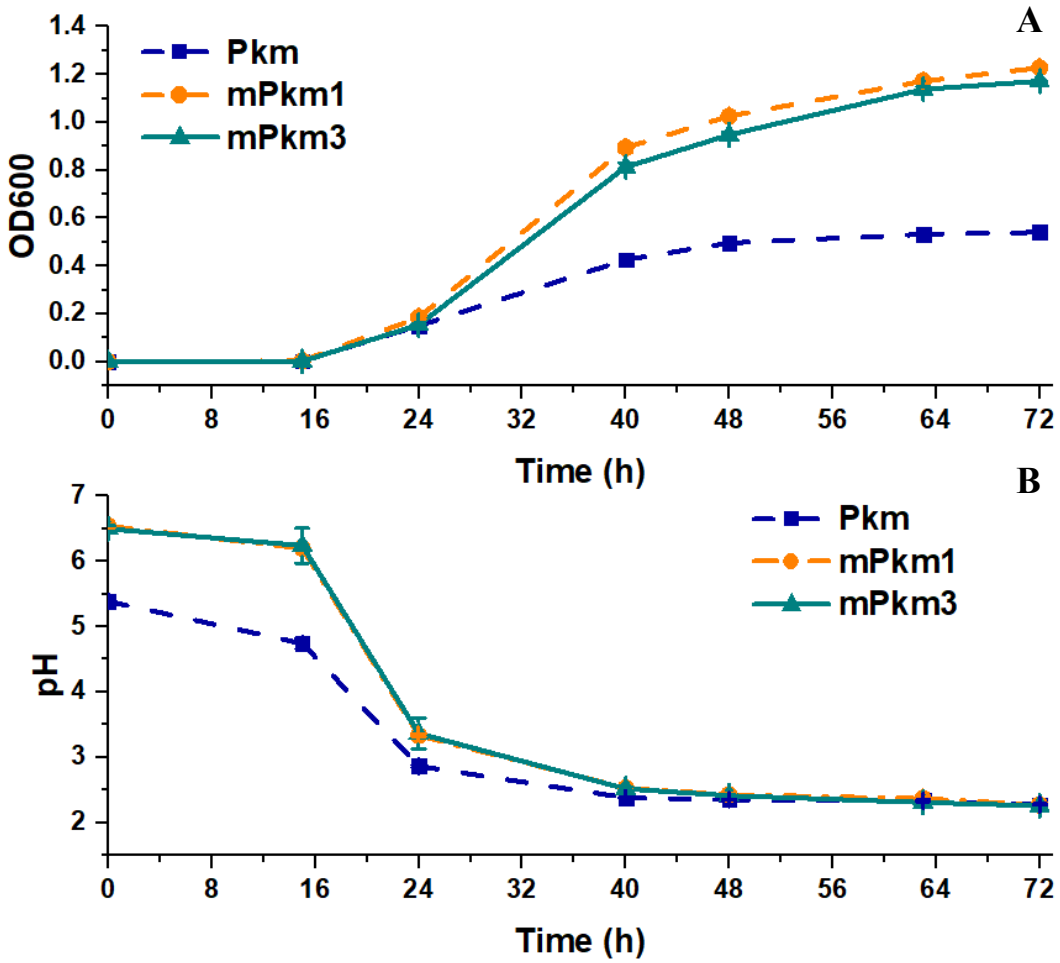

Figure 5. Growth (A) and pH (B) over the course of the 72 h cultivation period of *G. oxydans* under the variable media conditions. Pkm medium was used as a basis for comparison. mPkm1 and mPkm3 eliminated KH_2PO_4 and increased yeast extract (YE) concentrations, with mPkm1 having a YE/G ratio of 0.08. The concentration of YE in mPkm3 was 2.48 g L^{-1}.

By excluding KH_2PO_4 from the media and increasing the YE concentration, the initial pH of the media increased to 6.5 compared to 5.39 for Pkm (Figure 5B). By the end of the incubation period, the pH dropped to 2.27 under all growth conditions. A rapid decline in pH is characteristic of organic acid production by the organism.

To determine the nutrient limiting the growth of *G. oxydans* under the specified medium conditions, the biomass was approximated through literature review. The elemental composition of lyophilized *G. oxydans* cells, cultivated in YPG media at 25°C, was determined via combustion (CHN) analysis and inductively coupled plasma optical emission spectroscopy (ICP-OES) [79]. The result is summarized in Table 20.

Table 20. Unit carbon formulas (empirical formulas) of *G. oxydans*. Unit carbon formulas are expressed as number of moles of each element per mol of C [79].

Element	**Moles on a C_{mol} basis**
C	1.00
H	1.60
O	0.72
N	0.19
P	1.90E-2
S	4.04E-3
K	4.14E-3
Mg	2.96E-3
Ca	7.90E-5
Mn	1.02E-5
Fe	8.00E-5
Cu	1.77E-6
Zn	1.97E-5

The theoretical amount of biomass possible for each element, given the molar concentrations present in the growth medium, was calculated using the following equation 12.

$$\frac{X}{L} = [S] * MW_S * \frac{R_E}{mol} * MW_{G.ox} \quad (12)$$

where [S] is the substrate component concentration (g L^{-1}), MW_S is the molecular weight of the substrate (g mol^{-1}), R_E is the molar ratio of the element to the substrate (mol $mol^{-1}{}_{sub}$), mol is the molar ratio of the element within the cell, and $MW_{G.\,ox}$ is the molecular weight of *G. oxydans* (g mol^{-1}).

The presence of yeast extract created uncertainty in the calculation. Yeast extract is derived from yeast cells, often *Saccharomyces cerevisiae*. The water insoluble cell walls are removed followed by extraction and concentration of the water-soluble cellular content [78]. Yeast extract is composed of proteins, amino acids, glucans, nucleotides, B-group vitamins, and minerals [78]. It is a complex, undefined component, where the composition is variable depending on both the batch and processing procedure used [78]. As a result, the composition was approximated through literature review (Table 21).

Table 21. Composition of yeast extract, represented by mass percent.

Element	Concentration (%)
C^{*}	40
K^{*}	5
Mg^{*}	0.13
N^{**}	10
NH_3^{+} **	0.8
P^{**}	1.8
PO_4^{-} **	1

*Summarized through literature review [80].
**Measured experimentally [80].
*** Iron was determined through a back calculation using approximated concentrations in yeast extract paste. It was assumed yeast extract paste was solely hydrated yeast extract. The concentration of water in yeast extract paste was reported as 37 g/100 g YE [78]. Alternatively, yeast extract reported a concentration of 4 g/100 g YE [78]. The reported iron content in yeast extract paste, 3.7 mg/100 g YE [78], was recalculated by removing the excess water present in YE paste.

The theoretical amount of biomass (X) achieved due to the elemental composition in each medium was calculated (Eq 12) and reported in Table 22. This analysis functions to determine the theoretical limiting nutrient under each media condition.

It is possible there is iron contamination of media components, aside from $FeSO_4$, resulting in increased iron concentrations than can be accounted for. Initial nutrient limitation

investigations, calculated using Eq 12, did not consider iron as a potential nutrient limitation for this reason. The high YE media types, mPkm1 and mPkm3, were both limited for phosphorus. Alternatively, Pkm and mPkm2 were nitrogen limited. Nutrient limitation can result in the decrease of intracellular concentrations for distinct classes of metabolites, thus impacting the metabolite production [81].

Table 22. Summary of the limiting component for *G. oxydans* growth, with the amount of biomass (X/L) referencing the theoretical amount of biomass that could be generated given 1 L of each media source. The limiting nutrient(s) are indicated in red.

Media type	Element	Biomass (X/L) per L of media	Limitation
Pkm	C	38.34	Iron limited
	N	1.74	
	P	7.32	
	S	32.89	
	K	54.94	
	Mg	8.34	
	Fe	0.33	
mPkm1	C	38.34	Iron limited
	N	4.91	
	P	4.36	
	S	32.89	
	K	60.04	
	Mg	9.74	
	Fe	0.82	
mPkm2	C	38.34	Iron limited
	N	1.15	
	P	2.99	
	S	32.89	
	K	45.39	
	Mg	8.08	
	Fe	0.24	

Table 22 Continued. Summary of the limiting component for *G. oxydans* growth, with the amount of biomass (X/L) referencing the theoretical amount of biomass that could be generated given 1 L of each media source. The limiting nutrient(s) are indicated in red.

Media type	Element	Biomass (X/L) per L of media	Limitation
mPkm3	C	38.34	Iron limited
	N	4.07	
	P	3.38	
	S	32.89	
	K	53.64	
	Mg	9.37	
	Fe	0.69	

Large amounts of nitrogen are required for bacterial growth, providing the cell with the ability to synthesize proteins, nucleic acids, and other nitrogen containing compounds [82]. Consequently, nitrogen limitation is associated with low intracellular levels of amino acids, mainly glutamine and its products [81]. The limitation of nitrogen, demonstrated in Pkm and mPkm2, resulted in either decreased bacterial growth or in the case of mPkm2, no growth at all. As discussed previously, the lack of growth exhibited under mPkm2 conditions likely resulted from an inadequate supply of essential nutrients contained in the YE, which are required for *G. oxydans* growth. Alternatively, phosphorus limitation is associated with decreased quantities of phosphorylated compounds, including ATP, which is essential for energy generation and RNA production [81].

A function of the phosphate source in the growth medium is also to act as a buffer, controlling the culture pH at a level to promote bacterial growth. The conversion of glucose to gluconic acid and ketoacids (2,5-ketogluconic acid, 5-ketogluconic acid, and 2-ketogluconic acid) is highly influenced by medium pH [83]. Previous studies have shown that by controlling the media pH between 3.5-4.0, an 87% conversion of glucose to 5-ketogluconic acid (5-KGA)

can be achieved, demonstrating the favorable production of 5-KGA within this pH range. At a pH of 5, 2-ketogluconic acid (2-KGA) production is more favorable [83]. Alternatively, at a pH lower than 3, the production of gluconic acid becomes more favorable [83]. Therefore, control of the culture pH via buffer selection can result in selectivity toward favorable metabolite production.

Iron limitation has been demonstrated to promote the synthesis and excretion of iron chelating compounds, siderophores, in several organisms due to the ions major role in the electron transport chain [84]. Siderophores bind iron in soils more efficiently than low molecular weight organic acids. Compared to oxalic and citric acid, which exhibit association constants with Fe^{3+} of $10^{7.6}$ and $10^{17.3}$, respectively, siderophores have demonstrated formation constants ranging between 10^{25} to 10^{35} [85], indicating their strong ability for iron chelation. Consequently, iron was incorporated into the nutrient limitation investigation. It was determined under all media conditions implemented, iron was potentially the main nutrient limitation. Although these calculations are theoretical, promotion of siderophore production could have a substantial impact on leaching performance with respect to iron efficiencies.

Acid Strength

Heterotrophic bioleaching proceeds via one or more of the following mechanisms: acidolysis, complexolysis, and/or redoxolysis [86]. The mechanisms of acidolysis and complexolysis dominate heterotrophic bioleaching, with protons participating in acidolysis while the anion contributes to complexolysis [4]. Due to this phenomena, increased acid concentrations theoretically enhance the potential for metal solubilization. Organic acids are often either intermediates or end products in cellular metabolism, the accumulation of which is often

associated with high medium concentrations. Due to the importance of these acids as intermediate metabolites in primary biosynthetic metabolism, normal conditions result in the minimization of their extracellular concentrations. *G. oxydans* produced primarily gluconic acid with small quantities of acetic, citric, and succinic acid under the media conditions implemented in this study (Table 23). The HPLC method implemented was unable to measure keto-gluconic acid concentrations.

The strength of an organic acid can be defined by the acid dissociation constant, pKa. The pKa of weak acids is important for their characterization due to the differences between the ionized and nonionized forms [87]. A summary of the pKa values for the acids produced via the cultivation of *G. oxydans* through this study are summarized in Table 23. A lower pKa value is indicative of a higher propensity for dissociation and therefore proton donation.

Table 23. Summary of organic acid metabolites excreted from *G. oxydans*. The pKa values are provided for standard conditions (25°C, 1atm) in water. Acidolysis and complexolysis reactions are demonstrated with each organic acid cation and anion.

Organic Acid	Chemical Structure	Acidolysis reactions	pKa	Complexolysis reactions
Gluconic Acid ($C_6H_{12}O_7$)	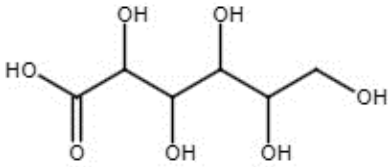	$C_6H_{12}O_7 \leftrightarrow C_6H_{11}O_7^- + H^+$	3.72[88]	$C_6H_{11}O_7^- + M \leftrightarrow C_6H_{11}O_7M$
Acetic Acid ($C_2H_4O_2$)	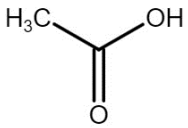	$C_2H_4O_2 \leftrightarrow C_2H_3O_2^- + H^+$	4.76[89]	$C_2H_3O_2^- + M \leftrightarrow C_2H_3O_2M$
Succinic Acid ($C_4H_6O_4$)	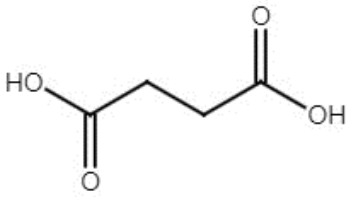	1. $C_4H_6O_4 \leftrightarrow C_4H_5O_4^- + H^+$ 2. $C_4H_5O_4^- \leftrightarrow C_4H_4O_4^{2-} + H^+$	1. 4.21[90] 2. 5.64[90]	1. $C_4H_5O_4^- + M \leftrightarrow C_4H_5O_4M$ 2. $C_4H_4O_4^{2-} + M \leftrightarrow C_4H_4O_4M$
Citric Acid ($C_6H_8O_7$)	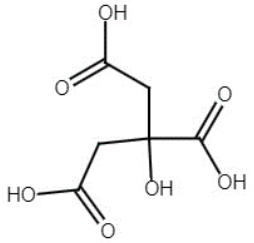	1. $C_6H_8O_7 \leftrightarrow C_8H_7O_7^- + H^+$ 2. $C_8H_7O_7^- \leftrightarrow C_8H_6O_7^{2-} + H^+$ 3. $C_8H_6O_7^{2-} \leftrightarrow C_8H_5O_7^{3-} + H^+$	1. 3.13[89] 2. 4.76[89] 3. 6.4[89]	1. $C_8H_7O_7^- + M \leftrightarrow C_8H_7O_7M$ 2. $C_8H_6O_7^{2-} + M \leftrightarrow C_8H_6O_7M$ 3. $C_8H_5O_7^{3-} + M \leftrightarrow C_8H_5O_7M$

Gluconic Acid. Gluconic acid has the second lowest pKa value of the produced organic acids, thus positioning its strength between citric and succinic acid. Excretion of this compound is characteristic of *G. oxydans*, due to the presence of membrane-bound dehydrogenases that incompletely oxidize glucose. The production of gluconic acid occurs outside the cytoplasmic membrane by the glucose dehydrogenase [51]. As a result, only a small amount of carbon is integrated into the cell [6]. Consequently, large proportions of gluconic acid are excreted by the microorganism.

The trend in gluconic acid accumulation for the first 40 h was very similar across the three growth conditions (Figure 6). Although production rates significantly declined, gluconic acid concentrations continued to increase over the entire growth period for both Pkm and mPkm3 conditions. The gluconic acid concentration decreased between 48 and 62 h for the high YE growth condition, followed by an increase between 63 and 72 h. This decline in gluconic acid concentration could be suggestive of further oxidation to 2-ketogluconate, 5-ketogluconate, or 2,5-ketogluconate [83] or it could be an artifact of HPLC sample analysis. Samples harvested from the culture were analyzed on separate days, with the 48 and 72 h supernatant analyzed a few days prior to the remaining samples. It is possible the variation in acid concentration resulted from instrument variation or equilibrium shifts during sample storage. Additional HPLC analyses would need to be performed to elucidate whether keto-gluconic acids are present.

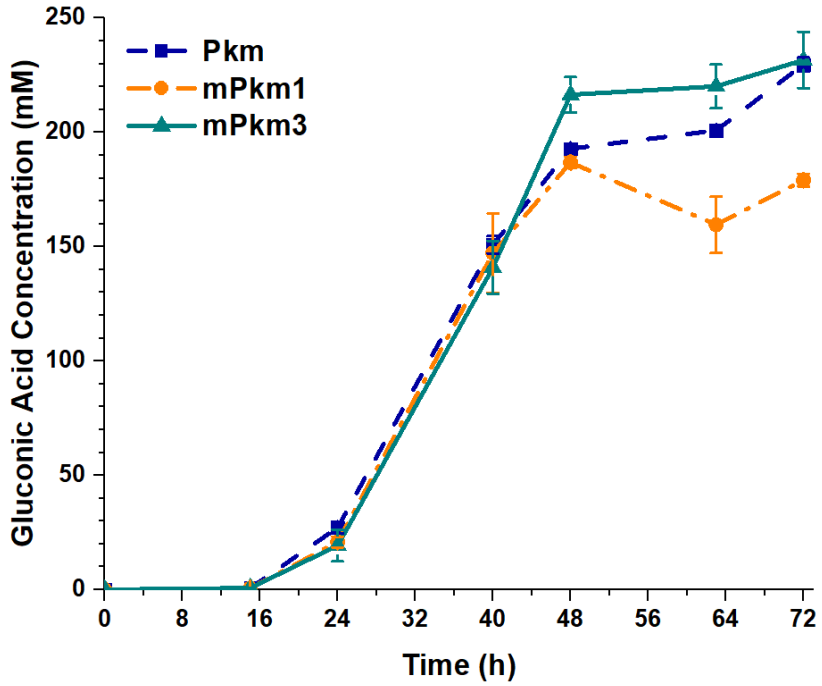

Figure 6. Gluconic acid concentration produced by *G. oxydans*, measured via HPLC, under the varying media conditions.

At 48 h, Pkm and mPkm1 cultures reached gluconic acid concentrations of 192.83 mM and 186.8 mM, respectively. mPkm3 resulted in a higher acid concentration, ending at 216.44 mM gluconic acid. By the end of the incubation period, the gluconic acid concentrations were 229.66 mM, 179.13 mM, and 231.60 mM for Pkm, mPkm1, and mPkm3 respectively. Interestingly, optimal growth was not complemented with increased gluconic acid concentrations, as was exhibited with mPkm1.

The conversion of supplied glucose, 40 g L^{-1} (220 mM), to gluconic acid under the varying media conditions is demonstrated in Table 24. Although the supplied glucose remained constant across the media types, the rate of conversion varied. Nonetheless, the conversion of glucose to gluconic acid reached upwards of 80% under all conditions. A conversion of over

100%, as exhibited for Pkm and mPkm3 conditions after 72 h, is likely due to the direct inoculation from glycerol stock resulting in some carry over of excess sugar.

Table 24. Conversion (%) of glucose (220 mM) to gluconic acid exhibited by *G. oxydans* between the harvesting point under variable media conditions.

	48 h	72 h
Pkm	87.65 ± 0.78	104.4 ± 1.39
mPkm1	84.91 ± 1.13	81.42 ± 1.26
mPkm3	98.38 ± 3.51	105.3 ± 5.61

Succinic Acid. Succinic acid is an intermediate of the TCA cycle, synthesized from α-ketoglutaric acid by α-ketoglutarate dehydrogenase. It is an intermediate in the glyoxylate bypass under aerobic conditions and an end product by the reductive TCA cycle under anaerobic conditions [91]. It is a diprotic acid [90], capable of donating two protons. The concentration increases for the first 16 hours of cultivation (Figure 7) under all conditions exhibiting cellular growth, with Pkm demonstrating the smallest concentration. After 16 h, the succinic acid concentration in the Pkm culture decreased until it was no longer detected at 40 h. Alternatively, the mPkm1 and mPkm3 stocks exhibited similar trends to each other but differed from Pkm, with concentrations increasing then dropping between each sample measured for unknown reasons, likely resulting from analytical discrepancies.

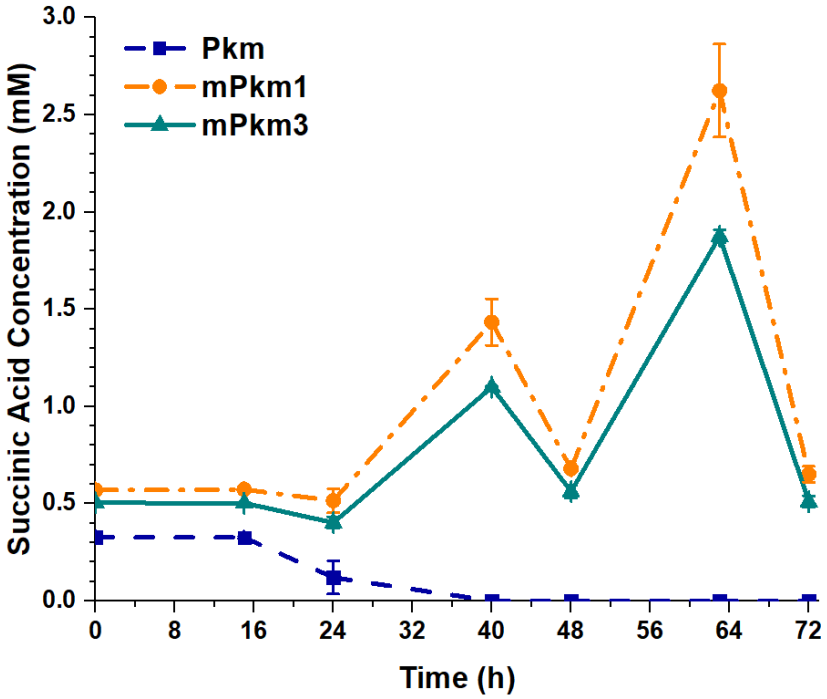

Figure 7. Succinic acid concentration during *G. oxydans* grown on 3 different media types.

The increase in succinic acid concentrations under increasing YE conditions suggests that supplementation of excess YE, thereby creating a condition where phosphorus is likely the limiting nutrient, enhanced the cell's opportunity for succinic acid production. Although the variation between conditions varied minimally, the final concentrations of succinic acid were 0.00 mM, 0.65 mM, and 0.51 mM for Pkm, mPkm1, and mPkm3, respectively.

Citric Acid. Citric acid has one hydroxyl group and three carboxylic acid groups, thus making it a good buffer for pH control and capable of three dissociation events. Citric acid is the strongest of the acids produced by *G. oxydans* (Table 23). It is a primary metabolite formed in the TCA cycle. The nitrogen source has been noted to have a significant impact on the production of citric acid due to its importance in cellular metabolism and functional application for cell proteins [92]. Concentrations of citric acid (Figure 8) exhibited a similar trend as was

visualized for succinic acid under high YE conditions, wherein after the concentration fluctuated up and down between each sample measured. The concentration in Pkm also fluctuated up and down after 24 h but ended with a final concentration of 0.00 mM by the end of the cultivation period.

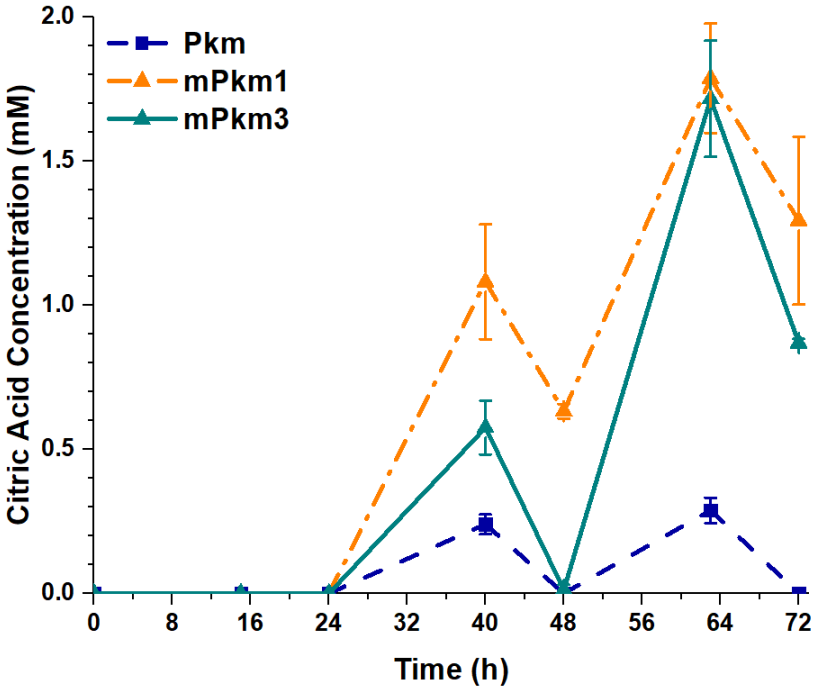

Figure 8. Citric acid concentration during *G. oxydans* growth in 3 media types.

Acetic Acid. Acetic acid, with a pKa of 4.76, is the weakest of acids produced via *G. oxydans* cultivation. It functions as a metabolite incorporated into the TCA cycle to generate acetyl-CoA. Acetic acid concentrations exhibited a similar trend of fluctuation as was exhibited for citric acid concentrations (Figure 9). Due to the low concentrations exhibited, it is possible fluctuations are a result of concentrations close to the limit of detection. The presence of these fluctuations may also result from differences in sampling time due to presence of a consistent trend across all low-concentration organic acids. Similar to gluconic acid, samples harvested

from the culture were analyzed on separate days. The 48 and 72 h supernatants were analyzed a few days prior to the remaining samples. It is possible that the variation in acid concentration resulted from instrument variation, equilibrium shifts during sample storage, or perhaps a result of being close to the limit of detection. The final concentrations of acetic acid were 0.00 mM, 1.29 mM, and 0.87 mM for Pkm, mPm1, and mPkm3 respectively. Acetic acid concentrations associated with iron limited conditions have been reported to decrease as iron dilution rates decreased, demonstrated in *E. coli* cultures [93]. As YE concentrations are increased, resulting in slightly greater iron concentrations, an increased secretion on acetate is exhibited.

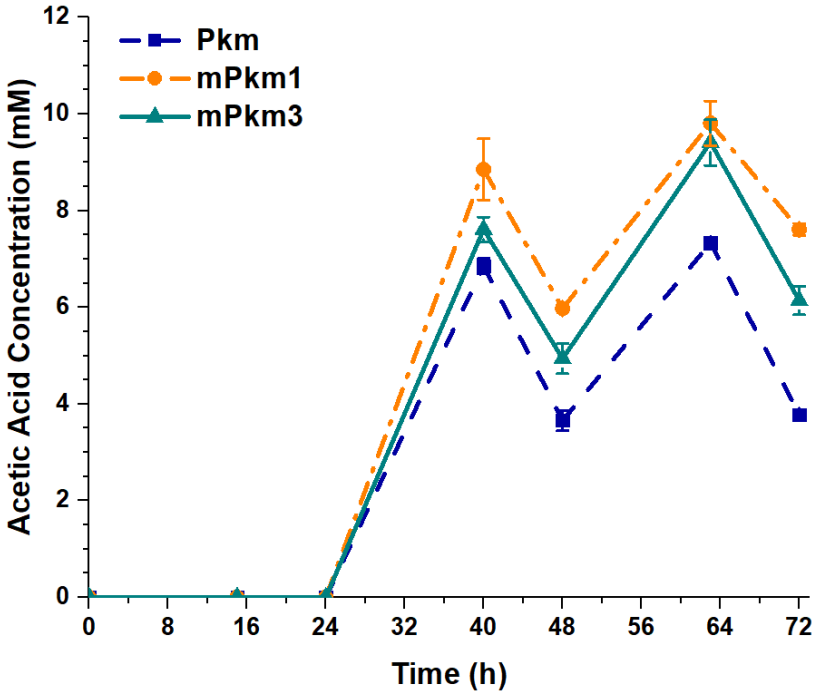

Figure 9. Acetic acid concentration during *G. oxydans* growth in 3 media types.

Ultimately the increased concentrations of succinic, citric, and acetic acid under high YE conditions are likely a result of the cells inability to perform the TCA cycle, thus increasing the secretion of these intermediate metabolites.

Spent Medium Bioleaching of Magnetic Swarf

Leaching of milled magnetic swarf was studied using the cell-free supernatant from *G. oxydans* grown on Pkm, mPkm1, or mPkm3 media. The biolixiviant was collected after 48 and 72 h of cultivation and diluted to 105 mM gluconic acid. The organic acid concentrations following gluconic acid standardization are displayed in Table 25.

Table 25. *G. oxydans* derived biolixiviant acid concentrations for the leaching experiments of the magnetic swarf feedstock.

Condition	Time (h)	Citric Acid (mM)	Gluconic Acid (mM)	Succinic Acid (mM)	Acetic Acid (mM)
Pkm	48	0.00	105.00	0.00	1.99
Pkm	72	0.00	105.00	0.00	1.73
mPkm1	48	0.35	105.00	3.24	3.36
mPkm1	72	0.73	105.00	3.26	4.46
mPkm3	48	0.01	105.00	2.30	2.31
mPkm3	72	0.40	105.00	1.96	2.79

The REE leaching yields were measured through tXRF following the leaching experiments. The leaching efficiencies (Figure 10) exhibit a consistent trend in REE recovery for the 48 h biolixiviant derived across the 3 media conditions. The effect of extended biolixiviant cultivation periods on leaching efficiencies are summarized in Table 26. After 72 h, there was a significant increase in the REE leaching efficiencies with the high YE media types, whereas application of the Pkm biolixiviant resulted in a consistent decrease across all elements. Notably, as the YE/G mass ratio was increased, the leaching efficiencies increased substantially.

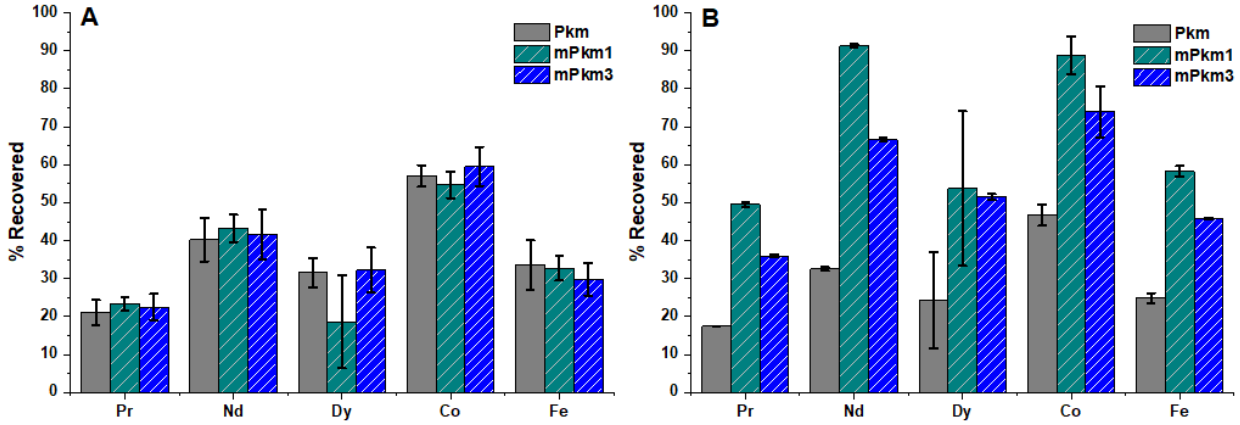

Figure 10. Leaching efficiencies for milled swarf from the biolixiviant produced after (a) 48 hours and (b) 72 hours of *G. oxydans* cultivation.

Table 26. Summary of the change in leaching efficiencies between the 48 h and 72 h biolixiviants cultivated across the 3 media types.

	Pkm	mPkm1	mPkm3
Pr	-	+	+
Nd	-	+	+
Dy	-	+	+
Co	-	+	+
Fe	-	+	+

Table 26 clearly demonstrates mPkm1 and mPkm2 benefited upon delayed biolixiviant harvest, whereas Pkm exhibited increased efficiencies for the 48 h biolixiviant. These trends are consistent across all elements leached. Error between triplicate measurements is likely a result of sample heterogeneity. Leaching experiments were performed on samples recovered from a bulk container, therefore it is possible there is flask to flask variation. Pre-leaching procedures, including the grinding of samples, introduces inherent heterogeneity between particles, which could also lead to small variations across replicate samples.

To elucidate variations between the lixiviants produced under each individual growth condition, the changes in acid concentration (represented both in relative % change and change in concentration, mM) between harvest points are summarized in Table 27.

Table 27. Variation in acid content, represented both by relative % change and by change in concentration, upon extended cultivation periods. These values are based off biolixiviant concentrations standardized to a gluconic acid concentration of 105 mM.

	Pkm		**mPkm1**		**mPkm3**	
	ΔmM	**%**	**ΔmM**	**%**	**ΔmM**	**%**
Gluconic	0.00	0.00	0.00	0.00	0.00	0.00
Citric	0.00	0.00	0.38	108.6	0.39	3900
Succinic	0.00	0.00	0.02	0.62	-0.34	-14.78
Acetic	-0.26	-13.07	1.10	32.74	0.48	20.78

The gluconic acid concentration remained constant at 105 mM across all biolixiviants due to consistent dilution conditions. While concentrations of the other acids remained low, below 4.5 mM, the profound differences in leaching efficiencies indicate their presence and/or absence may play a significant role in metal solubilization. Pkm exhibited a decrease of 13.07% in acetic acid concentrations after extended cultivation, potentially contributing to the slight decrease in efficiencies visualized for the 72 h biolixiviant. Alternatively, an increase in acetic acid concentration was complemented with higher yields for the high YE lixiviants. mPkm1 exhibited the most substantial difference and overall highest leaching yields following an extended lixiviant cultivation period, with acetic acid concentrations amounting to 4.46 mM resulting from 32.74% increase. Comparatively, the acetic acid concentration of mPkm3 also increased but ultimately the concentration was only 2.79 mM. Although variations in acetic acid concentration may contribute to the differences exhibited between leaching yields, it is likely the increase in high YE efficiencies is compounded by differences between succinic and citric concentrations.

The application of the mPkm1 and mPkm3 48 h biolixiviant yielded similar results. However, the application of the 72 h biolixiviant resulted in a deviation of extraction efficiencies, with mPkm1 exhibiting substantially greater yields. Elucidation of how these biolixiviant composition changed following an extended harvest period could provide insight into conditions promoting increased yields. As previously discussed, increased acetic acid concentration corresponded with increased yields. Additionally, both biolixiviant conditions differed in their change of citric and succinic acid content. Although mPkm3 exhibited a 3900% increase in citric acid concentration, the change amounted to only 0.39 mM resulting in a total concentration of 0.40 mM. Similarly, mPkm1 exhibited an increased citric acid concentration of 0.38 mM resulting in a concentration 0.73. Succinic acid concentrations increased minimally between mPkm1 conditions, by 0.02 mM, whereas between mPkm3 conditions the concentration decreased by 0.34 mM. It is possible the increased citric and acetic acid concentrations differentiate the yields of the high YE conditions from the Pkm condition following a delayed biolixiviant harvest. Alternatively, the differences in succinic acid likely played a role in the increased efficiencies of the mPkm1 condition. Ultimately, the REE solubilization yields benefit from the substitution of KH_2PO_4 with YE, and furthermore benefit from its increased concentration.

Spent Medium Bioleaching of LIB Material

Leaching of the LIB black mass was studied using cell-free supernatant of *G. oxydans* cultures grown on Pkm, mPkm1, and mPkm3 media. The biolixiviant was collected after 48 and 72 h of cultivation and diluted to 75 mM gluconic acid. The biolixiviant organic acid

concentrations (Table 28) had similar trends as the magnetic swarf experiments (Table 25) but were at lower concentrations due to the higher dilution of gluconic acid concentration to 75 mM.

Table 28. *G. oxydans* derived biolixiviant acid concentrations for the leaching experiments of the black mass feedstock.

Condition	Time (h)	Citric Acid (mM)	Gluconic Acid (mM)	Succinic Acid (mM)	Acetic Acid (mM)
Pkm	48	0.00	75.00	0.00	1.42
Pkm	72	0.00	75.00	0.00	1.24
mPkm1	48	0.25	75.00	2.31	2.40
mPkm1	72	0.52	75.00	2.33	3.19
mPkm3	48	0.01	75.00	1.64	1.65
mPkm3	72	0.28	75.00	1.40	1.99

Following the leaching experiments, the base metal leaching yields were measured through AAS. The leaching efficiencies for the key elements of interest are demonstrated in Figure 11 (reference Figure A.1 for a summary of all elements leached). Yields were high across all conditions investigated, reaching upwards of 50% for all key elements.

The leaching efficiencies between biolixiviant cultivation duration for each media type were compared (Table 29). The results were both varied from the trends exhibited for magnetic swarf, as well as across elements. Cu and Co were the only two elements to decrease in recovery following extended bacterial cultivation for all media types. Alternatively, there were 3 conditions that exhibited a negligible difference (<0.6%), including Li under Pkm conditions, and Al and Zn under mPkm3 conditions. Cu, Al, Mn, Fe, and Co all decreased while Ni and Zn increased for Pkm under extended bacterial cultivation. The high YE media exhibited a different trend. mPkm1 increased recovery for Li, Mn, and Fe while mPkm3 increased recovery for Li,

Mn, and Ni. There was a less substantial difference across media types, as seen with magnetic swarf. Overall, there was not a consistent trend in the recovery of base metals from LIB black mass.

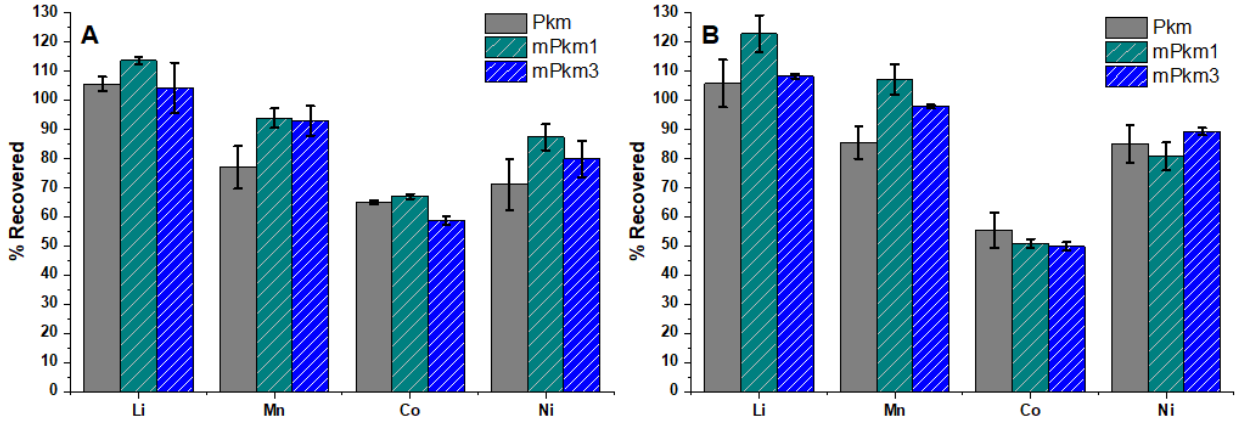

Figure 11. Leaching efficiencies for LIB black mass from the biolixiviant produced after (A) 48 hours and (B) 72 hours of *G. oxydans* cultivation.

Table 29. Summary of the change in leaching efficiencies of LIB between the 48 h and 72 h biolixiviants cultivated across the 3 media types.

	Pkm	mPkm1	mPkm3
Li	=	+	+
Cu	-	-	-
Al	-	-	=
Mn	+	+	+
Fe	-	+	-
Co	-	-	-
Ni	+	-	+
Zn	+	-	=

Lithium recovery exceeded 100% under all investigated conditions. Several factors may have contributed. Firstly, the feedstock was obtained from a bulk container of milled black mass, potentially introducing sample to sample heterogeneity. Alternatively, the higher recovery rate

could have resulted from error in sample analysis, either in the pre-leaching ICP-MS characterization or the post-leaching AAS analysis. The samples underwent acid digestion followed by analysis via ICP-MS to quantify the distribution of elements within the black mass feedstock. If the samples were inadequately digested, the results may indicate a lower composition than present, thus resulting in a higher recovery rate than achievable.

Discussion

The variation of leaching parameters, including pulp density, leaching time, temperature, and acid concentrations, does not allow for a direct comparison between magnetic swarf and LIB leaching efficiencies. Ultimately, magnetic swarf recoveries were most impacted by adjustments in the phosphorus source as well as extended bacterial cultivation, with efficiencies drastically increasing under high YE conditions for the 72 h biolixiviant. In contrast, LIB efficiencies remained relatively high across all conditions. Measurement of the acid concentration demonstrate the substitution of KH_2PO_4 with YE resulted in an increase of succinic, citric, and acetic acid concentrations. Despite the low concentration of these metabolites, below 4 mM, their difference in magnetic swarf leaching efficiencies is suggestive of their impact on overall recovery even with minimal differences.

There are some parameters that were not able to be measured that could have also impacted solubilization yields. Firstly, previous research references the use of insoluble phosphates results in the precipitation of metals. This effect is most pronounced in the case of REE, as was evidenced in NiMH extractions [7]. It is possible this effect is contributing the large yield discrepancies visualized between magnetic swarf and LIB through the substitution of KH_2PO_4 with increasing concentrations of YE.

Alternatively, due to the pH dependence of ketoacid conversion, it may also be possible that there are 2,5-, 5-, and/or 2-ketogluconic acids present within the biolixiviant. Within the first 24 hours of cultivation, the pH remained above 3 for mPkm1 and mPkm3. Previous studies have demonstrated that within this range, there is a favorable biotic conversion to 5-ketogluconic acid and 2-ketogluconic acid [43]. Due to the inability to measure the presence of these compounds via HPLC analyses, the concentration cannot be determined. If present, these metabolites may impact leaching efficiencies. After about 24 h, the pH dropped below this pH threshold of 3. The ketoacids would likely become diluted over the course of the cultivation period as increased concentration of metabolites, mainly gluconic acid, are produced. Therefore, the impact on leaching performance due to the presence of ketoacids would become less pronounced in the 72 h biolixiviants than the 48 h biolixiviants. Nonetheless, an analytical method would need to be established to determine their concentration and furthermore their impact on leaching performance.

In the case of NiMH waste feedstocks it was demonstrated that 5-ketogluconate increased base metal solubilization whereas gluconate was most efficient for REE mobilization [94]. The combination of these products significantly impacted leaching yields, in most cases decreasing efficiencies for both base metal and REE solubilization [94]. Further studies need to be conducted to determine 1) if these ketoacids are present, 2) at what concentrations, and 3) discern how and if their presence impacts the bioleaching efficiencies of both the REE in magnetic swarf and base metals in LIB.

A minimal difference in leaching efficiencies obtained through substitution of YE indicates its increased supplementation is not necessary to achieve high solubilization yields of

LIB. One of the primary hurdles associated with the industrial implementation of heterotrophic bioleaching is associated with high operational costs, of which is largely imparted by nutrient costs. Heterotrophic bacteria require large amounts of carbon to produce the desired organic acids required for subsequent leaching operations. As a result, nutrient costs are estimated to account for 44% of total process annual costs [24]. The substitution and supplementation of excess YE was demonstrated to not impart any benefit in LIB solubility yields. As such, the cost of the media components should be compared to determine the most economically reasonable approach. Ultimately, nutrients were reported to consume 44.3% of the total operating costs associated with *G. oxydans* bioleaching, largely as a result of high glucose supplementation [24]. Investigation into alternative carbon sources is required to improve the overall economics of this process.

Mineral Processing

Physiochemical separation of valuable metals and REEs from ore requires mineral processing steps to liberate, refine, and concentrate the minerals of interest (Figure 12). Mineral processing can be divided into two main functions. Firstly, preparation and liberation of valuable minerals through comminution and secondly, the separation and concentration of valuable mineral particles.

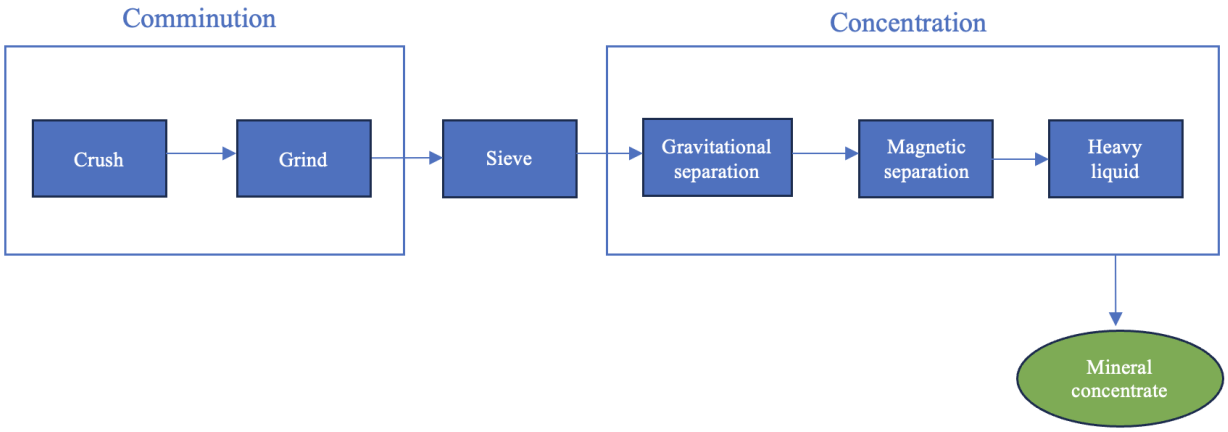

Figure 12. Typical ore processing scheme.

Typical ore bodies are comprised of disseminated minerals where the valuable minerals are both spread throughout the host rock and closely associated with low value minerals, referred to as gangue. Comminution breaks the ore into finer grains, creating a distribution of particle sizes containing different proportions of both valuable and gangue mineral phases. Mineral liberation describes the extent to which valuable mineral phases are distinct from gangue phases within an individual particle [95]. Full liberation is achieved when a particle is composed of disaggregated mineral phases. The degree of liberation is driven by three factors: (1) ore texture,

including mineral grain sizes and mineral associations, (2) final particle size, and (3) the method by which the particles are processed [95]. Optimization of an ore processing regime is critical for downstream processing, with increased concentration efficiencies often correlated to increased liberation [47]. Consequently, increased ore liberation can indirectly impact leaching efficiencies by increasing the concentration of the mineral of interest within the feedstock.

Comminution occurs in stages to sequentially reduce ore grain sizes to finer particles, achieving greater degrees of mineral liberation. It is achieved through one or more of the following mechanisms: impact, compression, and attrition [95]. Crushing, achieved through impact, is often the initial comminution step to refine the particle sizes from 1 m down to 0.5 cm [95]. Gyratory, jaw, or cone crushers are often utilized as the primary crusher [96]. Following crushing, particles are further refined through grinding or milling to reduce grain sizes down to micron sized particles [95].

Alternatively, comminution through transcritical CO_2 (tCO_2) cycling has garnered attention to reduce the energy consumption often exhibited through traditional comminution methods (Figure 13). Energy consumption in the mining industry is estimated to consume up to 10% of global energy consumption, as of 2013, with a significant proportion contributed through comminution [10, 97]. tCO_2 cycling liberates minerals through tensile fracture rather than compressive fracture [10]. The tensile strength of rocks is reported to be 90-97% lower than the compressive strength [10, 98]. The CO_2 is cycled between supercritical and sub-critical states through temperature and pressure adjustments within the closed cell. As the CO_2 moves into the supercritical phase, the low viscosity, lack of surface tension, and high diffusivity creates optimal properties for migration into the micropores of the ore structure [10]. As the CO_2 quickly

transitions to the subcritical phase, the gas expands, and the tensile strength of the rock is overcome resulting in pulverization of the ore body. Due to the closed-circuit nature of the cycling mechanism, the CO_2 can be cycled between phases to reach the extent of mineral liberation required for subsequent processing steps [10]. The degree of mineral liberation has large implications for downstream processing, positively correlating with increased ore concentration and thus increasing subsequent leaching efficiencies [47]. Achieving high degrees of liberation typically requires extensive processing under traditional comminution practices, thus generating fine particle sludge that must be removed [99]. This phenomena is due largely impart to the indiscriminate nature of traditional fracture processes [99]. The ability of supercritical CO_2 to flow into the micropore structures of the ore body presents the possibility of an ore specific, comminution technology.

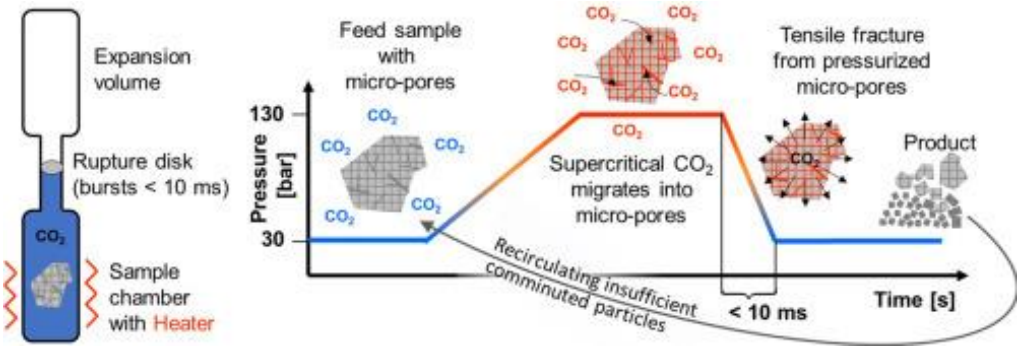

Figure 13. Representation of transcritical CO_2 comminution cycling process [10].

Following comminution, classification is often used to screen out fine grains produced to return courser grain to either comminution circuits or for subsequent processing steps [95]. Classification is defined as the method of separating a mixture of minerals on the basis of velocity with which the particles fall through a fluid medium, with water often implemented as the fluid medium [96]. Hydrocyclones and screens are widely adopted methods of classification.

Hydrocyclones use centrifugal force to separate particles. They are a simple method of classification but often are limited in their efficiency to eliminate fine particles fully from the coarse product, with the capacity to classify particles within the 1.5-300 μm range [95]. Alternatively, mineral screening can be implemented. The vibratory screen has predominantly been used to classify particles ranging from 300 mm down to 45 μm [95]. Size separation is achieved using screening surfaces, or sieves, of different mesh sizes. A screen with a smaller aperture consequently results in lower throughput. Comparatively, hydrocyclones achieve high capacity, whereas screening achieves higher classification efficiency [95]. As a result, hybrid classification can be employed to overcome the deficiencies of the classifiers and optimize for the needs of the facility in terms of size separation.

Comminution and classification function to prepare the ore for separation steps. The subsequent processing operations are based on the composition of mineral phases within the ore. Determination of the effective processing steps can be based on differences in optical features, density, magnetic susceptibility, and electrical conductivity of the minerals within the ore body [96]. Gravitational separation and magnetic separation often follow mineral liberation practices. Gravitational separation aims to separate out valuable minerals through the exploitation of density differences between valuable and gangue minerals. The four main methods of gravitational separation include spiraling, jigging, shaking, and flowing films [95]. Finer particles generally have a lower terminal velocity because of higher frictional resistance in viscous fluids such as water. As a result, gravitational separation efficiencies increase with courser grains. The utilization of gravitational separation is beneficial because it is (1) simple and easy to operate, (2) has low operational costs as it does not require expensive reagents, and (3)

similarly, it is environmentally friendly due to the absence of organic chemicals. There are a few different theoretical estimations that can be used to determine efficiencies of gravitational separation operations. A concentration criterion, Equation 13, can be used to determine whether an ore is suitable for gravitational concentration [95, 96].

$$\Delta\rho = \frac{\rho_h - \rho_f}{\rho_l - \rho_f} \tag{13}$$

Where ρ_h and ρ_l are the densities of the heavy and light minerals, respectively, ρ_f is the density of the fluid medium, and $\Delta\rho$ is the concentration criterion. In general, if the concentration criterion is greater than 2.5, gravity separation will be relatively easy, with efficiencies decreasing as the concentration criterion decreases [95]. Gravity separation efficiencies are also impacted by particle size and shape [95]. The Corey Shape Factor, CSF, is a dimensionless parameter used to estimate irregularity of mineral shapes relative to a sphere (Equation 14) [11].

$$\text{CSF} = \frac{c}{(ab)^{0.5}} \tag{14}$$

Where a, b, and c are the lengths on the longest axis, the intermediate axis, and the shortest axis, respectively [100]. When CSF is equal to 1, the particle is spherical or a cube. Gravitational separation efficiencies decrease with lower CSF values [11]. When gravitational separation is not applicable to an ore body, alternative concentration techniques must be employed.

Concentration Techniques

Magnetic separation is a widely employed technique for the recovery and manipulation of magnetic particles [101]. The wide adoption of this technique is largely due to its effectiveness, simple operation, low cost, and environmental sustainability [101]. The method is used for the concentration of magnetic components by exploiting the difference in magnetic properties

between minerals [101]. The method is a physical separation of discrete particles based on the three-way competition between tractive magnetic forces, gravitation, frictional, or inertial forces and attractive or repulsive interparticle forces [102]. Conventional magnetic separation devices are generally restricted to separating strongly magnetic materials, such as iron and magnetite [102].

Flotation is a surface driven process that relies on a particle's physical attachment to air bubbles to separate minerals by floating them to the surface of flotation cells [103]. This operation is effective only when sufficient liberation is achieved to expose valuable mineral phases on the surface. A typical flotation setup consists of a vessel or tank filled with a slurry. An impeller introduces air bubbles to the system, creating agitation of the slurry and causing minerals to remain suspended and inducing air bubble-particle interactions and attachment. The buoyancy of particle-bubble aggregates allows them to float to the surface, where they are allowed to overflow the cell lip where they are collected as flotation concentrate. The chemistry of the pulp controls the surface properties of the particles, making them amenable to air bubble attachment. Typically, the pulp consists of reagents capable of controlling the pH and electrochemical potential of the system, such as xanthates [103].

Characteristics of Awaruite

Awaruite is a nickel-iron alloy, originally discovered in Awarua Bay, New Zealand [11]. It occurs in many areas geographically including the US, Switzerland, and Canada. The alloy is commonly deposited with serpentinized ultramafic rocks [11]. In literature, it may also be referenced under different mineral names, including souesite and brokovkite, depending on the geographical location of the deposit [11]. More recently, a deposit in central British Columbia,

Canada has been discovered to incorporate large proportions of awaruite. The Baptiste deposit lies in the Decar Nickel District. Mineralogical analyses indicate that approximately 75-78% of the nickel in the Baptiste deposit is hosted as awaruite [7]. Awaruite, Ni_3Fe, has gained interest due to the high nickel content of the alloy, accounting for about 70% of the minerals content [11].

Information regarding the physiochemical properties and processing parameters of awaruite are limited as there is not an operational mine currently processing awaruite. Seiler et al. have studied the physiochemical characteristics of awaruite including the density, magnetic susceptibility, and flotation potential. The awaruite grains are shiny and metallic grey color that are easily differentiable from the dull gangue minerals and is typically contained in particles ~100 μm large [11]. A study of the Baptiste deposit from 2020 determined that 100% of awaruite particles were below 200 μm, 80% below 96 μm, and 50% below 5 μm [104]. This result indicates that to achieve full liberation of awaruite, finer grain sizes are necessary. Magnetite and serpentine are the most prominent gangue minerals in co-location with awaruite from the Baptiste deposit. Determination of the properties of awaruite along with the gangue minerals often identified in co-localization with awaruite within the Baptiste deposit helps to determine an effective processing scheme. The characteristics of the minerals in the Baptiste deposit is summarized in Table 30. Awaruite has a density of 8.57 g cm^{-3}, which is significantly higher than the main gangue material serpentine, at 2.6 g cm^{-3}. The concentration criterion, an estimate for theoretical gravitational separation efficiencies, between awaruite and serpentine was calculated to be 4.9 [11], indicating the density differences between the two minerals is great enough for an effective gravity concentration operation. Native awaruite generates flat particle grains when

ground, resulting from the high malleability of the mineral phase [11]. The CSF, a measure of shape irregularity relative to a sphere, is indicative of gravitational separation performance. Although the density of awaruite varies from gangue minerals, the CSF was determined to be less than 0.5, correlating to poor gravitational separation performance [11].

Magnetite is often co-localized with awaruite. Awaruite is ferromagnetic, having a non-linear relationship between magnetization and applied magnetic field, whereas magnetite is ferrimagnetic [11]. The primary difference between ferromagnetic materials and ferrimagnetic materials lies in the alignment of electron spins; ferromagnetic materials exhibiting parallel electron spins of equal magnitude, whereas ferrimagnetic materials demonstrate magnetic domains of varying orientations [105]. As a result, ferromagnetic materials generate a stronger magnetic field and thus exhibit a greater attraction to applied magnetic fields [105]. Nonetheless, both awaruite and magnetite are attracted to the magnetic lines of an external magnetic field. Awaruite has a greater initial volumetric susceptibility of 14.4 SI units at 0.01 T and a saturation magnetization of 750 kAm^{-1} [11]. Alternatively, magnetite has an initial volumetric susceptibility of 2 SI units at 0.01 T and a saturation magnetization of 470 kAm^{-1} [11]. Serpentine, the main other gangue mineral found within the Baptiste deposit, is paramagnetic [11]. Paramagnetic minerals are also attracted to magnetic lines of an external magnetic field, but at a lessened extent compared to ferromagnetic or ferrimagnetic minerals. To appropriately remove serpentines through magnetic separation, a lower magnetic field strength should be utilized. Due to the inability to specifically differentiate magnetite from awaruite during magnetic separation, the processing step is useful primarily for the rejection of most gangue material [106].

Consequently, an alternative separation method is necessary to isolate awaruite containing particles.

Table 30. Baptiste deposit mineral phase characteristics [11].

Mineral	**Chemical Formula**	**Density (10^3 kg/m^3)**	**Magnetic classification**	**Initial Volumetric Susceptibility at 0.01 T (SI units)**	**Saturation Magnetization (kA/m)**
Awaruite	Ni_3Fe	8.57	ferromagnetic	14.4	750
Serpentine	$Mg_3Si_2O_5(OH)_4$	2.55	Paramagnetic	-	-
Magnetite	Fe_3O_4	5.18	ferrimagnetic	2	470
Forsterite	Mg_2SiO_4	3.20	diamagnetic	-	-
Enstatite	$Mg_2Si_2O_6$	3.20	diamagnetic	-	-
Brucite	$Mg(OH)_2$	2.38	diamagnetic	-	-

Awaruite readily floats in acidic conditions in the presence of a xanthate collector [107]. The awaruite surface passivates under neutral and alkaline conditions, resulting in impedance of interactions between the xanthate collector and the mineral surface [107]. Under acidic conditions, the oxide coating is dissolved, allowing the collector to interact with the surface. Seiler et al. optimized awaruite flotation conditions for nickel recovery [107]. Awaruite was shown to selectively float under weakly acidic conditions, pH of 4.5, with potassium amyl xanthate as a collector [107]. The group also demonstrated the use of a hydrocyclone, to remove serpentine slime, resulted in similar recovery potential but decreased acid consumption by half. Although awaruite concentration is still being investigated, current research indicates that magnetic separation can be utilized to remove highly abundant serpentines and flotation can be utilized to isolate awaruite grains from magnetite.

Results and Discussion

The two primary objectives of this study were to 1) determine the extent of nickel concentration of the awaruite ore and 2) explore physical differences, if any, that exist between the different comminution methods. Due to the lack of a standardized awaruite processing procedure, a few different processing methods were investigated. While gravitational separation using a Wilfley table was attempted, the exercise was unsuccessful. This result agrees with previous reports stating the dominant CSF of awaruite ore, measured to be less than 0.5, makes the ore body not amenable to the gravitational separation [11]. In practice, gravitational separation of flat particles results in the sinking of these particles and therefore an inability to differentiate by density [11]. Consequently, processing steps implemented on the ore consisted primarily of magnetic separation. Figure 14 depicts the clear color change achieved through the application of the hand magnet (pictured in Figure 2 of the Methods), with the magnetic concentrate exhibiting a darker shade of grey when compared to the gangue material. A visual difference between samples seemed to indicate some degree of ore concentration had been achieved.

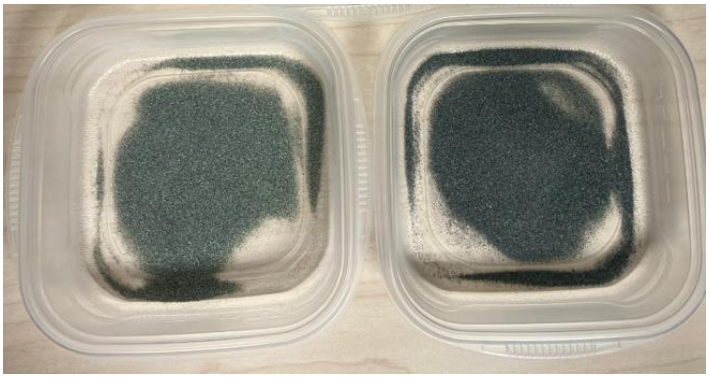

Figure 14. Gangue (left) and magnetic concentrate (right) of traditionally comminuted awaruite ore samples achieved using a SE Prospector's Choice 5 lbs hand magnet.

Degree of Liberation

Scanning Electron Microscopy (SEM) was used to evaluate the extent of nickel liberation across the various sample particles. Utilization of the backscatter electron detector allowed for a distinction between high and low atomic number elements to be made, proxies for high and low value minerals, respectively. The emission of backscatter electrons (BSE) correlates with atomic number, with heightened yields associated with increasing atomic number [60]. Thus, visualization of images with increased contrast enabled the differentiation between heavy and light elements within the sample, with brighter areas indicating the location of higher value products. These images provide insight into the extent of mineral liberation and concentration achieved through the mineral processing steps implemented.

A high distribution of bright spots in the BSE images indicates a high degree of ore concentration. Enhanced concentrations of bright spots with respect to dark spots provides evidence that ore processing efforts effectively concentrated the samples. Alternatively, the spatial distribution of bright spots within an individual particle in respect to the dark spots establishes the degree of mineral liberation. Full liberation is characterized by a particle composed predominantly of unbound bright spots.

Initial studies focused on particles between 212-300 μm to determine the efficacy of magnetic separation using a hand magnet. The analysis, displayed in Figure 15, illustrates a higher concentration of high value product in the magnetically separated ore products, evidencing the ability of the magnet to discriminate some magnetic particles. Although the concentration is greater, these particles have very minimal phase liberation and an overall small concentration of heavy elements with respect to silicates within the magnetically separated

product. Overall, the analysis provides evidence the samples require further concentration prior to downstream processing.

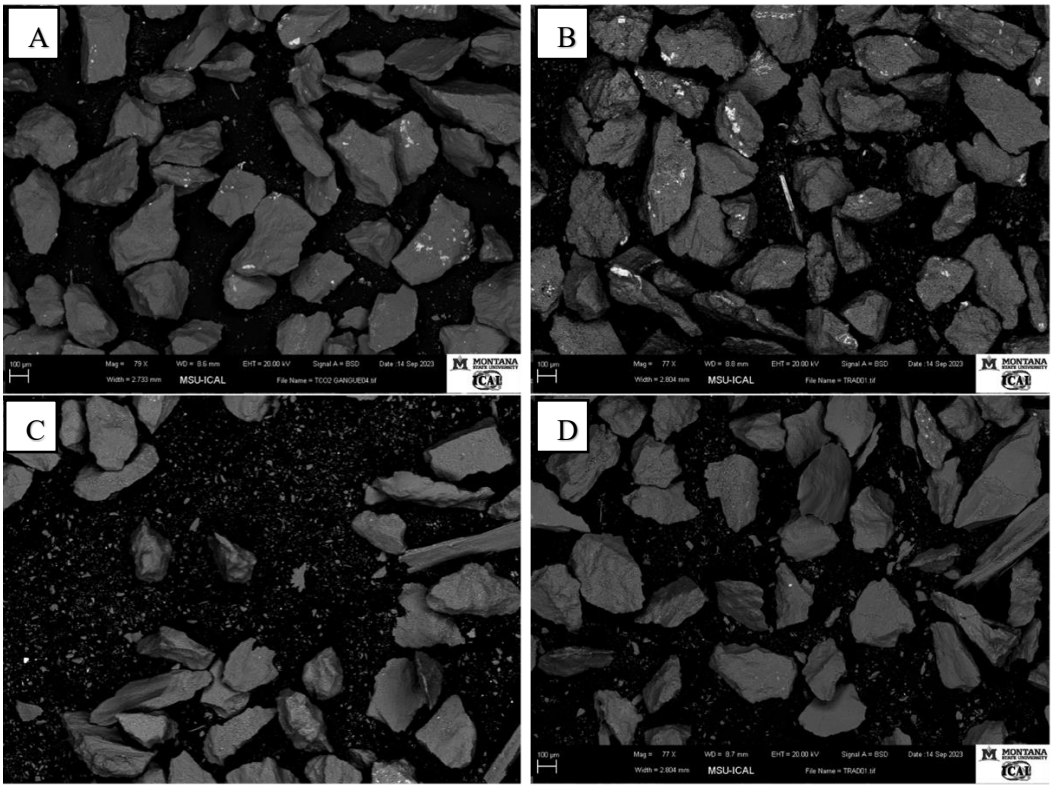

Figure 15. BSE images for the A) tCO_2 (Product 3) magnetic concentrate, B) Product 1 magnetic concentrate, C) tCO_2 (Product 3) gangue, and D) Product 1 gangue. All products were concentrated with a hand magnet.

Liberation and relative nickel concentrations were compared across the magnetic concentrates. EDS spectra on selected sections of the sample enabled a semi-quantitative determination of the elements present within the selected spots. The analysis focused on particles sized between 90-125 μm and 425-500 μm of both tCO_2 (Product 3) and Product 4 magnetic concentrate samples. Notably, Product 4 was not refined into distinct grain size fractions; therefore, the smaller grain size range analyzed consisted of particles between 75-125 μm. The BSE images and corresponding EDS maps are demonstrated in Figure 16 (reference Appendix

Figure A.2 for the remaining images collected). Visually, there appears to be a distinction of both mineral disaggregation and concentration across both comminution methods and particle sizes. Compared to the coarse traditional samples, tCO_2 particles exhibit a larger proportion of high value product (Figure 16A, 16E), determined to be primarily nickel and iron through EDS (Figure 16B, 16F). This trend is consistent across smaller particles as well. Regardless of comminution method, smaller particles resulted in both higher concentrations of minerals as well as higher degrees of liberation.

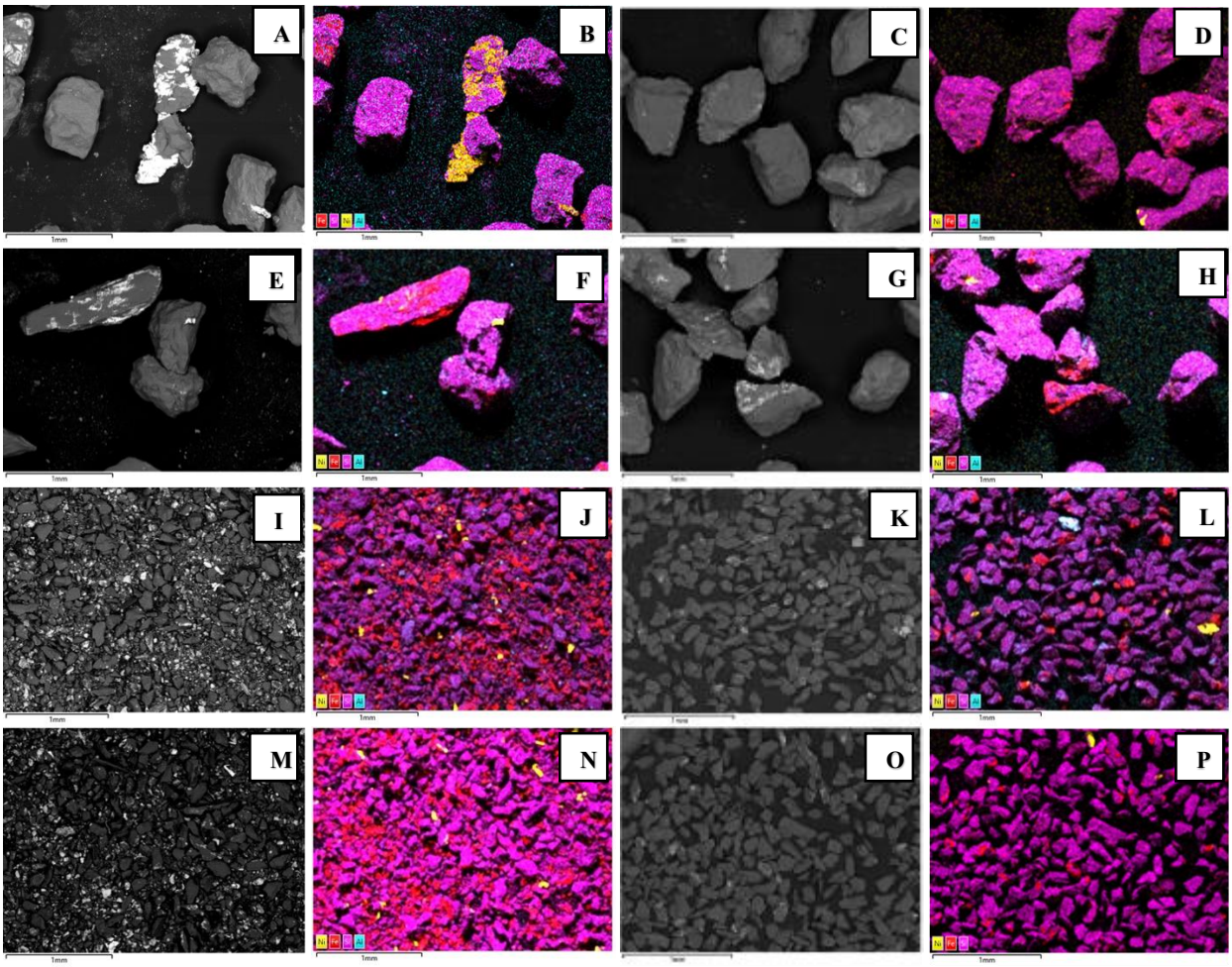

Figure 16. Backscatter electron images with corresponding EDS map. Samples were mounted onto sample mounts and coated in ~20 nm of carbon. A and E depict BSE images of 425-500 µm tCO_2 particles with the corresponding EDS map in B and F. C and G depict BSE images of 425-

500 μm traditional particles with the corresponding EDS map in D and H. I and M depict 90-125 μm tCO_2 particles with the corresponding EDS map in J and M. K and O depict 75-125 μm traditional particles with the corresponding EDS map in L and P. EDS images denote nickel in yellow, iron in red, silicon in pink, and aluminum in teal.

To quantify differences in high value product concentration across comminution methods and particle size, ImageJ was used to determine relative content with respect to total particle area (Table 31). Additionally, the full map EDS spectra results are summarized in Appendix Table 4A and Table 5A, although these spectra may present issue due to the small particles sizes. An accelerating voltage of 20 keV was utilized to increase backscatter electron signal, thus sacrificing spatial resolution. It is possible some signal is picked up from below the particle surface.

tCO_2 particles exhibit a higher proportion of high value product relative to total sample area compared to traditional comminution, indiscriminate of particle size. Furthermore, as particle size decreased the concentration of high value product further increased. Although present, this result is much less pronounced in traditional comminution samples. A difference in concentration, quantified as 7.67% for coarser particles and 14.63% for finer particles, provides evidence that the use of tCO_2 comminution generates grains more amenable to magnetic concentration.

Table 31. Bright spot content, primarily composed of nickel and iron, relative to total particle area averaged across all sites imaged. The images analyzed in ImageJ were the BSE images, as pictured in Figure 16 and Appendix Figure A.2. A full summary of the ImageJ results broken down by site analyzed can be found in Appendix Table 6A.

	Relative High Value Content (%)
tCO_2 425-500 μm	10.32
tCO_2 90-125 μm	19.1
Traditional 425-500 μm	2.65
Traditional 75-125 μm	4.47

Sampling bias may have influenced these results substantially. Typically, a splitter is used to ensure there is a lack of sampling bias [108]. However, in this study, samples were obtained by pressing the carbon dot into the sample and analyzing the particles that adhered. This could introduce bias toward light particles, opposed to heavy particles that may have been distributed unevenly toward the bottom of the bag. The use of a sample splitter could generate representative sub-samples to mitigate sampling bias that may result from sample storage. It is uncertain whether there was a bias toward particle orientation. A preferred orientation of the particles would result in a non-representative depiction of the liberation of the particles. This analysis could be complemented with an alternative analytic test such as XRF to determine the overall elemental composition of the sample prior to analysis within the SEM. XRF is non-destructive, therefore the same sample could be cycled through the series of tests to determine whether the entire grain is composed of gangue minerals and at what concentration the high value minerals were present on the visualized surface.

Displayed in Figure 17 is a representation of disaggregated awaruite, with 17B depicting a zoomed in view of the mineral phase demonstrated in 17A. EDS was performed on selected spots to determine their approximate elemental compositions, represented in Table 32. The relative proportions of Fe to Ni indicate the primary mineral phase is awaruite, Ni_3Fe. Alternatively, Spectrum 13 and 15 demonstrate magnetite in close approximation with the awaruite phase.

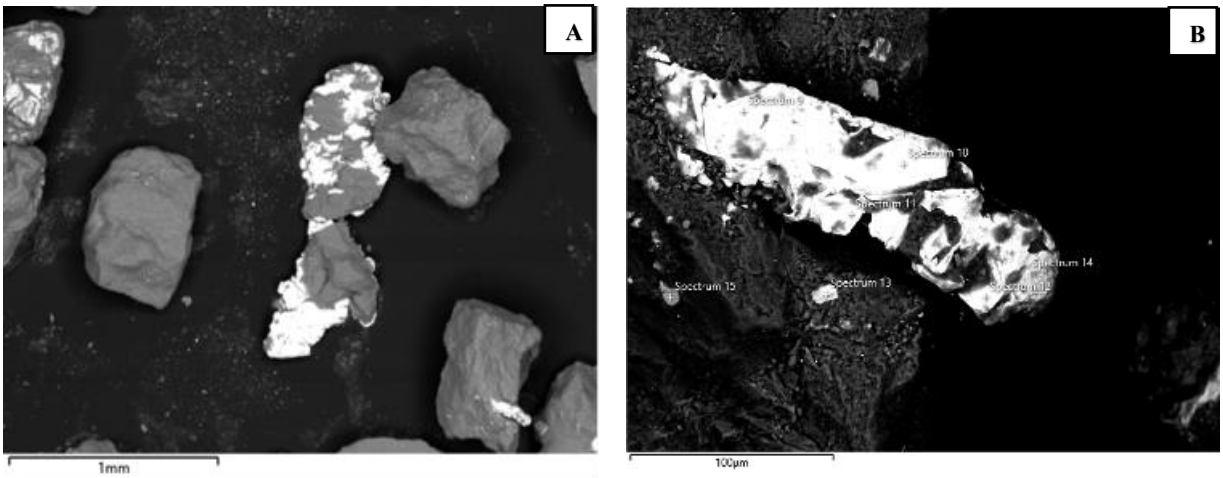

Figure 17. Representation of disaggregated awaruite mineral phase found in Baptiste deposit.

Table 32. EDS spectra obtained for selected spectra displayed in Figure 17B.

	Ni	Fe	O	Mg	Si	Cu	Co	Al	Na	S	Ca	Ti	Cr
Spectrum 9	65.15	19.69	6.51	4.53	1.95	1.14	0.73	0.19	0.10	0.02	0.00	0.00	0.00
Spectrum 10	75.18	21.00	1.10	0.25	0.20	1.54	0.58	0.06	0.09	0.00	0.01	0.00	0.00
Spectrum 11	64.84	20.02	6.48	4.80	1.88	1.28	0.50	0.12	0.04	0.04	0.00	0.00	0.00
Spectrum 12	64.42	19.10	7.50	4.67	1.82	0.98	1.12	0.18	0.11	0.00	0.00	0.02	0.00
Spectrum 13	0.48	67.82	29.55	0.77	0.31	0.04	0.27	0.04	0.00	0.00	0.01	0.06	0.66
Spectrum 14	51.09	17.13	14.70	10.71	4.44	0.67	0.72	0.19	0.14	0.07	0.09	0.01	0.00
Spectrum 15	0.23	83.09	10.42	3.54	1.55	0.01	0.47	0.09	0.06	0.03	0.02	0.00	0.48

Difference in Comminution Methods

The second objective of this study was to investigate whether physical differences in the ore exist between traditional and tCO_2 comminution methods. The role of comminution in mineral processing is to simultaneously reduce particle size and liberate minerals [99]. Traditional comminution is typically accomplished through the application of compressive forces. These compressive forces lead to the fracture of the ore body and when applied in series, optimal sized particles can be achieved. However, conventional comminution methods often lack

efficiency of mineral liberation, operating indiscriminately to fracture the ore body to finer grain sizes [99]. The liberation characteristics of an ore body with respect to grinding is heavily related to the mineralogical texture of the ore [47]. Interactions between the comminution method and textural properties of the ore therefore determine liberation efficiencies [47]. Additionally, the degree of liberation impacts downstream concentration efficiencies, with high degrees of liberation correlated to increased ore concentration [47]. Low liberation efficiencies increase operational costs by necessitating the production of finer grains to enhance mineral liberation [99].

In contrast to conventional grinding comminution practices, tCO_2 comminution breaks apart the rock by overcoming tensile forces [10]. While tCO_2 is potentially less energy intensive, it is also hypothesized the process is capable of fracturing particles along grain boundaries. Theoretically, this assumption would provide great benefit to downstream processing. Breakage along grain boundaries would likely increase liberation potential, exposing valuable product and increasing leachable surface area. As demonstrated in the previous section, tCO_2 fracture appeared to increase subsequent concentration efforts and provide increased proportions of disaggregated awaruite particles as grain size decreased. To investigate potential disparities between comminution methods, surface topography, grain size distributions, and shape factors were analyzed and compared. Inconclusive surface topography secondary electron images are contained in Appendix Figure A.3.

Sieve Analysis. To assess the validity of the grain boundary assumption, the grain size distribution among samples was first determined. Utilizing a RoTap vibratory sieve, samples were collected and weighed from each mesh size. The analysis encompassed Product 1, Product

2, and Product 3. The grain size distribution collected on each sieve mesh size is plotted in Figure 18, demonstrated as both relative wt% in 18A and % passing in 18B. Notably, Product 1 and Product 2 samples were plotted independently due to observed physical differences in the samples. Product 2 samples appeared powdery and exhibited a lighter shade of grey when compared to Product 1 samples. Additionally, the samples underwent separate processing procedures, with Product 1 processed internally using a disk mill and Product 2 processed at the UBC facilities using a similar series of fracture methods. Consequently, the samples were kept separate throughout the analysis.

A minimal difference in grain size distribution is observed between the traditional (Product 1 and Product 2) and tCO_2 comminution methods. tCO_2 comminution yields a slightly higher proportion of large particles (>212 μm), whereas traditional comminution generated a greater distribution of finer particles (<125 μm), specifically for Product 2. Both products processed via traditional comminution exhibited a significant content of large particles (>500 μm). It is possible that if these products were further refined, the distribution would more closely align with tCO_2, although it has been reported the indiscriminate nature of traditional comminution results in high proportions of fine granular sludge [99]. The ability of tCO_2 comminution to generate a higher proportion of large particles could be indicative of discriminate fracture, thus inducing a wider distribution of native mineral phases.

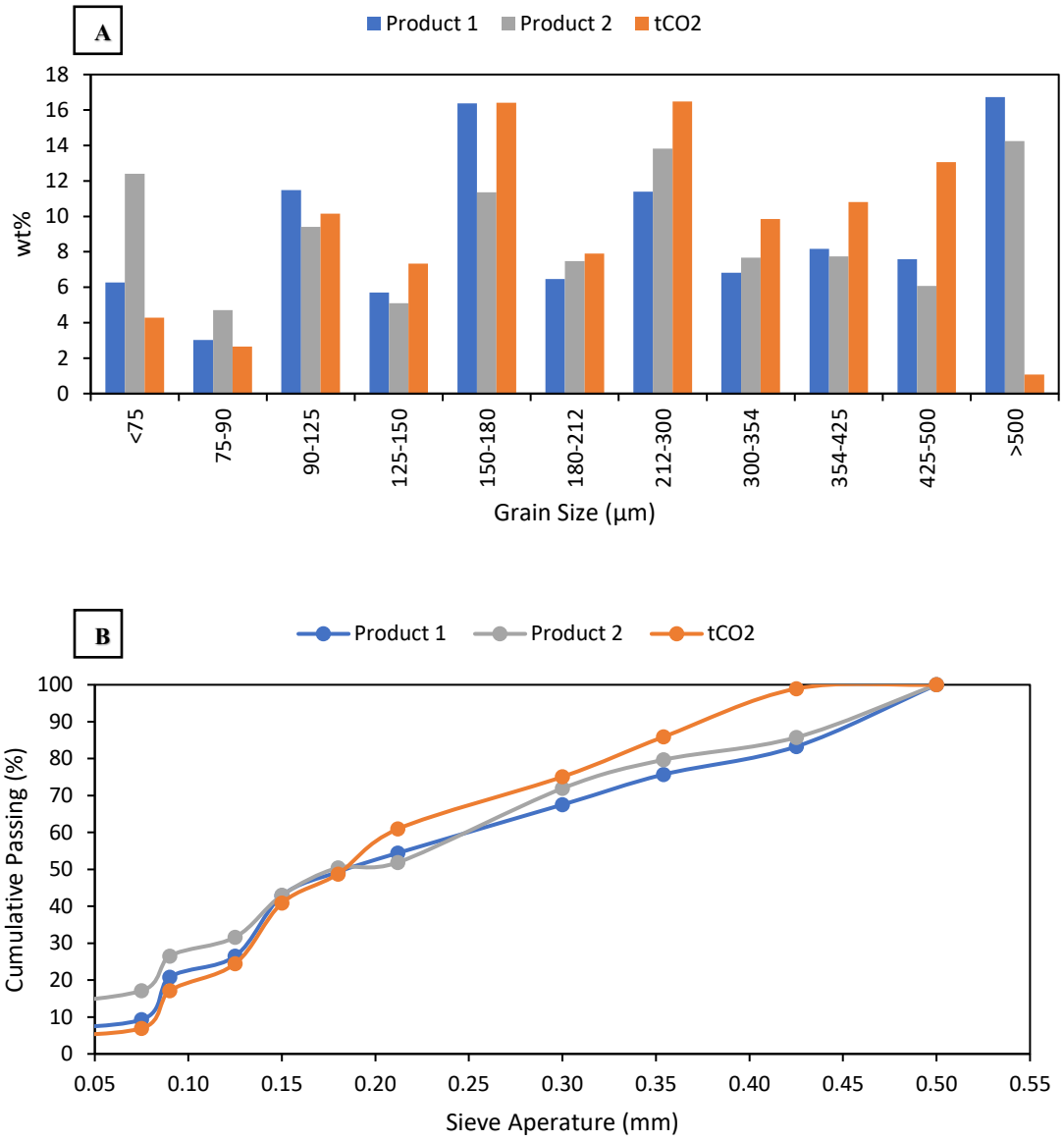

Figure 18. Grain size distribution for Product 1, Product 2, and Product 3 (tCO_2) samples. The data is represented both as a bar graph to demonstrating (A) relative weight % per grain size range and as (B) cumulative passing.

To provide further insight into the grain boundary assumption, EBSD analyses were performed on the native Baptiste deposit ore. The grain size distribution of the native ore was to be compared to the grain size distributions established through both comminution methods.

EBSD. The use of EBSD aimed to establish the native grain size distribution within the Baptiste deposit. This identification would allow for direct comparison with both the traditionally ground and tCO_2 fractured ore distributions. It is hypothesized that if a comminution method fractured ore along grain boundaries, the distribution would closely align with that of the native ore, determined through EBSD analyses.

EBSD requires enhanced quality of the sample surface to generate a sharper image, lattice patterns, and prevent misalignments [60]. The implementation of a combination of mechanical and chemo-mechanical polishing are often exhibited [109]. Sample compositions helps to determine the time, strength, and tools applicable to successfully polish the sample [60]. Careful attention to sample preparation is important due to the possible generation of artifacts. Artefacts, often exhibited in serpentines, include the production of dislocations or amorphization (non-crystalline state), leading to inaccuracies in EBSD measurements [110]. Amorphization can impact the quality of diffraction patterns, resulting in complications with indexing and analyzing the crystallographic orientation of the material [110].

Initial polishing attempts applied a pressure of 9 lbF, followed by chemomechanical polishing for a duration of 2 hours (Figure 19). Amorphization of the serpentine matrix was exhibited, whereas the magnetite lattice remained intact (Figure 20). The sample surface was ground off and repolished at 4.5 lbF, based off of a reportedly successful protocol for the polishing of antigorite samples [110]. When EBSD was performed, indexing was not possible for any minerals encompassed in the sample. This could have resulted from a few different phenomena, including insufficient polishing, damage propagation below the surface from the previous test, or over-polishing. Consequently, new thin section samples were generated and

polished minimally, polishing at 3 lbF for 3 min and ultra-polishing for 30 min, in hopes of preventing amorphization. These samples were unable to be indexed and suspected to not have been polished sufficiently. Consequently, the samples were polished for longer, repeating the protocol through for a second time. The resultant samples appeared to have become amorphized.

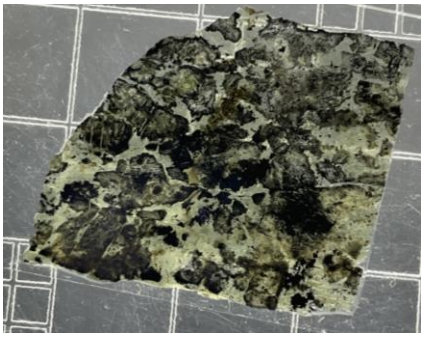

Figure 19. Representation of an awaruite thin section. The sample underwent grinding, polishing, and subsequent chemo-mechanical polishing as described in the methods section.

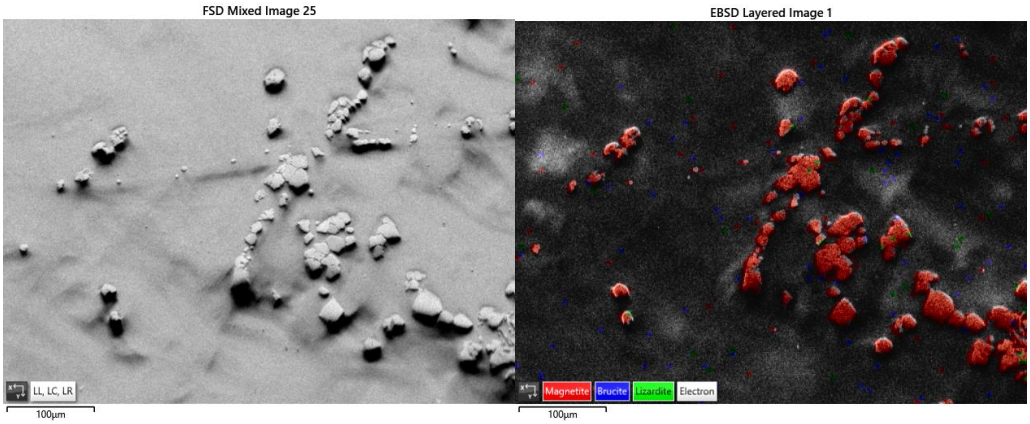

Figure 20. EBSD image of awaruite native ore sample, demonstrating amorphization of serpentine matrix.

Complications in EBSD sample preparation resulted in the inability to quantify the native grain size distribution. The dominant minerals found in the Baptiste deposit include magnetite, serpentinite minerals, heazlewoodite, and awaruite. It has been noted that the primary silicate is lizardite [11]. Among serpentines, the chemical composition is identical, but the crystal structure

is dependent on the thermodynamic environment in which the serpentine was produced. The lattice, consisting of a T-sheet and an O-sheet, can become mismatched thus giving rise to polymorphic serpentine structures. The primary serpentine minerals include chrysotile, lizardite, and antigorite. Structural differences arise from distortion of the T-sheet, SiO_4 tetrahedral, and O-sheets, MgO octahedra. These structural differences present varying material properties, including hardness. Serpentines are typically soft minerals, whereas magnetite has a Mohs hardness of 5.5-6.5. It has been reported that serpentines can be affected by shearing due to polishing [111]. It is also possible the surface was disturbed when cut with the diamond saw, as was exemplified for graphite samples [111] that were further exacerbated through subsequent grinding and polishing steps. A study investigating the damage of serpentine samples during polishing concluded that although pure lizardite provided a clear Kikuchi band, almost no pattern was detected in a mixed serpentinite sample due to a contrast of mineral hardness with surrounding hard minerals [111].

Due to the challenges exhibited with surface polishing, it was not possible to analyze the samples via EBSD. The complexity of varying hardness within the ore deposit indicates alternative preparation methods should be investigated. Once an EBSD sample preparation procedure has been established for this ore deposit, a representative sub-sample needs to be obtained. Course materials require larger sample masses to get representative samples in means of mineralogical composition.

Shape Factor. Variations in particle shape can result from a few different phenomena, including rock structure, mineralogy, and hardness [112]. Particle shape is dependent both on the nature of the material being fractured, as well as the method of stress application used [113]. For

example, the grinding of quartz minerals is distinct between both fine and large particles with respect to fracture equipment used. A roll mill creates elongated and acicular-angular fine particles, whereas a ball mill generates sharp splintered fine particles [114]. The shape of the original particle can also influence the effectiveness of comminution stress application wherein irregular shapes tend to fracture more easily, inducing higher rates of breakage [113]. Often material type is what drives particle shape generation [114]. Mineral phases often adopt distinct shapes; for instance, studies have observed that awaruite has preferred rod-shaped flat orientations [11]. The method of rock fracture may enhance mineral liberation, inducing an increased proportion of native mineral orientations and affecting the overall particle shape distribution. The comparison of particle shape factors generated through different comminution methods can reveal whether preferential and/or distinct fracture patterns are present. Shape morphology influences beneficiation processes, including flotation, electrostatic, gravity, and magnetic separation as well as subsequent leaching behaviors [114]. Distinguishing whether differences between particles generated through the applied comminution methods can inform whether the mechanism of fracture has profound impact on particle shape generation and therefore, potential leaching efficiencies.

Shape factors are dimensionless quantities used to describe the shape of a particle, independent of its size. A particle's shape can be captured through three independent relative scales: form, roundness, and roughness [112]. Form is often characterized through parameters like aspect ratio and sphericity. Aspect ratio is a function of the largest diameter and the smallest diameter orthogonal to it (Eq 7). Sphericity, or circularity (Eq 9), is another measure of form. Combined, these shape factors provide evidence of a particle's elongation wherein increased

aspect ratio and decreased circularity values indicate increased particle elongation. Roundness measures angularity (Eq 8), while solidity is a measure of compactness (Eq 10).

Histograms were used to visually distinguish the distribution between comminution methods, with Table 7A and Table 8A in the Appendix providing a statistical overview for quantitative assessment of the distributions. The sample size was twice as large for the coarse traditional data set. This was due to the analysis being performed on previously referenced BSE images. Despite the same number of sites imaged, tCO_2 had both fewer particles in the field of view as well as fewer particles that were imaged in entirety. Statistically, due to the small sample size, these results would be further substantiated if more images were collected and analyzed via image processing to increase the total number of particles analyzed.

Traditional comminution yielded a greater variability of particles sizes, represented by the area distribution in Figure 21. The mean area for traditional and tCO_2 were approximately 259,000 ± 13,400 and 269,000 ± 13,600 μm^2, respectively.

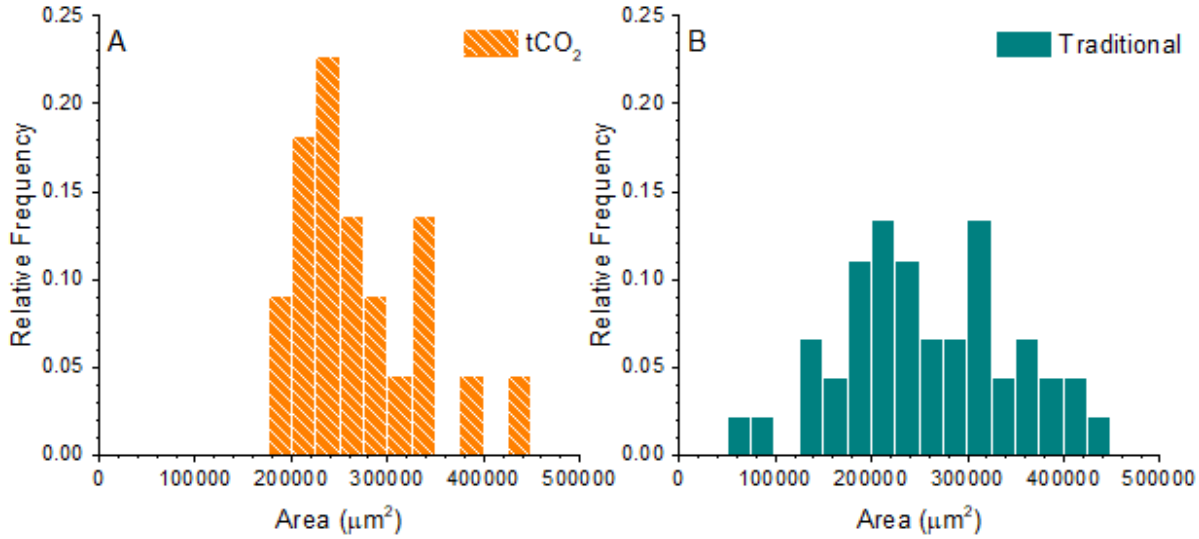

Figure 21. Comparison of the coarse particle area (μm^2) distributions of awaruite particles fractured through tCO_2 and traditional comminution. Particles range in size between 425-500 μm.

Traditional comminution resulted in particles with a higher mean aspect ratio (Figure 22). tCO_2 yielded an aspect ratio of 1.2 with a few outliers at 3.7. The mean aspect ratios were 1.7 and 1.54 for traditional and tCO_2 coarse particles, respectively. tCO_2 shows a wider range of aspect ratios and a high kurtosis, indicating a flatter distribution with a larger proportion of extreme values. The two methods exhibited little difference in roundness (Figure 23), circularity (Figure 24), and solidity (Figure 25) indicating similar compactness and roundness. In general, traditional comminution tended to produce a greater proportion of elongated particles, indicated by the greater mean aspect ratio.

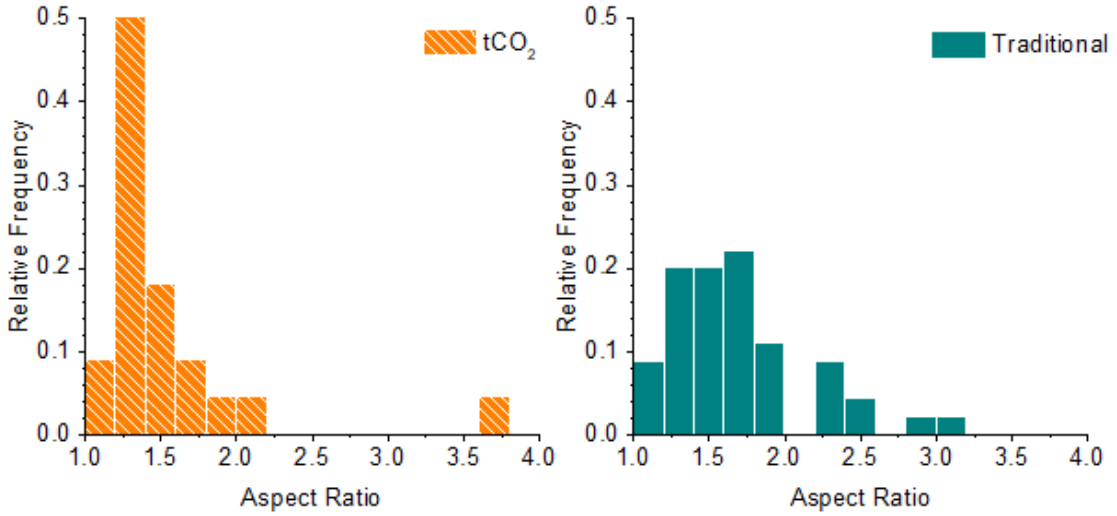

Figure 22. Comparison of aspect ratio distribution of awaruite particles fractured through tCO_2 and traditional comminution. Particles range in size between 425-500 µm.

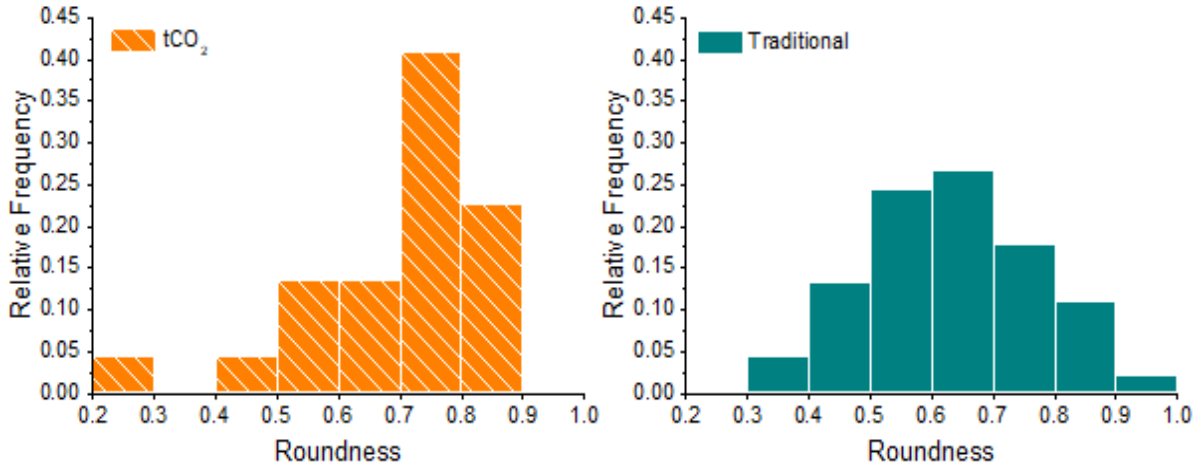

Figure 23. Comparison of roundness distribution of awaruite particles fractured through tCO_2 and traditional comminution. Particles range in size between 425-500 µm.

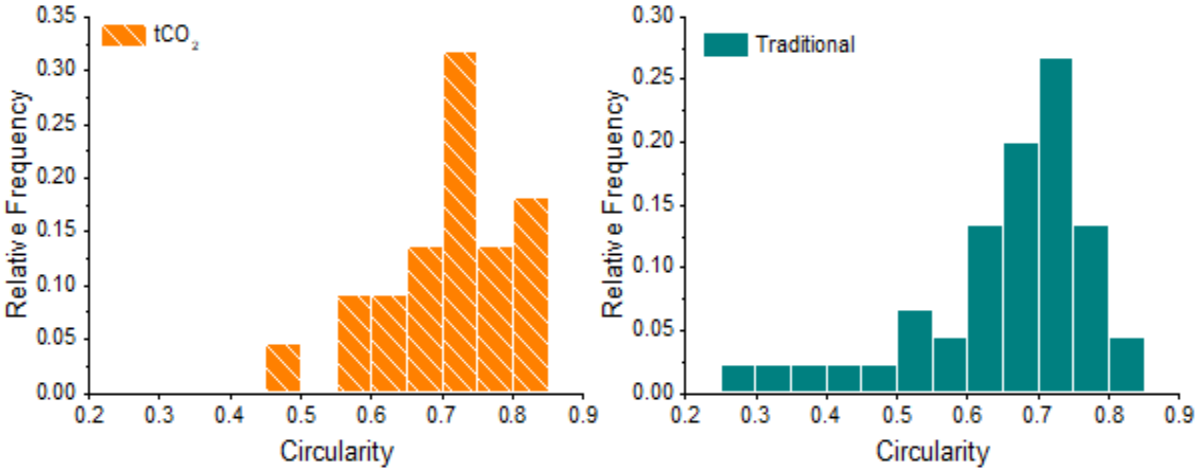

Figure 24. Comparison of circularity distribution of awaruite particles fractured through tCO_2 and traditional comminution. Particles range in size between 425-500 µm.

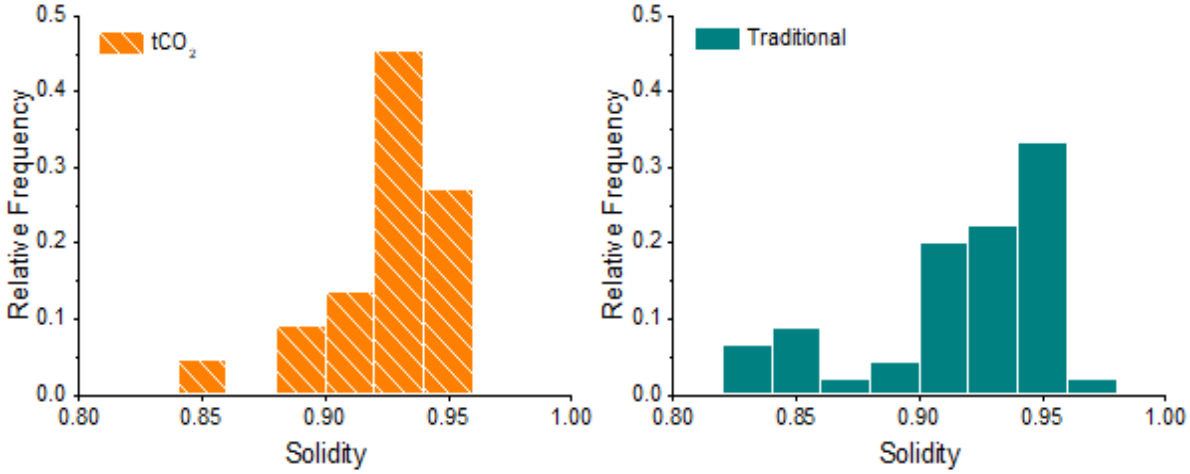

Figure 25. Comparison of solidity distribution of awaruite particles fractured through tCO_2 and traditional comminution. Particles range in size between 425-500 µm.

Interestingly, tCO_2 resulted in an increased frequency of shape factors with similar values across all parameters investigated, represented by >30% of the same value in the histogram. This may indicate a more discriminate fracture of awaruite ore achieved through tCO_2 fracture. Discriminate fracture would likely result in increased mineral liberation. Mineral liberation has profound impacts on downstream processing, with high degrees of liberation resulting in

increased mineral concentration efficiencies. This result may explain the increased magnetic concentration achieved for tCO_2 samples.

Finer particles exhibited less pronounced differences between comminution method. The mean and median area for traditional comminution were both higher, measured at 9920 ± 129 μm^2 and 9310 μm^2 as compared to 6110 ± 106 μm^2 and 4700 μm^2 for tCO_2 (Figure 26). Although tCO_2 samples were sieved to a larger grain size fraction, 90-125 µm compared to 75-125 µm for traditional, the overall area of the particles was smaller. This could have resulted from sample storage differences or instead could indicate the tCO_2 samples require extended sieving periods. There was a particularly large distribution of tCO_2 particles exhibiting an area between 0-5000 μm^2.

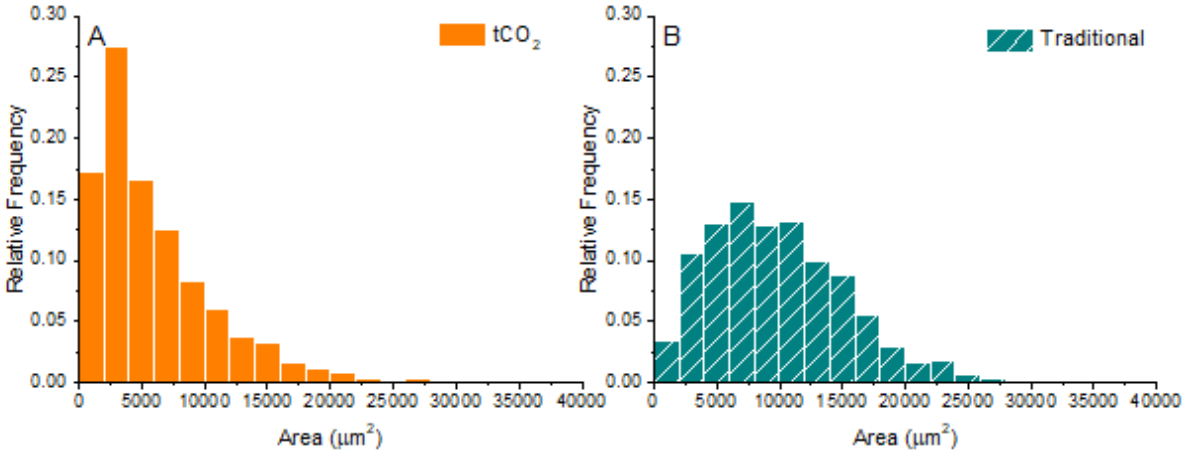

Figure 26. Comparison of fine particle area (μm_2) distributions of awaruite particles fractured through tCO_2 and traditional comminution. Particles range in size between 90-125 µm and 75-125 µm for tCO_2 and traditional, respectively.

Despite exhibiting similar central tendencies, the aspect ratio of tCO_2 particles had a substantially greater range, slightly greater skew, and a large kurtosis value, or measure of the shape of a distribution's tails in relation to the overall shape (Figure 27). Both comminution

methods generated uniform particles, indicated through circularity (Figure 28), and mean roundness values of 0.60 (Figure 29). Similarly, there was not substantial deviation in solidity between comminution methods (Figure 30).

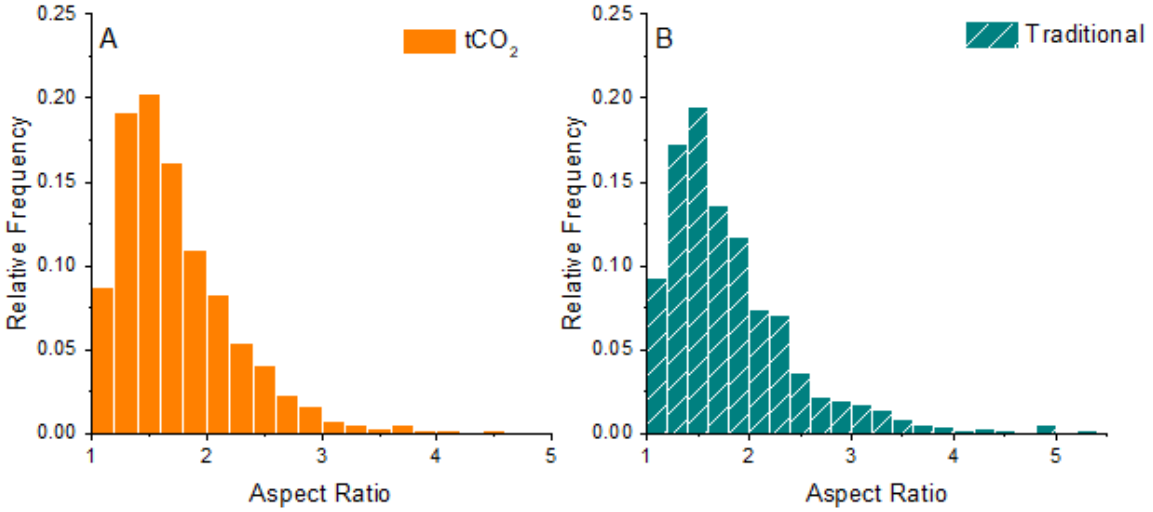

Figure 27. Comparison of fine particle aspect ratio distributions of awaruite particles fractured through tCO_2 and traditional comminution. Particles range in size between 90-125 µm and 75-125 µm for tCO_2 and traditional, respectively.

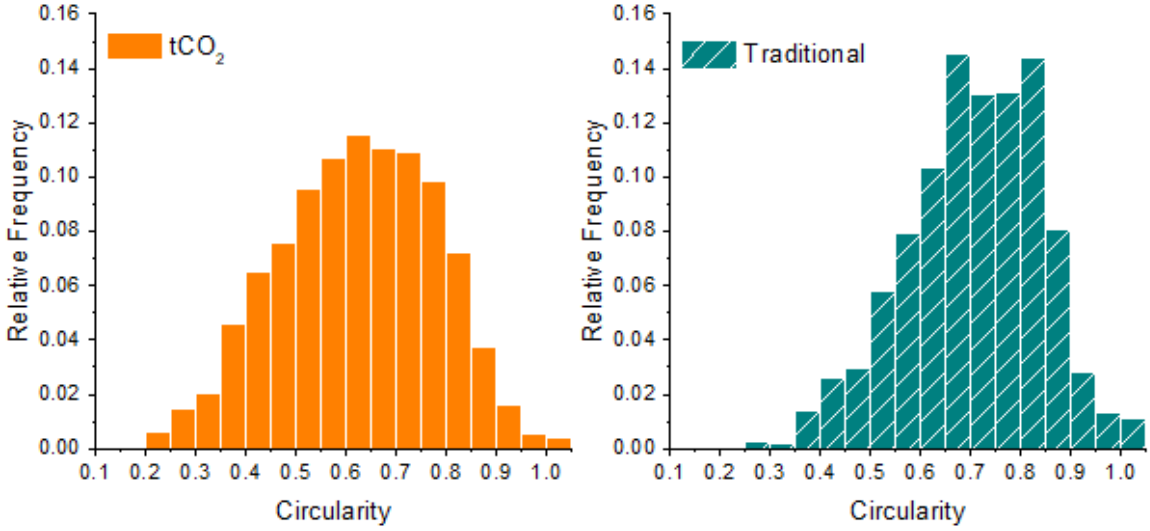

Figure 28. Comparison of fine particle circularity distributions of awaruite particles fractured through tCO_2 and traditional comminution. Particles range in size between 90-125 µm and 75-125 µm for tCO_2 and traditional, respectively.

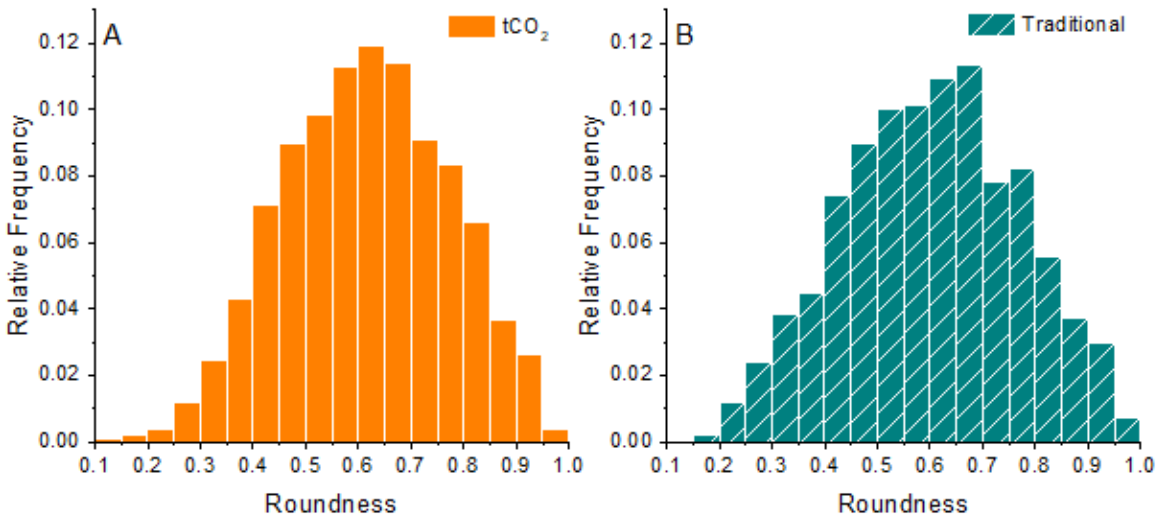

Figure 29. Comparison of fine particle roundness distributions of awaruite particles fractured through tCO_2 and traditional comminution. Particles range in size between 90-125 µm and 75-125 µm for tCO_2 and traditional, respectively.

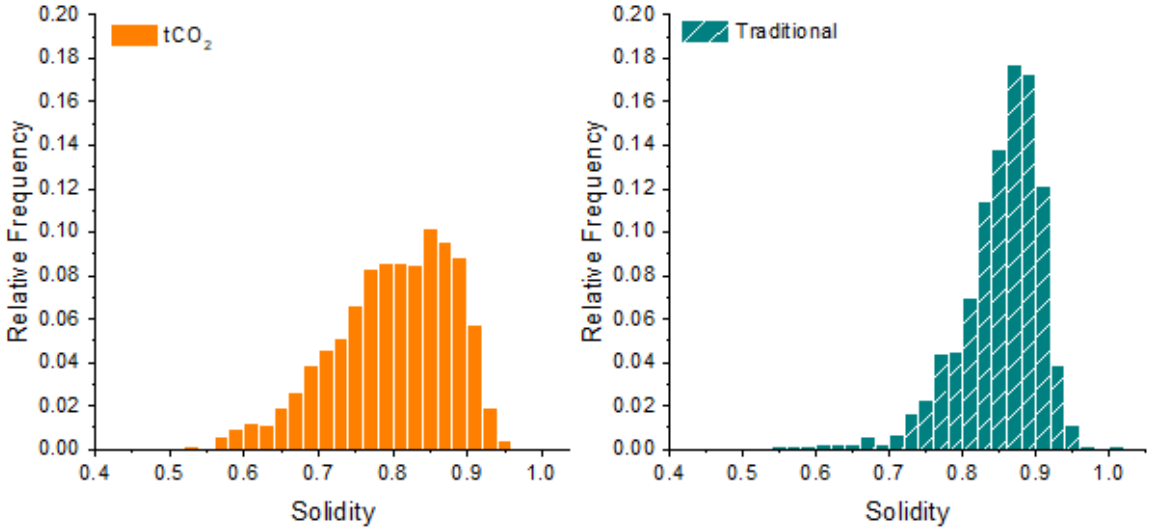

Figure 30. Comparison of fine particle solidity distributions of awaruite particles fractured through tCO_2 and traditional comminution. Particles range in size between 90-125 µm and 75-125 µm for tCO_2 and traditional, respectively.

The most distinguishable difference in shape factor across particle sizes between comminution methods lied in the aspect ratio, with tCO_2 exhibiting large kurtosis values for both the fine and coarse particles. In the case of fine particles, this distribution of extreme aspect

ratios could be a result of the increased number of disaggregated awaruite particles visualized in Figure 16J, 16N. Similarities between solidity and roundness could have propagated from thresholding biases. Manual segmentation was required to distinguish between particles when Watershed or Biovoxxel were unable to differentiate particle boundaries. As a result, some of the surface angularity may have been lost.

A greater physical distinction between comminution methods was identified in the coarser particles, with tCO_2 fracture resulting in increased similarities in shape factor propagation. This finding suggests tCO_2 may lead to a more selective ore fracture, likely enhancing mineral liberation efficiencies. Increased mineral liberation correlates with higher ore concentration, as demonstrated in the case of tCO_2 comminuted samples across both coarse and fine particles.

Discussion

Although there was not a clear physical distinction between particles obtained under the varying comminution methods, there is preliminary evidence ore concentration is impacted by fracture method. Through SEM analyses, it was determined concentration efforts were most effective under tCO_2 comminution conditions. This was demonstrated through the comparison of BSE and EDS images among samples. The relative high value product for each respective image was determined through image analysis. tCO_2 demonstrated increased proportions of high value product, as well as nickel content, when compared to traditional comminution samples across both particle size ranges investigated. Refinement of particle size resulted in increased liberation in both cases. Shape factor analyses indicate that coarse particle generated through tCO_2 fracture resulted in increased similarities among particles. Similarities among particles may explain the

increased mineral liberation and concentration efficiencies observed for tCO_2 comminution conditions.

The visualization of higher proportion product in tCO_2 samples indicate it may be a promising technology for increased liberation and ore pre-concentration prior to downstream leaching processes. Preliminary investigations indicate the tCO_2 ore was more amenable to magnetic concentration, indicated by increased proportions of bright spots relative to darks spots in the BSE images. If these results are representative, not only would this technology likely decrease subsequent ore processing procedures, but the energy expenditure to perform the comminution is potentially substantially decreased [10]. The overall low concentrations of high value ore indicate further beneficiation processes are necessary. Additionally, an inability to distinguish particles, based on physical characteristics, generated through the different comminution methods indicates leaching studies need to be performed to ultimately determine whether efficiencies are impacted by the fracture method.

AWARUITE LEACHING

Nickel is a vital metal with industrial applications in the manufacturing of stainless steel and other alloys [115]. It is expected that nickel demand will only increase with the surge of electric vehicles due to its utilization in lithium-nickel-cobalt-aluminum and lithium-nickel-manganese-cobalt batteries [116]. Demand, within the electric vehicle industry alone, is expected to increase nickel demand by 2.6Mt Ni to 2040 [116]. Notably, all nickel ore deposits have relatively low nickel content, most clearly demonstrated by a high grade classification only containing about 1.8% Ni [116]. Although the main source of nickel has primarily relied on the mining of sulfidic ore deposits, laterite ore comprises 72% of global nickel reserves [117]. Despite the large relevance of laterite ore, these deposits only account for about 40% of the global nickel production due to low processing efficiencies due to difficulties in their processing [117]. This is largely due to low nickel content and a high abundance of silicates [116].

Alternatively, awaruite is a nickel iron alloy (Ni_3Fe) distributed across a few reserves globally. The high abundance of Ni in the awaruite ore makes it a good option for alternative nickel resources. Although nickel is highly concentrated in the awaruite mineral phase, the lack of a standardized processing method and challenges associated with its isolation from magnetite make it difficult to isolate the mineral [106]. As a result, the overall ore deposit exhibits low grades. In a press release from September 2022, FPX Nickel classified their nickel into low (0.06-0.10% Ni), medium (0.10-0.14% Ni), and high-grade (>0.14% Ni) shells.

The application of bioleaching is often associated with increased yields with low operational costs, making it a viable option for the leaching of low-grade ore. Bioleaching has been demonstrated to be effective in the leaching of laterite [41, 116, 118]. The primary objective

of this study is to understand the viability of abiotic hydrometallurgical recovery of nickel from awaruite ore with the eventual goal of cell-free hydrometallurgical application. The previous chapter investigated differences in "daughter particles" between tCO_2 and traditional comminution methods, wherein tensile and compressive fracture are achieved, respectively. Through this study, it was determined particles were more amenable to magnetic concentration resulting from tensile fracture. Along with investigating leachability, the study aims to determine whether recovery yields differ between comminution methods to determine whether comminution type impacts downstream leaching efficiencies. Gluconic acid was used to perform abiotic hydrometallurgical leaching to determine optimized processing parameters for future bioleaching implementation.

Current detection methods include AAS, ICPMS, TXRF, or ICP-OES [119]. Although these analytical methods can detect multiple elements at relatively low detection limits, there are high capital costs, time consuming method development, and requirement of a trained analyst to enable their implementation. Alternatively, the development of a colorimetric assay to determine nickel concentrations in leachate samples would provide a high-throughput solution to quickly determine the impact on recovery due to variations of leaching process parameters. Colorimetric methods rely on the measurement of light absorption at a particular wavelength, as a proxy for concentration, of colored species in solution. Some nickel detection colorimetric methods implement the use of DMG [120], silver nanoparticles [121], or gold nanoparticles [122]. The work discussed here is based off the chelation activity of beta-mercaptoethanol (βME). βME, C_2H_6OS, has been demonstrated to be effective in urease inhibition through the chelation with nickel active site [123, 124].

Colorimetric Assay Validation

The βME forms a complex with nickel in the presence of sodium borate buffer with strong absorbance bands from 300 to 600 nm. Absorbance at both 330 nm and 405 nm were measured before the addition of βME and 30 minutes following βME addition to the wells. A slight visual difference was detected (Figure 31). A standard curve was prepared in triplicate to determine the concentration of nickel solution in a sample. The assay was repeatable and robust, exhibiting the same trend in detection both when performed days apart (Figure 32A) and when sampled variably over the course of approximately one day (Figure 32B). The assay did not exhibit a change in absorbance over the course of the period investigated, indicating a strict measurement 30 minutes following βME addition was not necessary. Although the standard curve developed at a wavelength of 330 nm is displayed, a standard curve was also generated at a wavelength of 405 nm (Appendix Figure A.5). The standard curve was not as linear after ~375 nmol Ni. Although linearity was still achieved, the signal at 405 nm was far lower than what was exhibited at 330 nm as indicated by a smaller slope. Notably, the absorbance measured at both wavelengths prior to addition of the assay reagent were nominally 0.00. The assay was therefore characterized by the absorbance measured after addition of βME.

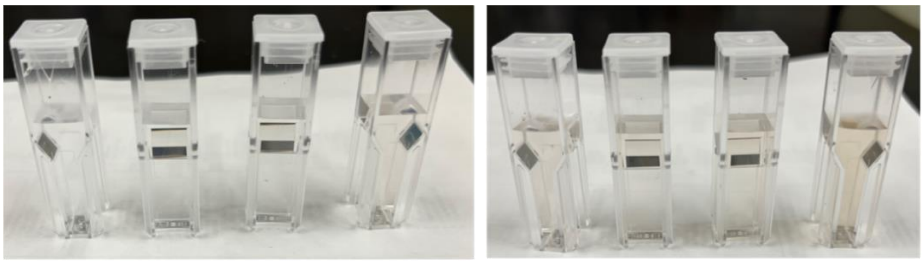

Figure 31. Cuvette 30 minutes following βME addition. Nickel concentration increases from left (0 nmol) to right (525 nmol). Nickel standard and sodium borate were added to the cuvette followed by 75 µL of βME. This image was captured 30 minutes after βME addition.

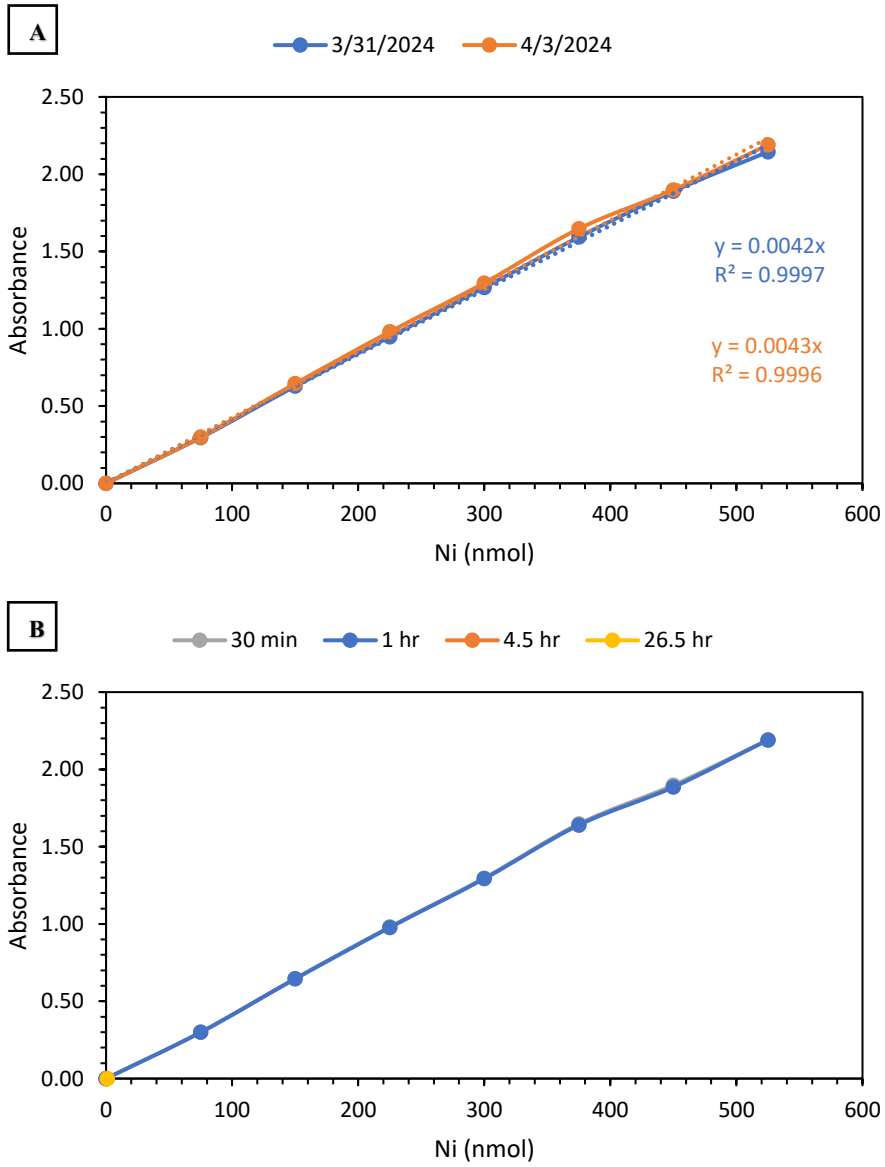

Figure 32. Nickel standard curve development. Nickel at varying concentrations was applied to the cuvette and topped off with sodium borate until the total volume was 1.5 mL. 75 µL of βME were added to each cuvette and mixed. Figure A demonstrates a consistent signal measured on different days and Figure B demonstrates the ability to extend measurement over at least a 26.5 h time-period following βME addition.

The high concentration of iron in the awaruite samples necessitated an investigation into iron inhibition. A standard curve was developed under the same conditions used for nickel, but the nickel was substituted with iron. Measurement of the absorbance prior to βME addition,

wherein the only reagents in the cuvettes were iron standard of varying concentration topped off with sodium borate buffer to reach a final volume of 1.5 mL, resulted in a 2nd order polynomial fit for absorbance measured at 330 nm and 405 nm. The presence of iron in the cuvettes resulted in a yellowish hue, increasing in shade as concentration increased, that was not previously seen under solely nickel conditions (Figure 33A). 30 minutes following βME application, the solution turned more of a reddish brown (Figure 33B). Absorbance measurements reflected the increased hue associated with iron concentration in the pre-βME absorbance measurements under both wavelengths, 330nm and 405nm (Figure 34A). Similarly to the nickel standard curve, the absorbance was measured 30 minutes following βME application (Figure 34B).

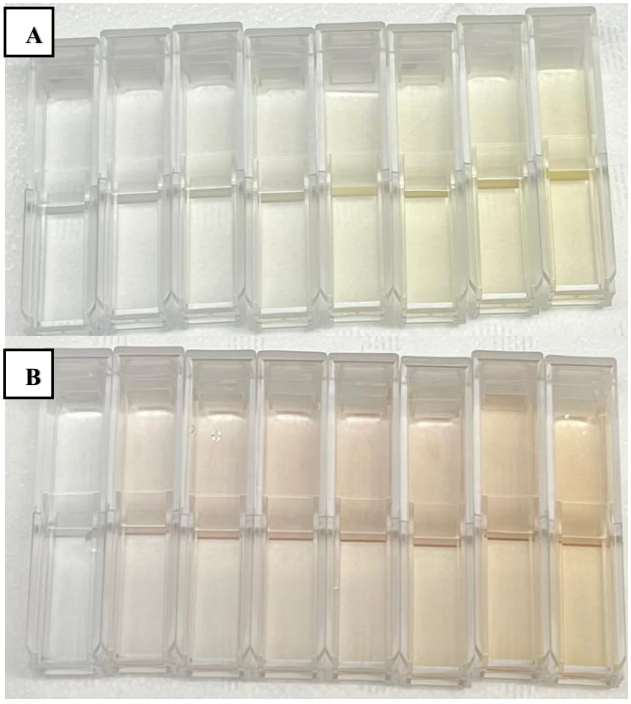

Figure 33. Color change with increasing iron concentration visualized both pre (A) and post (B) βME application. The iron concentration is increased incrementally by 75 nmol from left to right for both images, with the first cuvette composed of the blank sodium borate solution.

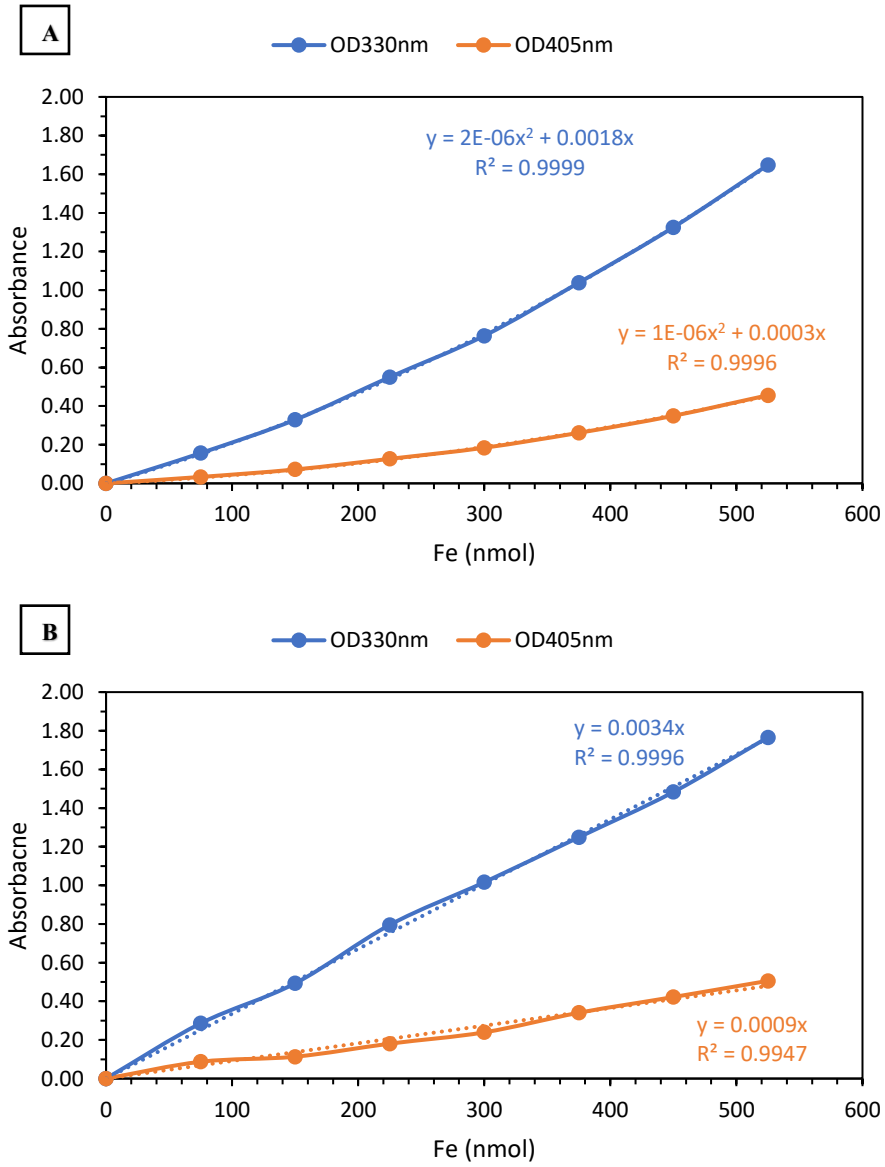

Figure 34. Absorbance measurements at 330 nm and 405 nm both pre-βME (A) and 30 minutes following βME application (B) with increasing iron concentration. Iron at varying concentrations was applied to the cuvette and topped off with sodium borate until the total volume was 1.5 mL. 75 uL of βME were added to each cuvette and mixed. Standard curves for the pre-βME application best fit a 2nd order polynomial whereas post-BME is represented by linear curve fit.

To account for assay application toward leachate samples, wherein iron concentration has not been predetermined and is likely present, the pre-βME absorbance was plotted against subsequent post-βME absorbance (Figure 35). Under both 330 nm and 405 nm wavelengths, the

signal is represented a 2nd order polynomial fit. The signal detected prior to βME addition, attributed to iron, can be used to predict the expected response following βME addition. This would allow for the removal of the iron signal from the total signal, resulting in the isolation of nickel signal. Theoretically, these curves can be utilized to correlate initial iron concentrations with subsequent assay signal measurements, enabling the differentiation between nickel and iron signals.

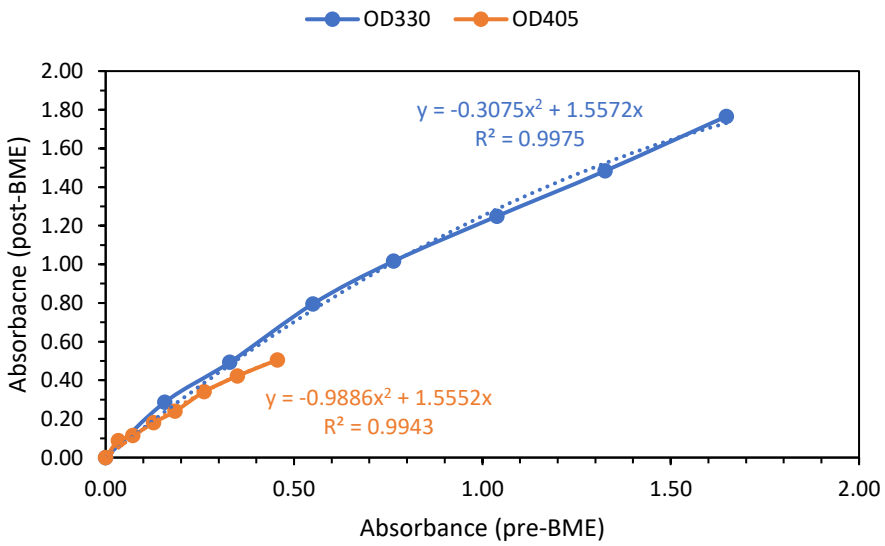

Figure 35. Pre-βME absorbance plotted against post-βME addition absorbance to demonstrate how iron presence impacts subsequent absorbance measurements.

Similarly, cobalt is inhibitory above a cobalt concentration of 375 nmol, the trend is no longer consistent indicating the concentration can no longer be accounted for past that point. (Appendix Figure A.6 and A.7).

Awaruite Leaching Studies

The leaching of awaruite samples was performed to determine possible leaching efficiencies and provide a basis for comparison between traditionally and tCO_2 comminuted ore. The pH was measured at the end of the 5-day leaching period (Table 33). Across all conditions an increase in pH was visualized, indicating there was at least some dissolution activity occurring. An increase in pH was also observed for traditional comminution samples leached for both 1 and 3 days (Appendix Table 9A). A change of pH provided preliminary evidence that at least some activity had occurred over the course of the applied leaching duration. The trend in pH deviated between samples. tCO_2 comminuted sample resulted in increasing pH deviation as particle size decreased, whereas the traditional comminuted samples exhibit the opposite. Additionally, as gluconic acid concentration was increased, tCO_2 samples exhibited decreased differences in pH where the opposite is true for traditional samples.

Table 33. pH increase measured at Day 5 for both tCO_2 and traditional leachate samples. pH was averaged across the three samples from each condition. The initial pH measured for the 75 mM and 105 mM calcium gluconate standards were 5.97 and 6.03, respectively.

	Particle Size (μm)	Calcium Gluconate (mM)	pH Change	Error
tCO_2	90-125	75	2.40	0.15
	90-125	105	2.33	0.01
	212-300	75	2.20	0.01
	212-300	105	1.77	0.23
	425-500	75	1.76	0.04
	425-500	105	1.62	0.05
Traditional	75-125	75	1.30	0.04
	75-125	105	1.32	0.03
	212-300	75	2.21	0.04
	212-300	105	1.85	0.01
	425-500	75	2.47	0.12
	425-500	105	1.98	0.06

To determine nickel concentration using the βME colorimetric assay, samples were spiked with a known concentration of nickel standard to determine whether a linear trend still existed (Figure 36). A sample volume of 75 µL resulted in an indistinguishable line from the nickel standard curve, indicating undetectable nickel concentrations at the added volume. As the sample volume was increased the trend remained consistent with the standard curve but the absorbance measurements increased slightly. A lack of signal from the sample indicated the sample contained low concentrations of nickel that were ultimately washed out by the signal of the nickel standard. This trend was consistent across 4 separate leachate samples (Appendix Figure A.9-A.11).

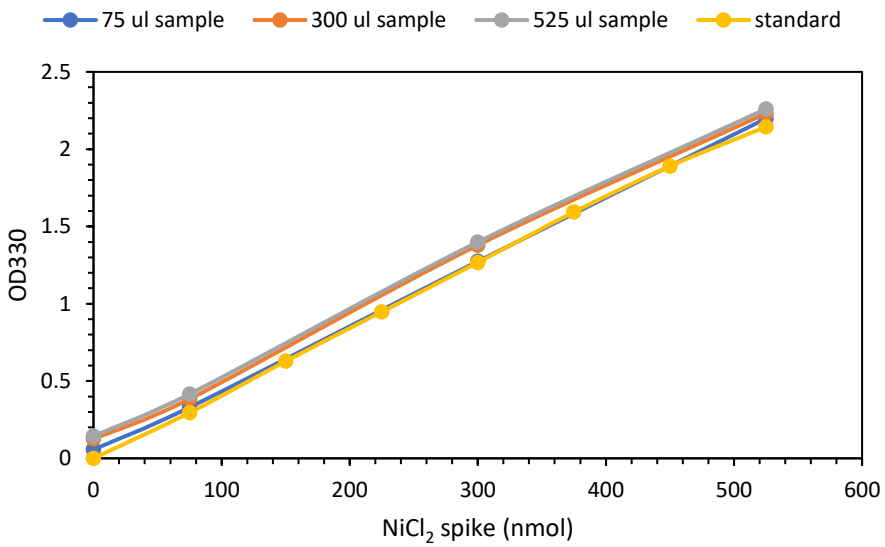

Figure 36. Varying volumes of leachate sample were spiked with $NiCl_2$ standard. The x-axis represents the concentration of the nickel spike, where points plotted at a value of 0.00 nmol do not contain excess nickel. The absorbance was measured at a wavelength of 330 nm. The nickel standard curve is plotted for reference.

By spiking 1 mL of leachate samples with lower concentrations of nickel, ranging between 18.75 and 75 nmol, the trend remained the same although the sample signal was a little

more distinct (Figure 37). The standard curve at lower concentrations of nickel was performed in conjunction, validating the linear range of the assay extended below 75 nmol.

Ultimately, these results provide evidence the concentration of nickel in the leachate sample were very low. The samples were also spiked with varying concentrations of iron. The resulting trends were both dissimilar from the iron standard curve (Figure 38) and the nickel standard curve. Again, the signal at 405 nm for both nickel and iron spiked samples deviated from the standard curve.

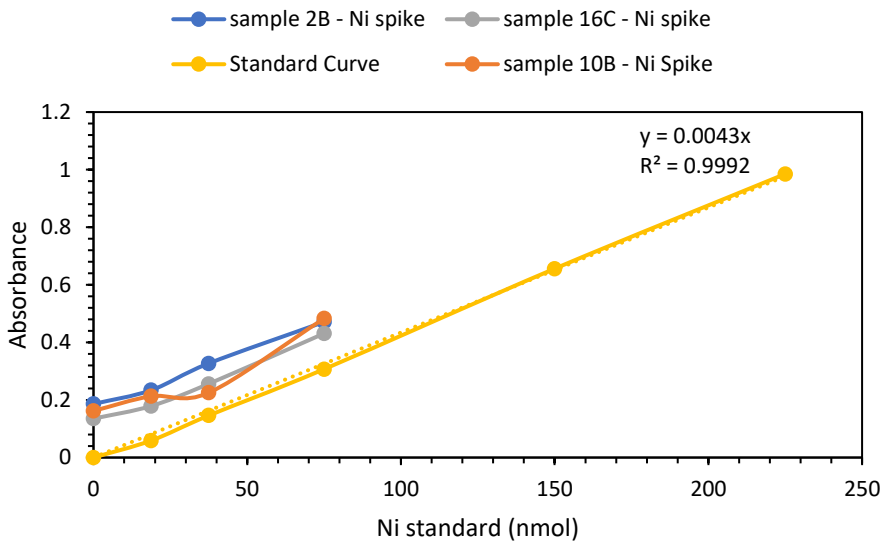

Figure 37. Leachate samples at a volume of 1 mL were spiked with varying concentrations of 1 mM Ni standard. Absorbance was measured at a wavelength of 330 nm. The nickel standard curve is plotted for reference.

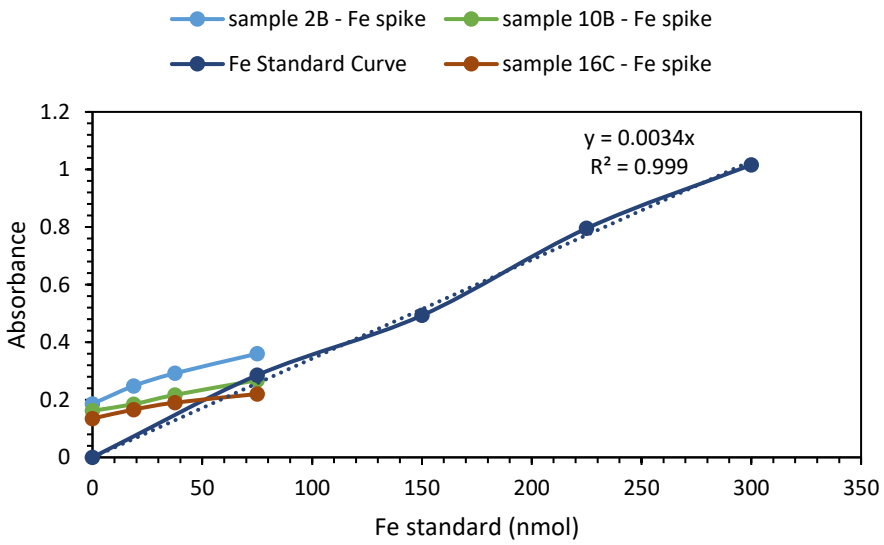

Figure 38. Leachate samples at a volume of 1 mL were spiked with varying concentrations of 1 mM Fe standard. Absorbance was measured at a wavelength of 330 nm.

It is clear the presence of both nickel and iron in the assay complicates results. Prior to the addition of βME, the absorbance measured at 330 nm remains consistent despite being spiked with added nickel concentration. Addition of the chelator results in discrepancies of the results, with the absorbance often not increasing above the pre-βME approximation. Alternatively, removal of iron signal utilizing the signal measured at a wavelength of 405 nm is not applicable due to the lack of signal at low concentrations and large increased signal visualized for un-spiked samples. Therefore, removal of the iron signal using the polynomial trend indicated in Figure 35 is not applicable to determine sample nickel concentrations. Nonetheless a few different methods were attempted to try to remove spiked signals and achieve representative results as observed in un-spiked sampled.

Case 1: Removal of Iron Signal using OD405 pre-βME Measurement

The iron concentration was first measured, using the OD405 pre-βME absorbance, with the following equation:

$$y = -1795x^2 + 1948.7x \quad \text{(Eq 15)}$$

where x is the absorbance and y is the Fe concentration (nmol). The equation is a reconfiguration of the OD405 polynomial fit displayed in Figure 34A to solve for concentration. This measurement was then used to determine the corresponding OD330 post-βME signal associated with the determined Fe concentration. The OD330 Nickel standard curve (Figure 32A) was used. Once this signal was subtracted from the OD330 measurement to determine the signal associated with Ni, the Ni content was measured. Across all conditions (un-spiked samples, iron spiked samples, and nickel samples) a negative nickel concentration was determined.

Case 2: Removal of Iron Signal using OD330 pre-βME Measurement

The iron concentration was first measured using the OD330 pre-βME absorbance with the following equation:

$$y = -85.166 + 455.92x \quad \text{(Eq 16)}$$

where x is the absorbance and y is the Fe concentration (nmol). The equation is a reconfiguration of the OD330 polynomial fit displayed in Figure 34A. This measurement was then used to determine the corresponding OD405 post-βME signal associated with the determined Fe concentration. The OD405 Nickel standard curve (Figure A.5) was used. Similarly, across all condition a negative nickel concentration was determined.

The demonstration of negative values for both Case 1 and Case 2 may indicate there is a lack of nickel in the sample. As a result, the samples were treated as if nickel was not present in the leachate samples.

Case 3: Determination of Iron Concentration

For this case, it was assumed that nickel was not present in the sample. The OD330 measurement was used. The signal associated with the Ni spike was subtracted, followed by the determination of iron concentration in the sample. The iron spike was removed from iron spiked samples. The results, demonstrated in Table 34, indicate presence of iron and nickel complicate the assay and ultimately, the concentration of nickel and iron in the leachate samples is unable to be determined.

Table 34. Fe concentration determined by OD330 post-βME absorbance across un-spiked sample, spiked Fe samples, and spike Ni samples. The Fe concentration displayed has removed the Fe and Ni spiked signal.

	Fe spike (nmol)	Ni spike (nmol)	Measured Fe (nmol)
2B	-	-	54.71
	18.74	-	54.20
	37.48	-	48.40
	75.00	-	30.88
	-	18.74	45.67
	-	37.48	49.88
	-	75.00	45.88
10B	-	-	47.65
	18.74	-	35.67
	37.48	-	26.34
	75.00	-	3.824
	-	18.74	39.50
	-	37.48	19.88
	-	75.00	49.42

Table 34 Continued. Fe concentration determined by OD330 post-βME absorbance across un-spiked sample, spiked Fe samples, and spike Ni samples. The Fe concentration displayed has removed the Fe and Ni spiked signal.

	Fe spike (nmol)	Ni spike (nmol)	Measured Fe (nmol)
16C	-	-	39.71
	18.74	-	30.08
	37.48	-	18.40
	75.00	-	-10.29
	-	18.74	29.50
	-	37.48	29.00
	-	75.00	34.12

Case 4: Pre-BME OD330 Trends

A consistent trend was observed across Fe-spiked samples in pre-βME absorbances (Figure 39). Fe-spiked samples exhibit a linear trend as iron concentration is increased whereas Ni-spiked samples, plotted at an Fe-spiked concentration of 0.00 nmol, indicating a lack of nickel interference in this measurement. The results are also demonstrated in Table 35 for reference.

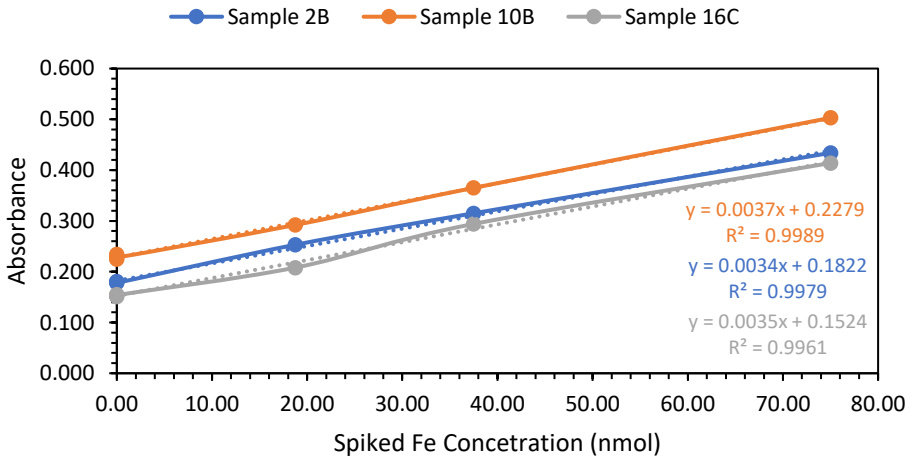

Figure 39. Absorbance, measured at 330 nm, prior to βME addition for both Fe and Ni-spiked leachate samples.

Despite following a linear trend, the pre-βME OD330 measurements do not follow the same linearity observed when solely iron is present. The only change between measurements, plotted in Figure 39, is the increased concentration of iron. Therefore, it is expected that the slope would align with the iron standard curve, due to the lack of nickel signal in this pre-βME measurement. A standardized sample volume across measurements of 1 mL makes it unlikely the reason for these discrepancies is a result of cobalt inhibition. It is likely there is an inhibitory factor that has not been considered, possibly the presence of gluconic acid in the leachate. Gluconic acid is a chelator, thus it is possible the signal is impacted by its presence.

Table 35. Leachate samples, 1 mL, were spiked with iron and nickel at varying concentrations. The OD was measured at 330 nm prior to βME addition.

Sample	Fe-spike (nmol)	Ni-spike (nmol)	OD330
2B	-	-	0.178
	-	18.74	0.181
	-	37.48	0.180
	-	75.00	0.178
	18.74	-	0.253
	37.48	-	0.315
	75.00	-	0.434
10B	-	-	2.34
	-	18.74	0.225
	-	37.48	0.234
	-	75.00	0.228
	18.74	-	0.292
	37.48	-	0.365
	75.00	-	0.503
16C	-	-	0.142
	-	18.74	0.155
	-	37.48	0.151
	-	75.00	0.154
	18.74	-	0.208
	37.48	-	0.294
	75.00	-	0.414

An inability to distinguish between interferences in the post-βME absorbance necessitated the use of the pre-βME absorbance to measure iron concentration. This measurement does not reflect actual iron concentrations in the sample but was instead used as a proxy to determine relative effectiveness over each leaching process. It is hypothesized that this is possible due to the exhibited linear increases in signal as iron concentration is increased (Figure 39).

Leaching Efficiencies

The iron concentration was estimated using the OD330nm polynomial fit in Figure 34A to develop a qualitative comparison of leaching yields across the samples tested. Although these values are not representative of the actual leaching yields, they provide a preliminary qualitative understanding of the relative effectiveness achieved across the various leaching conditions. Figure 40 displays relative iron leaching yields for the traditional comminution samples. The data demonstrates a trend correlated with particle size, gluconic acid concentration, and leaching time. Leaching efficiencies increase with decreasing particle size, increasing gluconic acid concentration, and increased leaching periods.

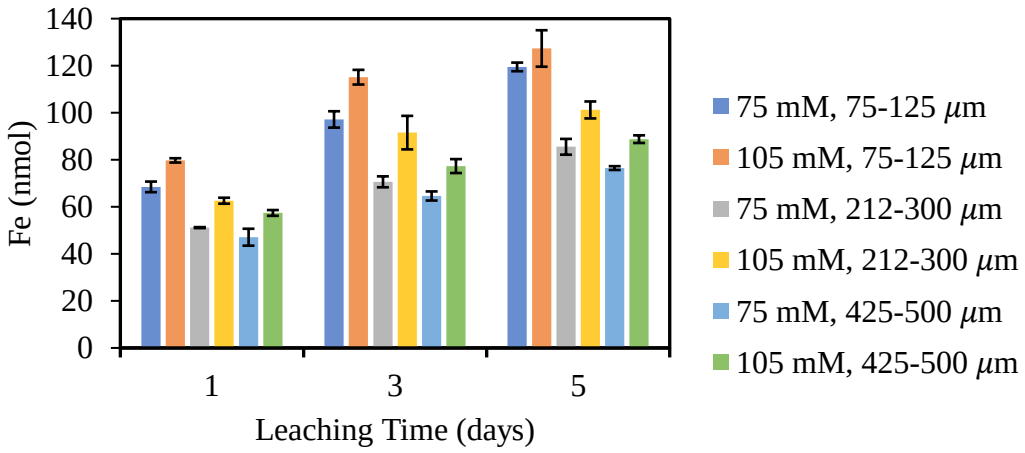

Figure 40. Leachate iron concentrations measured through the colorimetric assay. The results demonstrated are for traditional comminution samples.

Comparison of leaching efficiencies across comminution methods demonstrate relative iron concentration was increased with the application of tCO_2 samples (Figure 41). Similarly, as particle size is decreased and gluconic acid concentration is increased, tCO_2 leaching yields are increased. Ultimately, further validation of the colorimetric assay needs to be conducted to determine the extent of increased recovery and furthermore, nickel leaching efficiencies.

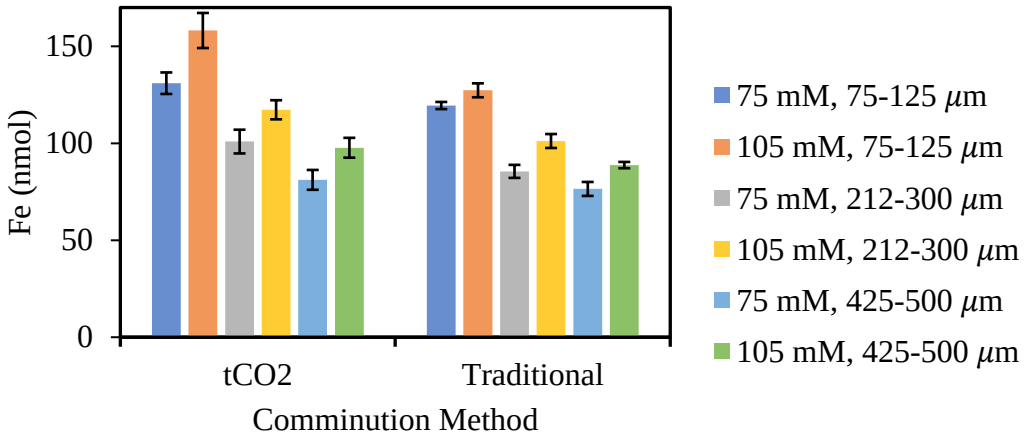

Figure 41. Comparison of tCO_2 and traditional comminuted sample leaching efficiencies. Demonstrated are the leaching yields achieved for a 5-day leaching period, represented by iron concentration (nmol).

Discussion

Leaching conditions were varied through particle size, gluconic acid concentration, and leaching time. An increase in pH exhibited by the end of the leaching period indicates some dissolution is occurring. The initial pH measured for the 75 mM and 105 mM gluconic acid standards were 5.97 and 6.03, respectively. The high initial pH is due to the use of calcium gluconate, where the presence of calcium salt results in an increased pH. Future leaching experiments should utilize either a different form of gluconic acid or acidify the lixiviant to promote increased leaching efficiencies. The large role of acidolysis is promoted under acidic conditions, therefore leaching efficiencies would be higher than what was possible under the conditions implemented in this study.

The determination of nickel and iron concentrations were not able to be obtained using the βME colorimetric assay. It is likely there are multiple inhibitory factors that have compounded the signal, resulting in the inability to quantify these components. An inability to discern between signals of different components likely present in the samples indicates the assay requires further synthesis prior to its implementation for leachate samples. It is also possible gluconic acid present in the leachate is inhibitory, and thus the βME is unable to chelate with nickel or iron present. Alternatively, the concentrations of the leachate could have been extremely low due to a combination of high lixiviant pH and the low ore concentration yields of the feedstock, as demonstrated in the previous chapter.

The primary objective of this study was to determine whether differences in comminution methods impact downstream processing efforts. The inability to quantify leaching efficiencies does not allow for this direct comparison to be made. Alternatively, changes of the pre-βME

absorbance (measured at a wavelength of 330 nm) were used to qualitatively determine leaching yields. This measurement, although likely not reflective of the scale of leaching performance due to differences in signal slope visualized between the standard curve and spiked samples, provides preliminary evidence that there is a difference between leaching yields. Ultimately, these results need to be validated through alternative tests, such as AAS and ICPMS, or through more extensive assay validation to discern signal propagation.

CONCLUSIONS

The investigation of variable media conditions, through the substitution of YE for KH_2PO_4 in a modified Pkm medium, resulted in substantially increased microbial growth. However, the impact on acid production was less profound, with gluconic acid production not directly correlating with the increased growth exhibited. Under both conditions where YE was the sole phosphorus source, the acetic, citric, and succinic acid concentrations were increased but minimal differences were observed for gluconic acid concentrations.

The cell-free supernatant generated through these studies was applied to two different feedstocks, LIB and magnetic swarf. LIB and magnetic swarf leaching conditions were different, wherein the gluconic acid concentration was standardized to different concentrations and the time, temperature, and pulp densities differed. This did not allow for a direct comparison across leaching efficiencies but instead the leaching trends were compared across feedstocks to theorize how variable media conditions impacted subsequent leaching processes. The substitution of YE had a more profound impact on leaching in magnetic swarf applications, with leaching efficiencies increasing substantially as bacterial cultivation time was increased to 72 h. This impact on leaching yields was not discernable upon the application of the 48 h biolixiviant. Under Pkm conditions, the biolxiviant did not result in substantial differences in the yield of swarf elements between cultivation periods. This indicated there was a change in the biolxiviant between cultivation periods that promoted the recovery of REEs from the feedstock. Alternatively, phosphorus source appeared to have a less substantial impact on the recovery of base metals from LIBs, with leaching yields remaining high across all applied biolixiviants.

Ultimately, this indicated the biolixiviant compositional changes resulting from the substitution of YE was most effective in the solubilization of REE.

The viability of nickel recovery from awaruite ore, located in the Baptiste deposit in British Columbia, was investigated. Awaruite, Ni_3Fe, contains high proportions of nickel making it a viable resource for nickel extraction. Two comminution methods, traditional and tCO_2, were investigated to determine whether physical differences existed between particles generated by the different fracture techniques. tCO_2 achieves rock fracture by overcoming tensile forces in the ore body, which may save energy, therefore it's utilization would be further substantiated if there was additional benefit for downstream processing. It was hypothesized that due to the method of fracture, the ore body is broken along grain boundaries. To test this hypothesis, a series of tests were used to identify whether physical differences in particle generation were present as a result of rock fracture method. Although there were no discernable physical distinctions between samples, there is preliminary evidence to suggest tCO_2 promotes increased ore concentration. Through a combination of BSE and EDS analyses, it was determined that the tCO_2 ore contained higher proportions of high value product, suggesting the ore was more amenable to magnetic concentration. Shape factor analyses revealed tCO_2 generated a greater frequency of similar coarse particles, indicating the fracture method is likely more selective than traditional comminution. Discriminate fracture would likely enhance mineral liberation and therefore ore concentration efficiencies.

Lastly, to investigate the impact of comminution method on downstream leaching processes, a leaching experiment was performed on the different samples. Varying particle size, gluconic acid concentration, and leaching times were used. A colorimetric assay was attempted

to determine nickel and iron concentrations of the leachate. Ultimately, the signals of the assay were not discernible, and the quantitative determination of nickel or iron was not possible. The pre-βME measurement was used to qualitatively describe differences in leaching performance. As particle size decreased, gluconic acid concentration increased, and leaching time was increased the relative leaching efficiencies of traditional samples increased. A comparison of tCO_2 and traditional comminution leaching performance was compared providing evidence the tCO_2 samples resulted in increased efficiencies. Ultimately, extent to which these efficiencies were different needs to be substantiated through an alternative analytical measurement.

RECOMMENDATIONS

The substitution of YE from KH_2PO_4 resulted in increased yields of REE from magnetic swarf, but did not have a significant impact on solubilization yields of base metals from LIB. The only measurable differences between biolixiviants produced under these varying microbial cultivation conditions were concentrations of citric, acetic, and succinic acid concentrations. Although the concentrations were low, their presence may have a profound impact on leaching efficiencies. To determine the significance of this impact, abiotic leaching studies should be performed to assess the contribution of citric, acetic, and succinic acid concentrations to overall metal solubilization yields. It is possible the presence and/or absence of keto-gluconic acids also contributes to increased metal solubilization. Development of a keto-gluconic acid quantification method would allow for a more complete analysis of differences between biolixiviants produced as a result of YE substitution. Additionally, alternative carbon sources should be investigated to reduce the overall operational costs associated with *G. oxydans* bioleaching. Glucose currently accounts for one of the greatest cost expenditures in the outlined bioleaching process. The use of an alternative carbon source, such as agricultural waste, would substantially decrease costs and overall improve the economic viability of electron waste recycling through bioleaching.

Preliminary results indicate further refinement of the awaruite ore is necessary. Literature suggests flotation may be a promising technology to achieve high degrees of ore concentration. Further concentration of the ore would provide for a more informative investigation into differences between comminution technologies. Imaging and image processing could be used to determine whether physical differences, including shape and size, exist between awaruite ore processed through the different comminution techniques. Additionally, these concentrated

samples could be used for future leaching and/or bioleaching experimentation to determine whether comminution ultimately impacts recovery yields.

Initial investigations indicate that leaching of awaruite ore, within the gluconic acid concentrations of 75 mM and 105 mM, is possible. Ultimately, the colorimetric assay hindered the quantification of these leaching yields. It is possible that gluconic acid resulted in the inhibition of assay signal. Both gluconic acid and βME are chelating agents, thus it is possible there is competition resulting in lessened signals. To discern whether this is the case, gluconic acid and nickel, as well as gluconic acid and iron standard curves should be developed. This would allow for the direct determination of how gluconic acid impacts assay signals. It would also be beneficial to investigate how the assay performs under combined varying concentration of nickel and iron. The standard curves were developed independently; therefore, it is impossible to discern how signal would be impacted by their joint presence. It would be most beneficial to perform these standard curves in conditions where both iron is in higher concentrations and when nickel is in higher concentrations.

Ultimately, once a method has been developed to quantify leaching yields, abiotic leaching studies should be performed on the concentrated awaruite ore to optimize this process. It would be beneficial to determine concentrations of the different acidic components that promote heightened metal solubilization. This could inform further microbial cultivation experiments to promote generation of these beneficial acids.

REFERENCES CITED

1. Nassar, N.T., E. Alonso, and J.L. Brainard, *Investigation of U.S. Foreign Reliance on Critical Minerals—U.S. Geological Survey technical input document in response to Executive Order No. 13953 Signed September 30, 2020*, in *Open-File Report*. 2020: Reston, VA. p. 37.

2. Bosecker, K., *Bioleaching: metal solubilization by microorganisms.* FEMS microbiology reviews, 1997. **20**(3): p. 591-604.

3. Alipanah, M., et al., *Sustainable bioleaching of lithium-ion batteries for critical materials recovery*. Journal of Cleaner Production, 2023. **382**: p. 135274.

4. Cruz-Rodríguez, I.A., N.G. Rojas-Avelizapa, and A.M. Rivas-Castillo, *Microbially-Produced Organic Acids as Leaching Agents for Metal Recovery Processes.* Postępy Mikrobiologii, 2022. **61**(4): p. 179-190.

5. Rasoulnia, P., R. Barthen, and A.-M. Lakaniemi, *A critical review of bioleaching of rare earth elements: The mechanisms and effect of process parameters.* Critical reviews in environmental science and technology, 2021. **51**(4): p. 378-427.

6. Bringer, S. and M. Bott, *Central Carbon Metabolism and Respiration in Gluconobacter oxydans*, in *Acetic Acid Bacteria: Ecology and Physiology*, K. Matsushita, et al., Editors. 2016, Springer Japan: Tokyo. p. 235-253.

7. Rasoulnia, P., et al., *Low residual dissolved phosphate in spent medium bioleaching enables rapid and enhanced solubilization of rare earth elements from end-of-life NiMH batteries.* Minerals engineering, 2022. **176**: p. 107361.

8. Abhilash, et al., *Extraction of REEs from Blast Furnace Slag by Gluconobacter oxydans.* Minerals (Basel), 2022. **12**(6): p. 701.

9. Reed, D.W., et al., *Bioleaching of rare earth elements from waste phosphors and cracking catalysts.* Hydrometallurgy, 2016. **166**: p. 34-40.

10. Hesse, M., et al., *Experimental demonstration of comminution with transcritical carbon dioxide cycles.* Powder technology, 2022. **407**: p. 117615.

11. Seiler, S., et al., *Awaruite, a new large nickel resource. Part 1: Physicochemical properties and their implication for mineral processing.* Minerals engineering, 2022. **186**.

12. Lipman, T.E. and P. Maier, *Advanced materials supply considerations for electric vehicle applications.* MRS bulletin, 2021. **46**(12): p. 1164-1175.

13. Charalampides, G., et al., *Rare Earth Elements: Industrial Applications and Economic Dependency of Europe.* Procedia economics and finance, 2015. **24**: p. 126-135.

14. Raju, R.D., *Critical minerals: their nature, occurrence, recovery and uses.* Current science (Bangalore), 2020. **119**(6): p. 919-925.

15. Kiehbadroudinezhad, M., A. Merabet, and H. Hosseinzadeh-Bandbafha, *Electronic Waste to Energy, Technologies, Economics, and Challenges: A Renewable or Non-Renewable Path?*, in *Reference Module in Earth Systems and Environmental Sciences*. 2023, Elsevier.

16. Laputka, M. and W. Xie, *A Review of Recent Advances in Pyrometallurgical Process Measurement and Modeling, and Their Applications to Process Improvement.* Mining, Metallurgy & Exploration, 2021. **38**(2): p. 1135-1165.

17. Naseri, T., et al., *A comprehensive review of bioleaching optimization by statistical approaches: recycling mechanisms, factors affecting, challenges, and sustainability.* RSC advances, 2023. **13**(34): p. 2357-23589.

18. Hocking, M.B., *13 - Ore Enrichment and Smelting of Copper*, in *Handbook of Chemical Technology and Pollution Control (Third Edition)*, M.B. Hocking, Editor. 2005, Academic Press: San Diego. p. 391-420.

19. Fleming, C.A., *Hydrometallurgy of precious metals recovery.* Hydrometallurgy, 1992. **30**(1-3): p. 127-162.

20. Free, M.L., *Hydrometallurgy: Fundamentals and Applications*. 2 ed. The Minerals, Metals & Materials Series. 2021, Cham: Springer International Publishing AG.

21. Faraji, F., et al., *27 - Recyclability and recycling technologies for lithium–sulfur batteries,* in *Lithium-Sulfur Batteries*, R.K. Gupta, et al., Editors. 2022, Elsevier. p. 627-651.

22. Alipanah, M., et al., *Value recovery from spent lithium-ion batteries: A review on technologies, environmental impacts, economics, and supply chain.* Clean Technologies and Recycling, 2021. **1**(2): p. 152-184.

23. Baniasadi, M., et al., *Advances in bioleaching as a sustainable method for metal recovery from e-waste: A review.* Journal of Industrial and Engineering Chemistry, 2019. **76**: p. 75-90.

24. Thompson, V.S., et al., *Techno-economic and Life Cycle Analysis for Bioleaching Rare-Earth Elements from Waste Materials.* ACS sustainable chemistry & engineering, 2018. **6**(2): p. 1602-1609.

25. Biswal, B.K. and R. Balasubramanian, *Recovery of valuable metals from spent lithium-ion batteries using microbial agents for bioleaching: a review.* Frontiers in microbiology, 2023. **14**: p. 1197081-1197081.

26. Krebs, W., et al., *Microbial recovery of metals from solids.* FEMS Microbiology Reviews, 1997. **20**(3-4): p. 605-617.

27. Rawlings, D.E., *Microbially-assisted dissolution of minerals and its use in the mining industry.* Pure and Applied Chemistry, 2004. **76**(4): p. 847-859.

28. Mishra, D., et al., *Bioleaching: A microbial process of metal recovery; A review.* Metals and Materials International, 2005. **11**(3): p. 249-256.

29. Ji, X., et al., *Bioleaching of Typical Electronic Waste-Printed Circuit Boards (WPCBs): A Short Review.* Int J Environ Res Public Health, 2022. **19**(12).

30. Ehrlich, H.L., *Microbes and metals.* Applied microbiology and biotechnology, 1997. **48**(6): p. 687-692.

31. Vera, M., et al., *Progress in bioleaching: fundamentals and mechanisms of microbial metal sulfide oxidation - part A.* Appl Microbiol Biotechnol, 2022. **106**(21): p. 6933-6952.

32. Jin, H., et al., *Sustainable Bioleaching of Rare Earth Elements from Industrial Waste Materials Using Agricultural Wastes.* ACS sustainable chemistry & engineering, 2019. **7**(18): p. 15311-15319.

33. Liermann, L.J., et al., *Microenvironments of pH in biofilms grown on dissolving silicate surfaces.* Chemical geology, 2000. **171**(1-2): p. 1-16.

34. Dusengemungu, L., et al., *Overview of fungal bioleaching of metals.* Environmental Advances, 2021. **5**: p. 100083.

35. Tzeferis, P.G., S. Agatzini, and E.T. Nerantzis, *Mineral leaching of non-sulphide nickel ores using heterotrophic micro-organisms.* Letters in Applied Microbiology, 1994. **18**(4): p. 209-213.

36. Upton, D.J., S.J. McQueen-Mason, and A.J. Wood, *An accurate description of Aspergillus niger organic acid batch fermentation through dynamic metabolic modelling.* Biotechnology for Biofuels, 2017. **10**(1): p. 258.

37. Bosecker, K. and Anonymous. *Chemical and microbial leaching of serpentinite from Potcoava*. Julich: Kernforschungsanlage (KFA) Juelich, Project Agency Materials Raw Materials Res.

38. Zhang, H., et al., *Heterotrophic Bioleaching of Vanadium from Low-Grade Stone Coal by Aerobic Microbial Consortium.* Int J Environ Res Public Health, 2022. **19**(20).

39. Castro, I.M., et al., *Bioleaching of zinc and nickel from silicates using Aspergillus niger cultures.* Hydrometallurgy, 2000. **57**(1): p. 39-49.

40. Muddanna, M.H. and S.S. Baral, *Leaching of nickel and vanadium from the spent fluid catalytic cracking catalyst by reconnoitering the potential of Aspergillus niger associating with chemical leaching.* Journal of Environmental Chemical Engineering, 2019. **7**(2): p. 103025.

41. Giese, E.C., et al., *Characterization and bioleaching of nickel laterite ore using Bacillus subtilis strain.* Biotechnology Progress, 2019. **35**(6): p. e2860.

42. Dopson, M., et al., *Growth in sulfidic mineral environments: metal resistance mechanisms in acidophilic micro-organisms.* Microbiology (Reading), 2003. **149**(Pt 8): p. 1959-1970.

43. Ano, Y., et al., *Selective, High Conversion of D-Glucose to 5-Keto-D-gluoconate by Gluconobacter suboxydans.* Bioscience, biotechnology, and biochemistry, 2011. **75**(3): p. 586-589.

44. Tchounwou, P.B., et al., *Heavy metal toxicity and the environment.* Exp Suppl, 2012. **101**: p. 133-64.

45. Jain, N. and D.K. Sharma, *Biohydrometallurgy for Nonsulfidic Minerals—A Review.* Geomicrobiology Journal, 2004. **21**(3): p. 135-144.

46. Valix, M. and L.O. Loon, *Adaptive tolerance behaviour of fungi in heavy metals.* Minerals Engineering, 2003. **16**(3): p. 193-198.

47. Lorenzen, L. and J.S.J. van Deventer, *The interrelationship between mineral liberation and leaching behaviour.* International Journal of Mineral Processing, 1994. **41**(1): p. 1-15.

48. Wang, X., et al., *Effect of particle size on uranium bioleaching in column reactors from a low-grade uranium ore.* Bioresource Technology, 2019. **281**: p. 66-71.

49. Johnson, D., *The Evolution, Current Status, and Future Prospects of Using Biotechnologies in the Mineral Extraction and Metal Recovery Sectors.* Minerals (Basel), 2018. **8**(8): p. 343.

50. Schmitz, A.M., et al., *Generation of a Gluconobacter oxydans knockout collection for improved extraction of rare earth elements.* Nature Communications, 2021. **12**(1): p. 6693.

51. Prust, C., et al., *Complete genome sequence of the acetic acid bacterium Gluconobacter oxydans.* Nature Biotechnology, 2005. **23**(2): p. 195-200.

52. Gupta, A., et al., *Gluconobacter oxydans: its biotechnological applications.* Journal of molecular microbiology and biotechnology, 2001. **3**(3): p. 445-456.

53. Antonick, P.J., et al., *Bio- and mineral acid leaching of rare earth elements from synthetic phosphogypsum.* The Journal of Chemical Thermodynamics, 2019. **132**: p. 491-496.

54. Bunaciu, A.A., E.g. Udriştioiu, and H.Y. Aboul-Enein, *X-Ray Diffraction: Instrumentation and Applications.* Critical reviews in analytical chemistry, 2015. **45**(4): p. 289-299.

55. Xiao, J., Y. Song, and Y. Li, *Comparison of Quantitative X-ray Diffraction Mineral Analysis Methods.* Minerals (Basel), 2023. **13**(4): p. 566.

56. Tonžetić, I.Ž., *5 - Quantitative analysis of iron ore using SEM-based technologies*. 2015, Elsevier Ltd. p. 161-189.

57. López, C., et al., *Electrochemical Selective Leaching and Deposition of Ag, Au and Pt from electronic waste.* International Journal of Electrochemical Science, 2017. **12**: p. 8198-8216.

58. Mennickent, D., et al., *Analytical performance of Compton/Rayleigh signal ratio by total reflection X-ray fluorescence (TXRF): A potential methodological tool for sample differentiation.* X-ray spectrometry, 2022. **51**(2): p. 142-150.

59. Regadío, M., et al., *Direct Analysis of Metal Ions in Solutions with High Salt Concentrations by Total Reflection X-ray Fluorescence.* Analytical chemistry (Washington), 2017. **89**(8): p. 4595-4603.

60. Chen, L., J. Xu, and J. Chen, *Applications of scanning electron microscopy in earth sciences.* Science China. Earth sciences, 2015. **58**(10): p. 1768-1778.

61. Schwartz, A.J., et al., *EBSD in the Earth Sciences: Applications, Common Practice, and Challenges*. 2009, Springer: United States. p. 345-360.

62. Ammann, A.A., *Inductively coupled plasma mass spectrometry (ICP MS): a versatile tool.* Journal of mass spectrometry., 2007. **42**(4): p. 419-427.

63. Zoorob, G.K., J.W. McKiernan, and J.A. Caruso, *ICP-MS for elemental speciation studies.* Mikrochimica acta (1966), 1998. **128**(3-4): p. 145-168.

64. Liu, Y., et al., *Applications of LA-ICP-MS in the elemental analyses of geological samples.* Chinese science bulletin, 2013. **58**(32): p. 3863-3878.

65. Beaty, R.D. and J.D. Kerber, *Concepts, instrumentation and techniques in atomic absorption spectrophotometry*. 1978: Perkin-Elmer USA.

66. Potts, P.J., *Atomic absorption spectrometry*, in *A Handbook of Silicate Rock Analysis*, P.J. Potts, Editor. 1987, Springer Netherlands: Dordrecht. p. 106-152.

67. Dzurendová, S., et al., *The influence of phosphorus source and the nature of nitrogen substrate on the biomass production and lipid accumulation in oleaginous Mucoromycota fungi.* Applied Microbiology and Biotechnology, 2020. **104**.

68. *D6913 Standard Test Methods for Particle-Size Distribution (Gradation) of Soils Using Sieve Analysis*. 2004.

69. Biswal, B.K., et al., *Biological Leaching and Chemical Precipitation Methods for Recovery of Co and Li from Spent Lithium-Ion Batteries.* ACS Sustainable Chemistry & Engineering, 2018. **6**(9): p. 12343-12352.

70. Horeh, N.B., S.M. Mousavi, and S.A. Shojaosadati, *Bioleaching of valuable metals from spent lithium-ion mobile phone batteries using Aspergillus niger.* Journal of Power Sources, 2016. **320**: p. 257-266.

71. Lobos, A., et al., *Tolerance of three fungal species to lithium and cobalt: Implications for bioleaching of spent rechargeable Li-ion batteries.* J Appl Microbiol, 2021. **131**(2): p. 743-755.

72. Xin, Y., et al., *Bioleaching of valuable metals Li, Co, Ni and Mn from spent electric vehicle Li-ion batteries for the purpose of recovery.* Journal of cleaner production, 2016. **116**: p. 249-258.

73. Mishra, D., et al., *Bioleaching of metals from spent lithium ion secondary batteries using Acidithiobacillus ferrooxidans.* Waste management (Elmsford), 2008. **28**(2): p. 333-338.

74. Jegan Roy, J., M. Srinivasan, and B. Cao, *Bioleaching as an Eco-Friendly Approach for Metal Recovery from Spent NMC-Based Lithium-Ion Batteries at a High Pulp Density.* ACS sustainable chemistry & engineering, 2021. **9**(8): p. 3060-3069.

75. Habibzadeh, A., M.A. Kucuker, and M. Gökelma, *Review on the Parameters of Recycling NdFeB Magnets via a Hydrogenation Process.* ACS Omega, 2023. **8**(20): p. 17431-17445.

76. Chowdhury, N.A., et al., *Sustainable Recycling of Rare-Earth Elements from NdFeB Magnet Swarf: Techno-Economic and Environmental Perspectives.* ACS Sustainable Chemistry & Engineering, 2021. **9**(47): p. 15915-15924.

77. Glombitza, F. and S. Reichel, *Metal-containing residues from industry and in the environment: geobiotechnological urban mining.* Advances in biochemical engineering/biotechnology, 2014. **141**: p. 49-107.

78. Tomé, D., *Yeast Extracts: Nutritional and Flavoring Food Ingredients.* ACS Food Science & Technology, 2021. **1**(4): p. 487-494.

79. Popovic, M., et al., *Elemental composition, heat capacity from 2 to 300 K and derived thermodynamic functions of 5 microorganism species.* Journal of Biotechnology, 2021. **331**: p. 99-107.

80. Thompson, K.A., R.S. Summers, and S.M. Cook, *Development and experimental validation of the composition and treatability of a new synthetic bathroom greywater (SynGrey).* Environmental science water research & technology, 2017. **3**(6): p. 1120-1131.

81. Boer, V.M., et al., *Growth-limiting intracellular metabolites in yeast growing under diverse nutrient limitations.* Molecular biology of the cell, 2010. **21**(1): p. 198-211.

82. Tschoep, H., et al., *Adjustment of growth and central metabolism to a mild but sustained nitrogen-limitation in Arabidopsis.* Plant, cell and environment, 2009. **32**(3): p. 300-318.

83. Hölscher, T., et al., *Glucose Oxidation and PQQ-Dependent Dehydrogenases in Gluconobacter oxydans.* Journal of molecular microbiology and biotechnology, 2009. **16**(1-2): p. 6-13.

84. Harder, W. and L. Dijkhuizen, *Physiological responses to nutrient limitation.* Annu Rev Microbiol, 1983. **37**: p. 1-23.

85. Kalinowski, B.E., et al., *Rates of bacteria-promoted solubilization of Fe from minerals: a review of problems and approaches.* Chemical Geology, 2000. **169**(3): p. 357-370.

86. Beschkov, V., S. Velizarov, and L. Peeva, *Some kinetic aspects and modelling of biotransformation of D-glucose to keto-D-gluconates.* Bioprocess Engineering, 1995. **13**(6): p. 301-305.

87. Huang, K., et al., *A Precise Method for Processing Data to Determine the Dissociation Constants of Polyhydroxy Carboxylic Acids via Potentiometric Titration.* Applied biochemistry and biotechnology, 2017. **183**(4): p. 1426-1438.

88. Kirimura, K., Y. Honda, and T. Hattori, *3.14 - Gluconic and Itaconic Acids*, in *Comprehensive Biotechnology (Second Edition)*, M. Moo-Young, Editor. 2011, Academic Press: Burlington. p. 143-147.

89. Lide, D.R., *CRC Handbook of Chemistry and Physics, 84th Edition*, in *Journal of the American Chemical Society*. 2004, American Chemical Society. p. 1586-1586.

90. Comuzzo, P. and F. Battistutta, *Chapter 2 - Acidification and pH Control in Red Wines*. 2019, Elsevier Inc. p. 17-34.

91. Goldberg, I. and J.S. Rokem, *Organic and Fatty Acid Production, Microbial*. 2009. p. 421-442.

92. Ahmed, B.M., et al., *Costly effective bioleaching of valuable metals from low grade ore using Aspergillus nidulans.* International journal of environmental science and technology (Tehran), 2024. **21**(6): p. 5469-5482.

93. Folsom, J.P., A.E. Parker, and R.P. Carlson, *Physiological and proteomic analysis of Escherichia coli iron-limited chemostat growth.* J Bacteriol, 2014. **196**(15): p. 2748-61.

94. Rasoulnia, P., et al., *Leaching of rare earth elements and base metals from spent NiMH batteries using gluconate and its potential bio-oxidation products.* Journal of Hazardous Materials, 2021. **414**: p. 125564.

95. Whitworth, A.J., et al., *Review on advances in mineral processing technologies suitable for critical metal recovery from mining and processing wastes.* Cleaner Engineering and Technology, 2022. **7**: p. 100451.

96. Wills, B.A. and J.A. Finch, *Wills' mineral processing technology : an introduction to the practical aspects of ore treatment and mineral recovery*. Eighth edition. ed. 2016, Amsterdam, [Netherlands: Butterworth-Heinemann.

97. Vidal, O., B. Goffé, and N. Arndt, *Metals for a low-carbon society.* Nature Geoscience, 2013. **6**(11): p. 894-896.

98. Zhang, Z.-X., *Rock fracture and blasting: theory and applications*. 2016: Butterworth-Heinemann.

99. *Review of methods of improving mineral liberation.*

100. Corey, A.T., et al., *Influence of shape on the fall velocity of sand grains.* 1949.

101. Chen, L. and D. Xiong, *Chapter Seven - Magnetic Techniques for Mineral Processing*. 2015, Elsevier Ltd. p. 287-324.

102. Oberteuffer, J., *Magnetic separation: A review of principles, devices, and applications.* IEEE transactions on magnetics, 1974. **10**(2): p. 223-238.

103. Peleka, E.N., G.P. Gallios, and K.A. Matis, *A perspective on flotation: a review.* Journal of Chemical Technology & Biotechnology, 2018. **93**(3): p. 615-623.

104. Grandillo, A., et al., *NI 43-101 Technical Report Preliminary Economic Assessment Baptiste Nickel Project British.* 2020.

105. *Chapter 4 - Thermal Properties of Pure Substances and Some Applications*, in *Practical Chemical Thermodynamics for Geoscientists*, B. Fegley, Editor. 2013, Academic Press: Boston. p. 81-125.

106. Seiler, S., et al., *Awaruite, a new large nickel resource. Part 2: Assessment of magnetic separation.* Minerals Engineering, 2023. **191**.

107. Seiler, S., et al., *Awaruite, a New Large Nickel Resource: Flotation under Weakly Acidic Conditions.* Minerals (Basel), 2023. **13**(9): p. 1147.

108. Iveson, S.M., D.M. Hunter, and K.P. Galvin, *A water-based method for measuring density-based partition curves of separators used in coal and mineral processing.* Minerals Engineering, 2015. **79**: p. 196-211.

109. Prior, D.J., et al., *The application of electron backscatter diffraction and orientation contrast imaging in the SEM to textural problems in rocks.* The American mineralogist, 1999. **84**(11-12): p. 1741-1759.

110. van de Moortèle, B., et al., *Electron back-scattering diffraction (EBSD) measurements of antigorite lattice-preferred orientations (LPO).* J Microsc, 2010. **239**(3): p. 245-8.

111. Kouketsu, Y., et al., *Drastic effect of shearing on graphite microtexture: attention and application to Earth science.* Progress in Earth and Planetary Science, 2019. **6**.

112. Umare, M. and S. Ambadkar. *Estimation of shape factor for irregular particles using three-axial measurement approach*. in *IOP Conference Series: Earth and Environmental Science*. 2022. IOP.

113. Hogg, R., M.L. Turek, and E. Kaya, *The Role of Particle Shape in Size Analysis and the Evaluation of Comminution Processes.* Particulate Science and Technology, 2004. **22**(4): p. 355-366.

114. Pourghahramani, P. and E. Forssberg, *REVIEW OF APPLIED PARTICLE SHAPE DESCRIPTORS AND PRODUCED PARTICLE SHAPES IN GRINDING ENVIRONMENTS. PART II: THE INFLUENCE OF COMMINUTION ON THE PARTICLE SHAPE.* Mineral processing and extractive metallurgy review, 2005. **26**(2): p. 167-186.

115. Olafsdottir, A.H. and H.U. Sverdrup, *Modelling Global Nickel Mining, Supply, Recycling, Stocks-in-Use and Price Under Different Resources and Demand Assumptions for 1850–2200.* Mining, Metallurgy & Exploration, 2021. **38**(2): p. 819-840.

116. Carpen, H.L. and E.C. Giese, *Enhancement of nickel laterite ore bioleaching by Burkholderia sp. using a factorial design.* Applied Water Science, 2022. **12**(8): p. 181.

117. Petrus, H.B.T.M., et al., *Effect of pulp density and particle size on indirect bioleaching of Pomalaa nickel laterite using metabolic citric acid.* IOP conference series. Materials Science and Engineering, 2018. **285**(1): p. 12004.

118. Johnson, D.B., S.L. Smith, and A.L. Santos, *Bioleaching of Transition Metals From Limonitic Laterite Deposits and Reassessment of the Multiple Roles of Sulfur-Oxidizing Acidophiles in the Process.* Frontiers in Microbiology, 2021. **12**.

119. García-Balboa, C., et al., *Microbial biominers: Sequential bioleaching and biouptake of metals from electronic scraps.* Microbiologyopen, 2022. **11**(1): p. e1265.

120. Zamora, L.L., et al., *Quantitative colorimetric-imaging analysis of nickel in iron meteorites.* Talanta (Oxford), 2011. **83**(5): p. 1575-1579.

121. Almaquer, F.E.P., J.S.Y. Ricacho, and R.L.G. Ronquillo, *Simple and rapid colorimetric sensing of Ni(II) ions in tap water based on aggregation of citrate-stabilized silver nanoparticles.* Sustainable environment research, 2019. **29**(1): p. 1-10.

122. Min, Z., Y.-Q. Liu, and B.-C. Ye, *Colorimetric assay for parallel detection of Cd2+, Ni2+ and Co2+ using peptide-modified gold nanoparticles.* Analyst (London), 2012. **137**(3): p. 601-607.

123. Benini, S., et al., *The complex of Bacillus pasteurii urease with β-mercaptoethanol from X-ray data at 1.65-Å resolution.* Journal of biological inorganic chemistry, 1998. **3**(3): p. 268-273.

124. Musiani, F., et al., *Structure-based computational study of the catalytic and inhibition mechanisms of urease.* Journal of biological inorganic chemistry, 2001. **6**(3): p. 300-314.

APPENDICES

APPENDIX A

RECYCLING OF LIB AND MAGNETIC SWARF

SUPPLEMENTARY DATA

Table 1A-3A contains a summary of the metabolites produced by *Gluconobacter oxydans* over the course of the cultivation period. 1 mL of supernatant was harvested at each time point and analyzed through HPLC analysis to determine the concentration of organic acid produced. The acid concentrations for Pkm, mPkm1, and mPkm3 are demonstrated in Table 1A, Table 2A, and Table 3A, respectively. A full summary of all elements solubilized through the leaching of LIB waste is demonstrated in Figure A.1.

Table 1A. Summary of *G. oxydans* metabolite production under Pkm growth media conditions. Acid concentrations measured via HPLC analysis.

Time (hr)	Citric Acid (mM)	Gluconic Acid (mM)	Succinic Acid (mM)	Acetic Acid (mM)
0	0	0	0.3278 ± 0.0019	0
15	0	0.6986 ± 0.0626	0.3262 ± 0.0064	0
24	0	27.15 ± 2.625	0.1209 ± 0.0856	0
40	0.2397 ± 0.0341	150.9 ± 3.844	0	6.851 ± 0.1595
48	0	192.8 ± 1.708	0	3.659 ± 0.2092
63	0.2882 ± 0.0441	200.8 ± 2.511	0	7.333 ± 0.0376
72	0	229.7 ± 3.063	0	3.781 ± 0.0586

Table 2A. Summary of *G. oxydans* metabolite production under mPkm1 media conditions. Acid concentration measured via HPLC analysis.

Time (hr)	Citric Acid (mM)	Gluconic Acid (mM)	Succinic Acid (mM)	Acetic Acid (mM)
0	0	0	0.5694 ± 0.0029	0
15	0	0.6682 ± 0.0119	0.5732 ± 0.0055	0
24	0	20.89 ± 2.345	0.5152 ± 0.0608	0
40	1.082 ± 0.1996	147.2 ± 17.34	1.433 ± 0.1196	8.853 ± 0.6344
48	0.6324 ± 0.0253	186.8 ± 2.488	0.6796 ± 0.0130	5.975 ± 0.0214
63	1.788 ± 0.1895	159.6 ± 12.26	2.625 ± 0.2382	9.809 ± 0.4596
72	1.294 ± 0.2910	179.1 ± 2.774	0.6508 ± 0.0406	7.609 ± 0.1230

Table 3A. Summary of *G. oxydans* metabolite production under mPkm3 media conditions. Acid concentration measured via HPLC analysis.

Time (hr)	Citric Acid (mM)	Gluconic Acid (mM)	Succinic Acid (mM)	Acetic Acid (mM)
0	0	0	0.5043 ± 0.0046	0
15	0	0.6796 ± 0.0394	0.5034 ± 0.0025	0
24	0	19.30 ± 6.975	0.4028 ± 0.0304	0
40	0.5757 ± 0.0931	140.9 ± 11.55	1.099 ± 0.0062	7.613 ± 0.2560
48	0.0125 ± 0.0177	216.4 ± 7.725	0.5626 ± 0.0336	4.937 ± 0.3134
63	1.717 ± 0.2016	220.1 ± 9.508	1.875 ± 0.0332	9.411 ± 0.4750
72	0.8691 ± 0.0144	231.6 ± 12.33	0.5105 ± 0.0295	6.139 ± 0.2933

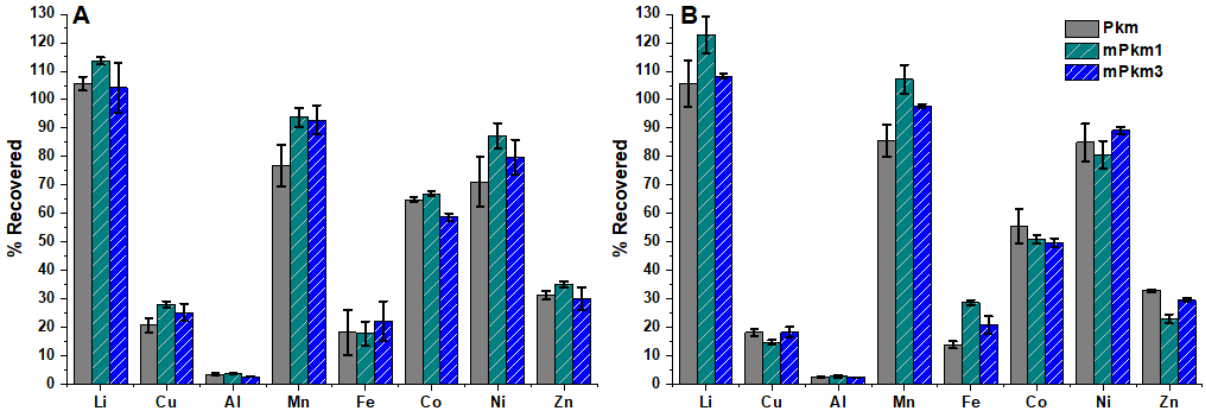

Figure A.1 Leaching efficiencies for all elements of LIB black mass from the biolixiviant produced after (A) 48 hours and (B) 72 hours of *G. oxydans* cultivation.

APPENDIX B

SCANNING ELECTRON MICROSCOPY SUPPLEMENTARY

Powder samples were mounted to the sample chuck with carbon sticky tape. A layer of ~20 nm of carbon was coated on the samples to minimize sample charging during SEM analysis. Liberation and relative nickel concentrations were compared across the magnetic concentrates. The analysis focused on particles sized between 90-125 µm and 425-500 µm of both tCO_2 (Product 3) and traditional (Product 4) magnetic concentrate samples. Notably, Product 4 was not refined into distinct grain size fractions; therefore, the smaller grain size range analyzed consisted of particles between 75-125 µm. The BSE and corresponding EDS images are displayed in Figure A.2.

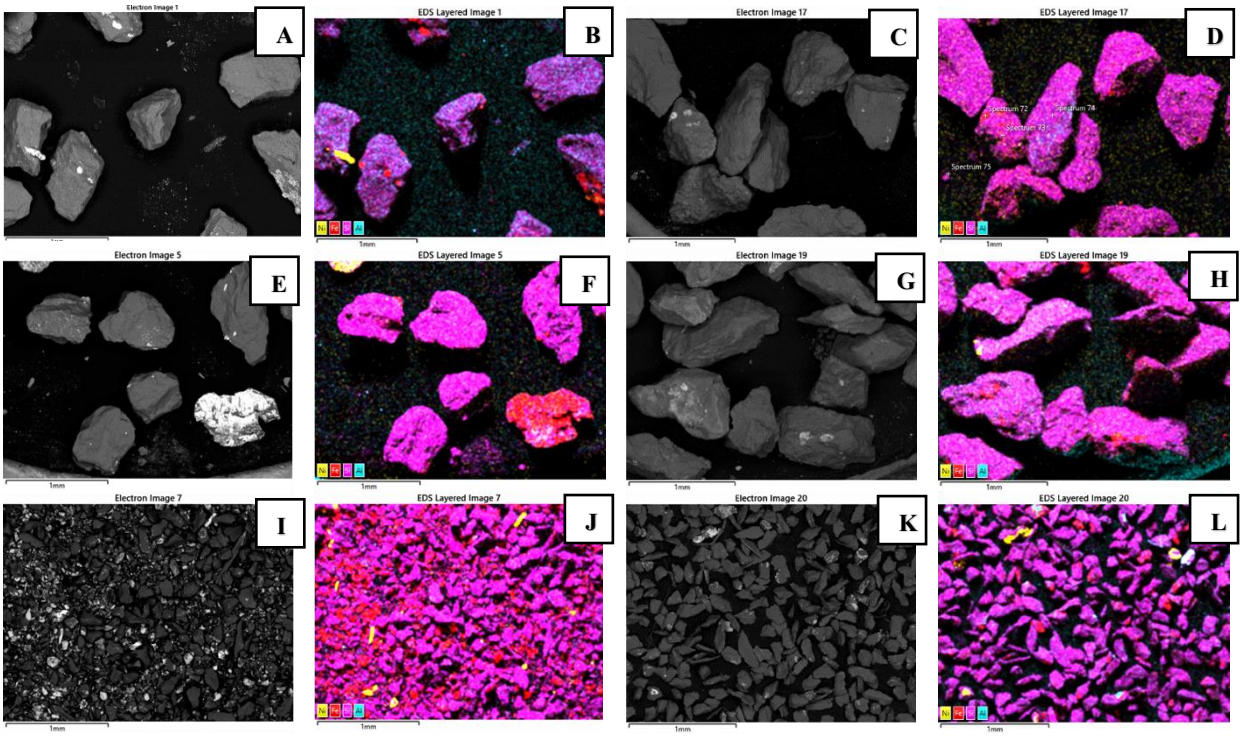

Figure A.2 Backscatter electron images with corresponding EDS map. Samples were mounted onto sample mounts and coated in ~20 nm of carbon. A and E depict BSE images of 425-500 µm tCO_2 particles with the corresponding EDS map in B and F. C and G depict BSE images of 425-500 µm traditional particles with the corresponding EDS map in D and H. I depicts 90-125 µm tCO_2 particles with the corresponding EDS map in J. K depicts 75-125 µm traditional particles with the corresponding EDS map in L. EDS images denote nickel in yellow, iron in red, silicon in pink, and aluminum in teal.

EDS spectra of the full site, represented in Figure 16 and Figure A.2, were collected. The fine particle, 75-125 μm for traditional and 90-125 μm for tCO_2 samples, elemental distributions are represented in Table 4A. The coarse particle, 425-500 μm, elemental distributions are represented in Table 5A.

Table 4A. Summary of full image EDS spectra of the fine particles imaged.

	tCO_2 90-125 μm				Magnetic Concentrate 75-125 μm			
	Site 1	Site 2	Site 3	Avg	Site 1	Site 2	Site 3	Avg
Element	wt%	wt%	wt%	wt%	wt%	wt%	wt%	wt%
O	45.39	44.84	44.47	44.90	50.82	50.27	49.99	50.36
Mg	22.15	21.9	21.83	21.96	23.22	23.35	22.17	22.91
Si	15.03	14.83	14.67	14.84	16.7	16.56	16.17	16.48
Fe	14.81	15.68	16.33	15.61	6.1	7.11	5.75	6.32
S	0.11	0.13	0.12	0.12	0.29	0.27	0.25	0.27
Na	0.06	0.1	0.07	0.08	0.23	0.27	0.19	0.23
Al	0.68	0.67	0.78	0.71	0.69	0.65	3.8	1.71
Ni	0.58	0.62	0.46	0.55	0.49	0.41	0.2	0.37
Ca	0.26	0.29	0.32	0.29	0.51	0.3	0.53	0.45
K	0.02	0.06	0.03	0.04	0.03	0.03	0.01	0.02
Cr	0.5	0.53	0.56	0.53	0.3	0.26	0.21	0.26
Cu	0	0	0	0.00	0.03	0.04	0.05	0.04
Co	0	0	0	0.00	0.09	0.04	0.03	0.05
Ti	0.02	0.01	0.03	0.02	0.02	0	0	0.01
Ag	0	0	0	0.00	0.14	0	0.24	0.13
Zn	0	0	0	0.00	0	0.01	0	0.00
Sr	0.18	0.2	0.21	0.20	0.26	0.31	0.21	0.26
Mn	0.13	0.15	0.11	0.13	0.08	0.13	0.1	0.10
In	0.07	0	0	0.02	0	0	0.1	0.03

Table 5A. Summary of full image EDS spectra of the coarse particles imaged.

	tCO_2 425-500 μm					Magnetic Concentrate 425-500 μm				
	Site 1	Site 2	Site 3	Site 4	Avg	Site 1	Site 2	Site 3	Site 4	Avg
Element	wt%	wt%	wt%	wt%	wt%	wt%	wt%	wt%	wt%	wt%
O	53.07	47.58	53.39	45.53	49.89	52.69	53.53	53.73	53.53	53.37
Mg	21.81	20.84	20.02	20.85	20.88	22.71	23.22	22.62	23.19	22.94
Si	15.69	13.19	13.58	14.28	14.19	15.66	16.76	17.06	16.8	16.57
Fe	4.47	6.59	6.95	15.04	8.26	5.94	3.37	3.21	4.05	4.14
S	1.35	1.33	1.58	0.89	1.29	0.79	0.63	0.56	0.28	0.57
Na	1.22	1.25	1.69	0.99	1.29	0.67	0.52	0.5	0.25	0.49
Al	0.65	0.61	0.58	0.66	0.63	0.47	0.89	0.69	0.73	0.70
Ni	0.62	7.25	0.46	0.31	2.16	0.15	0	0.15	0.13	0.11
Ca	0.55	0.37	0.7	0.5	0.53	0.26	0.24	0.89	0.56	0.49
K	0.24	0.23	0.7	0.49	0.42	0.02	0.15	0.06	0.04	0.07
Cr	0.15	0.33	0.16	0.00	0.16	0.19	0.16	0.18	0.14	0.17
Cu	0.11	0.08	0.10	0.06	0.09	0.00	0.00	0.00	0.00	0.00
Co	0.06	0.20	0.07	0.13	0.12	0.00	0.00	0.00	0.02	0.01
Ti	0.01	0.00	0.02	0.03	0.02	0.00	0.01	0.01	0.00	0.01
Ag	0.00	0.16	0.00	0.00	0.04	0.00	0.18	0.00	0.00	0.05
Zn	0.00	0.00	0.00	0.25	0.06	0.00	0.00	0.00	0.00	0.00
Sr	0.00	0.00	0.00	0.00	0.00	0.34	0.26	0.26	0.21	0.27
Mn	0.00	0.00	0.00	0.00	0.00	0.10	0.08	0.10	0.08	0.09

To quantify differences in high value product concentration across comminution methods and particle size, ImageJ was used to determine relative content with respect to total particle area (Table 6A).

Table 6A. Summary of imageJ relative bright spot area. Images were thresholded in ImageJ to capture the bright, high value product. The area was measured. The image was re-thresholded to capture the entire particles and the area was again measured. This allowed for the % bright spot to be measured relative to the total particle area in the field of view.

		total area (μm^2)	particle % area	bright area (μm^2)	bright spot % area	Relative %
425-500 µm	tCO_2 site 1	1923310.76	30.641	69805.611	1.112	3.62945044
	tCO_2 site 2	1856619.23	30.716	273594.668	4.526	14.7361755
	tCO_2 site 3	1195082.86	20.497	106136.155	1.82	8.88107083
	tCO_2 site 4	1891386.27	31.088	265479.939	4.364	14.0362623
	trad site 1	1996373.87	35.638	168509.636	3.008	6.4475841
	trad site 2	2432589.81	43.435	41466.27	0.74	1.70461414
	trad site 3	2581555.37	46.253	15048.76	0.27	0.58293385
	trad site 4	3306101.83	59.528	62163.66	1.119	1.88027058
90-125 µm	tCO_2 site 1	2613531.41	43.643	565165.027	9.4374	21.6245737
	tCO_2 site 2	3244698.81	53.331	620144.492	10.193	19.1125441
	tCO_2 site 3	3870264.81	59.823	641251.561	9.913	16.568674
	trad site 1	2989331	54.701	92752.788	1.697	3.10279417
	trad site 2	3185800	56.511	190900	3.386	5.99221546
	trad site 3	3267295.57	57.18	140802.252	2.464	4.30944336

Secondary electron images were used to investigate whether topographical differences exist between comminution methods (Figure A.). The images presented herein represent 90-125 µm and 450-500 µm particles for the various products. This investigation was inconclusive as there is not a distinguishable difference between particles, although it is unclear what particle features would exist given due to different fracture methods.

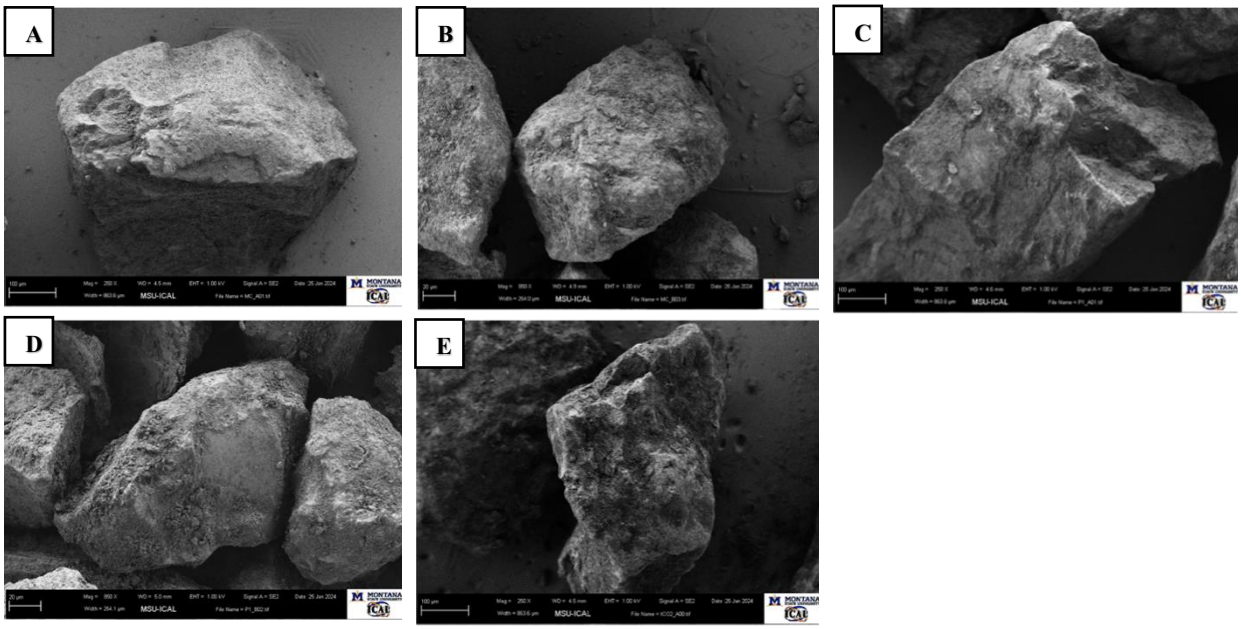

Figure A.3 Secondary electron images for the magnetic concentrate of A) Product 4 particle between 425-500 µm, B) Product 4 particle between 75-125 µm, C) Product 1 particle between 425-500 µm, D) Product 1 particle between 90-125 µm, and E) tCO2 (Product 3) particle between 425-500 µm.

APPENDIX C

IMAGEJ SHAPE FACTOR ANALYSIS

ImageJ, an image analysis software, was used to perform a shape factor analysis on the particles generated through the different rock fracture methods, tCO_2 and traditional crushing/grinding. As described in the Image Processing section of the Methods, the images were thresholded and segmented to differentiate between particles. Figure A.4.A and A.4.C demonstrates examples of raw BSE images that were uploaded into ImageJ. Figure A.4.B and Figure A.4.D provide examples of the output following thresholding and particle segmentation.

The particles were then measured in ImageJ to determine area, circularity, roundness, solidity, and aspect ratio. The data was then loaded into Origin to develop histograms as well as histogram statistics to determine whether physical differences are present between particles generated through the varying comminution methods. Table 7A represents the histogram statistics of the coarse particles and Table 8A representants the histogram statistics of the finer particles.

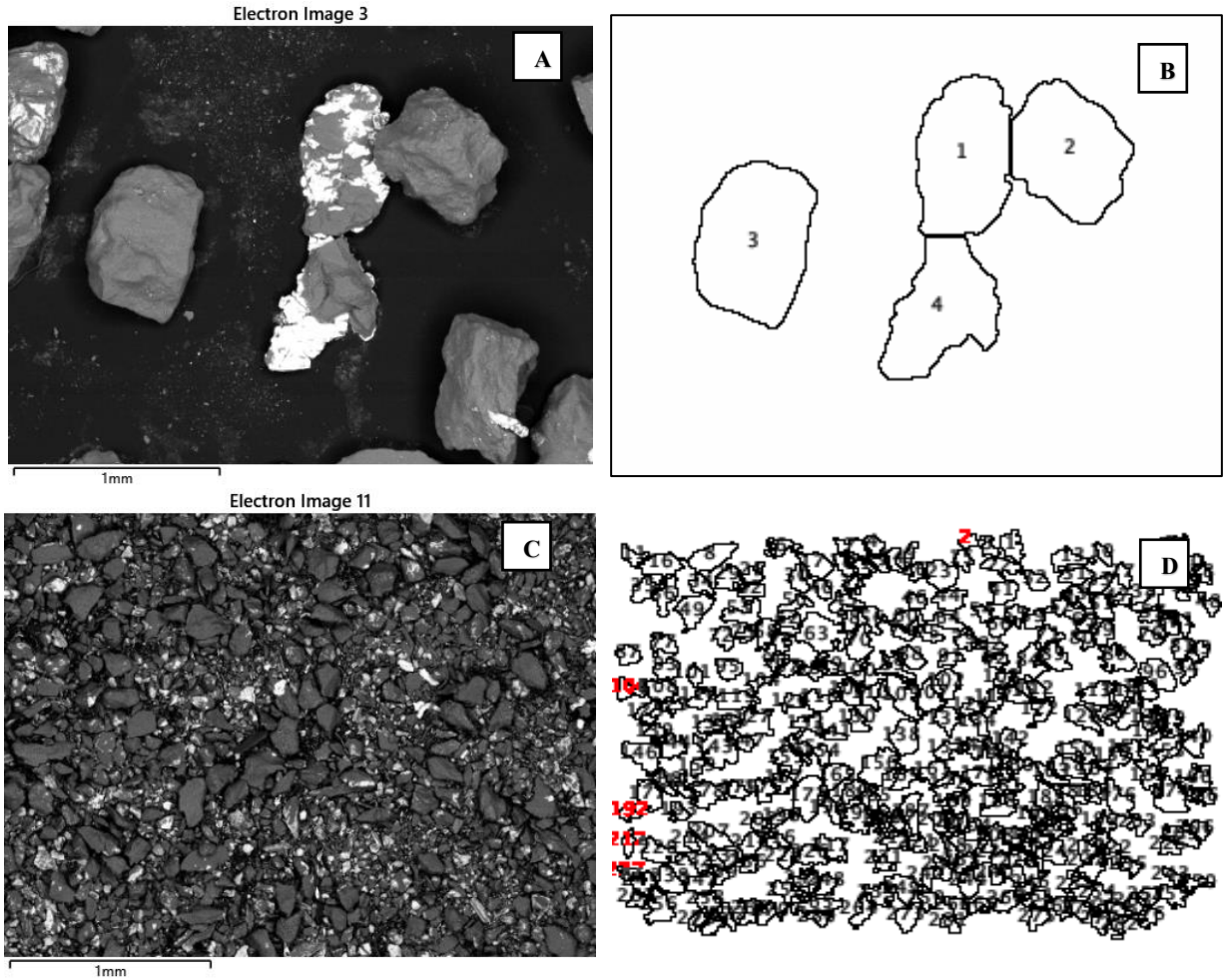

Figure A.4 Example of image processing through ImageJ. A) representation of the raw image for a large particle (425-500 μm) and B) the output of ImageJ following thresholding, segmentation, and measurement. Example of a small particle ImageJ analysis where A) is a representation of the raw image and b) the output of ImageJ following thresholding, segmentation and measurement. In this example, particles that were below the limit of particle size, indicating improper segmentation, were removed.

Table 7A. Coarse particle (425-500 μm) histogram statistics generated in Origin.

Parameter	Area (μm^2)		Aspect Ratio		Circularity		Roundness		Solidity	
Comminution Method	Traditional	tCO_2	Traditional	tCO_2	Traditional	tCO_2	Traditional	tCO_2	Traditional	tCO_2
N total	45	22	45	22	45	22	45	22	45	22
Mean	258593.48	269474.72	1.70	1.54	0.65	0.70	0.63	0.69	0.92	0.93
Standard Deviation	90186.28	63754.99	0.46	0.54	0.12	0.08	0.15	0.14	0.04	0.03
SE of mean	13444.18	13592.61	0.07	0.11	0.02	0.02	0.02	0.03	0.01	0.01
Variance	8.134E9	4.065E10	0.21	0.29	0.02	0.01	0.02	0.02	0.00	0.00
Skewness	0.03	1.09	1.23	3.37	-1.30	-1.09	0.00	-1.40	-1.10	-1.74
Kurtosis	-0.55	0.87	1.68	13.19	1.54	1.56	-0.50	2.60	0.12	3.81
Mode	--	--	1.20	1.40	0.75	--	0.60	0.72	0.95	0.91
Minimum	70779.73	187728.82	1.10	1.13	0.27	0.47	0.31	0.27	0.83	0.85
1st Quartile (Q1)	197945.85	221662.19	1.39	1.28	0.61	0.66	0.53	0.63	0.91	0.91
Median	234903.91	253580.25	1.61	1.37	0.68	0.72	0.62	0.73	0.93	0.93
3rd Quartile (Q3)	321590.04	302060.58	1.89	1.59	0.74	0.76	0.72	0.78	0.95	0.94
Maximum	433550.00	433366.45	3.19	3.70	0.82	0.81	0.91	0.89	0.97	0.96
Interquartile Range (Q3 - Q1)	123644.20	80398.39	0.50	0.31	0.12	0.10	0.19	0.15	0.04	0.03
Range	362770.27	245637.63	2.09	2.57	0.55	0.35	0.60	0.62	0.14	0.11

Table 8A. Small particle (75-125 μm) histogram statistics generated in Origin.

Parameter	Area (μm^2)		Aspect Ratio		Circularity		Roundness		Solidity	
Comminution Method	Traditional	tCO_2	Traditional	tCO_2	Traditional	tCO_2	Traditional	tCO_2	Traditional	tCO_2
N total	1827	2147	1827	2147	1827	2147	1827	2147	1827	2147
Mean	9921.63	6109.19	1.83	1.76	0.71	0.62	0.60	0.61	0.85	0.80
Standard Deviation	5531.35	4911.73	0.66	0.59	0.13	0.16	0.17	0.16	0.06	0.08
SE of mean	129.41	106.00	0.02	0.01	0.00	0.00	0.00	0.00	0.00	0.00
Variance	30595900.00	24125000.00	0.43	0.35	0.02	0.02	0.03	0.02	0.00	0.01
Skewness	0.81	1.76	1.84	2.91	-0.39	-0.18	-0.06	-0.09	-1.41	-0.71
Kurtosis	1.03	4.35	4.64	19.20	-0.12	-0.50	-0.60	-0.48	3.70	0.34
Mode	15207.85	1532.35	1.30	1.28	1.00	0.73	0.55	0.67	0.86	0.80
Minimum	573.88	189.37	1.02	1.01	0.28	0.14	0.19	0.11	0.52	0.42
1st Quartile (Q1)	5757.39	2469.45	1.37	1.38	0.62	0.51	0.48	0.50	0.82	0.75
Median	9310.69	4703.12	1.66	1.62	0.72	0.63	0.60	0.62	0.86	0.81
3rd Quartile (Q3)	13390.56	8204.14	2.08	2.00	0.81	0.74	0.73	0.73	0.89	0.86
Maximum	38793.73	40651.35	5.34	9.02	1.00	1.00	0.98	0.99	1.00	1.00
Interquartile Range (Q3 - Q1)	7633.17	5734.69	0.71	0.62	0.19	0.23	0.25	0.23	0.07	0.12
Range	38219.85	40461.98	4.32	8.01	0.72	0.86	0.79	0.88	0.49	0.58

APPENDIX D

COLORIMETRIC ASSAY SUPPLEMENTARY

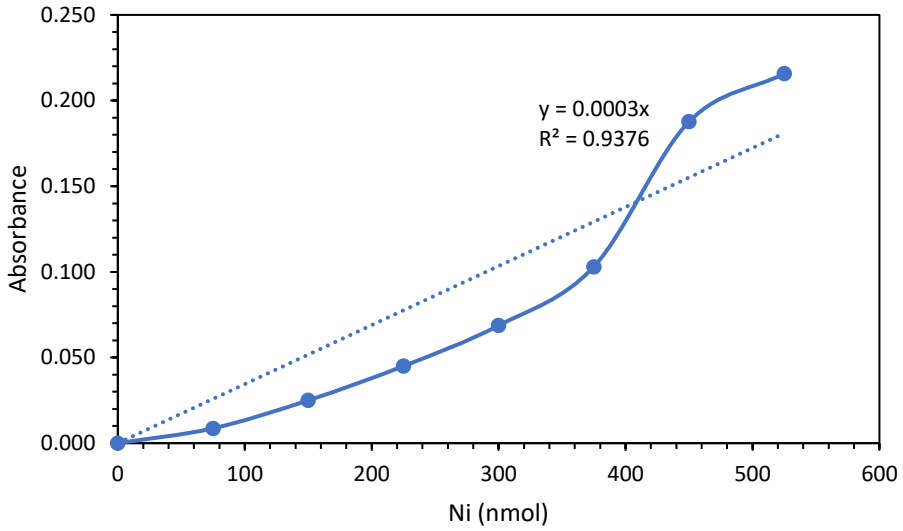

Figure A.5 Nickel standard curve development. Nickel at varying concentrations was applied to the cuvette and topped off with sodium borate until the total volume was 1.5 mL. 75 µL of βME were added to each cuvette and mixed. The absorbance was measured at a wavelength of 405 nm.

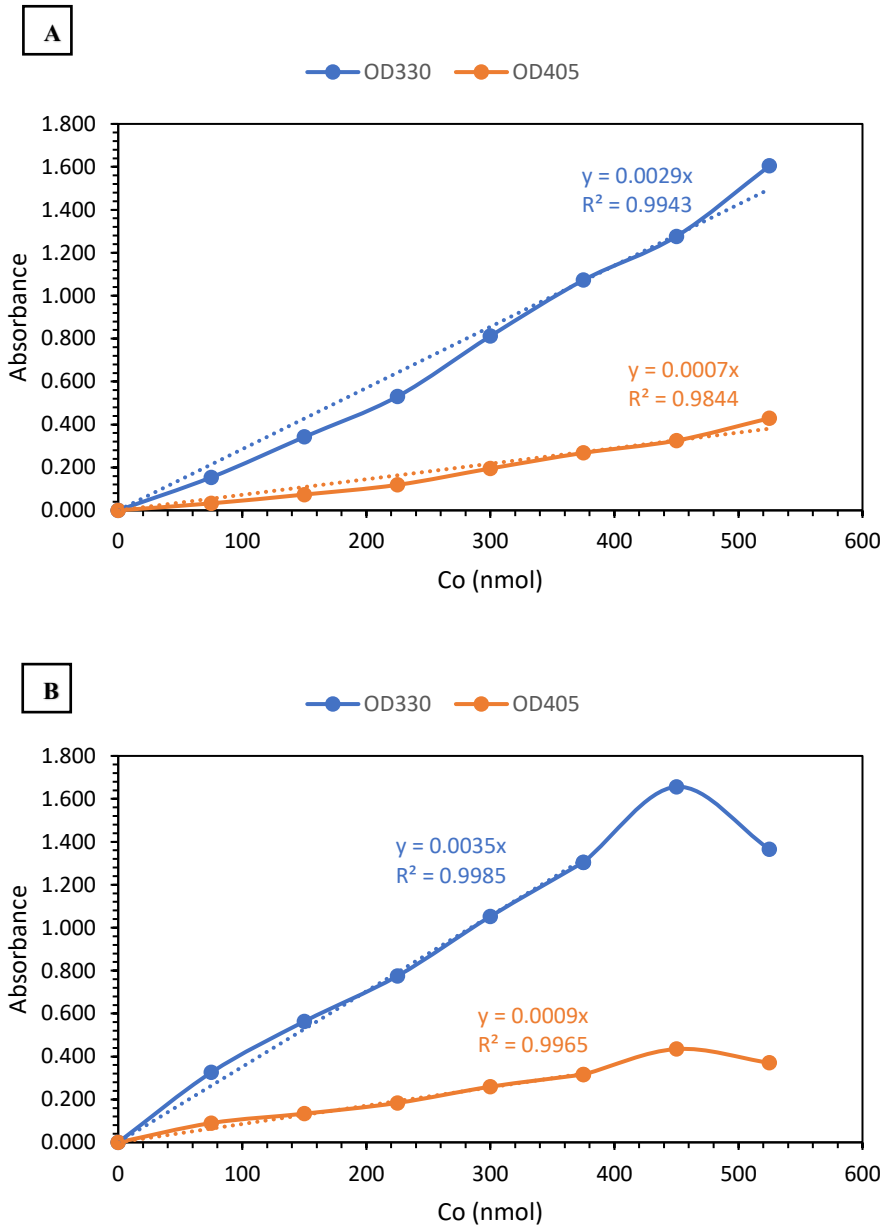

Figure A.6 Absorbance measurements at 330 nm and 405 nm both pre-βME (A) and 30 minutes following βME application (B) with increasing cobalt concentration. Cobalt at varying concentrations was applied to the cuvette and topped off with sodium borate until the total volume was 1.5 mL. 75 uL of βME were added to each cuvette and mixed. Standard curves for the pre-βME and post-BME application best fit a linear curve fit. Above a concentration of 425 nmol Cobalt, the assay was no longer linear.

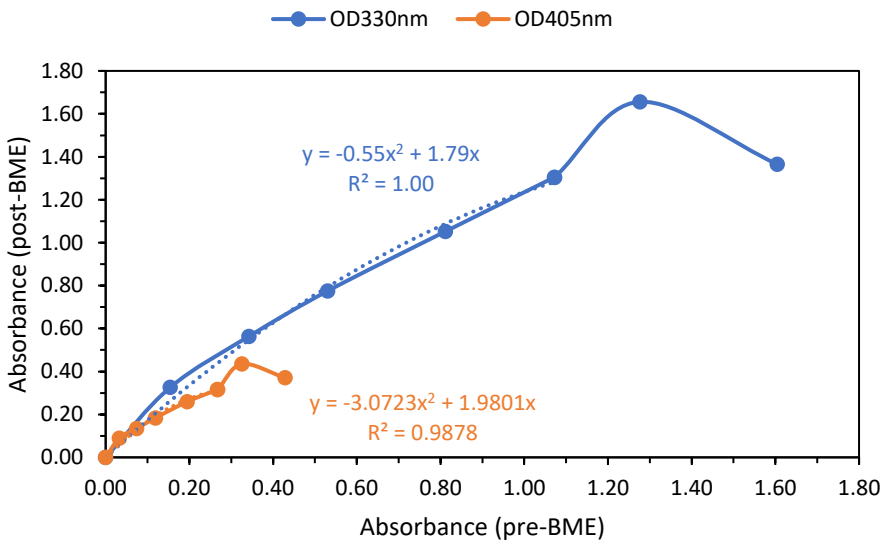

Figure A.7 Coblalt inhibition pre-βME signal plotted against the post-βME signal.

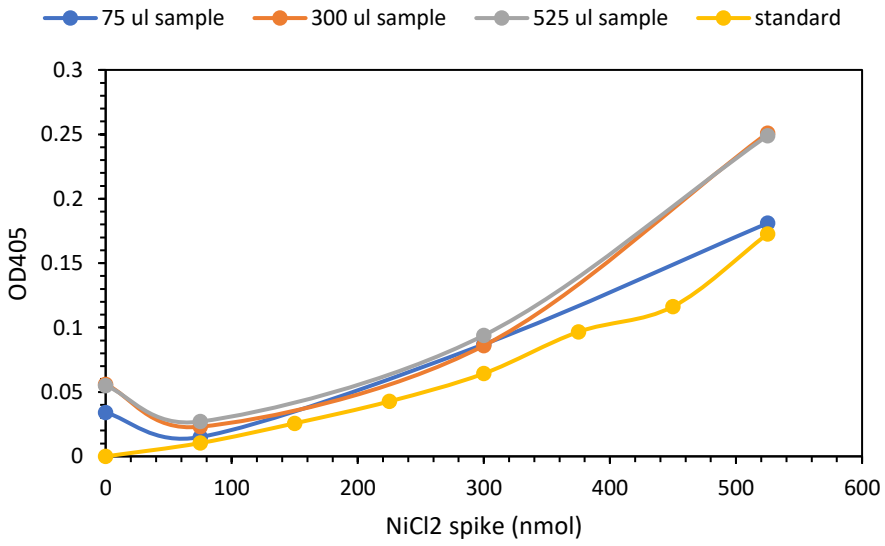

Figure A.8 Nickel spiked leachate samples (OD405). Varying volumes of leachate sample were spiked with $NiCl_2$ standard. The x-axis represents the concentration of the nickel spike, where points plotted at a value of 0.00 nmol do not contain excess nickel. The absorbance was measured at a wavelength of 405 nm. The nickel standard curve is plotted for reference.

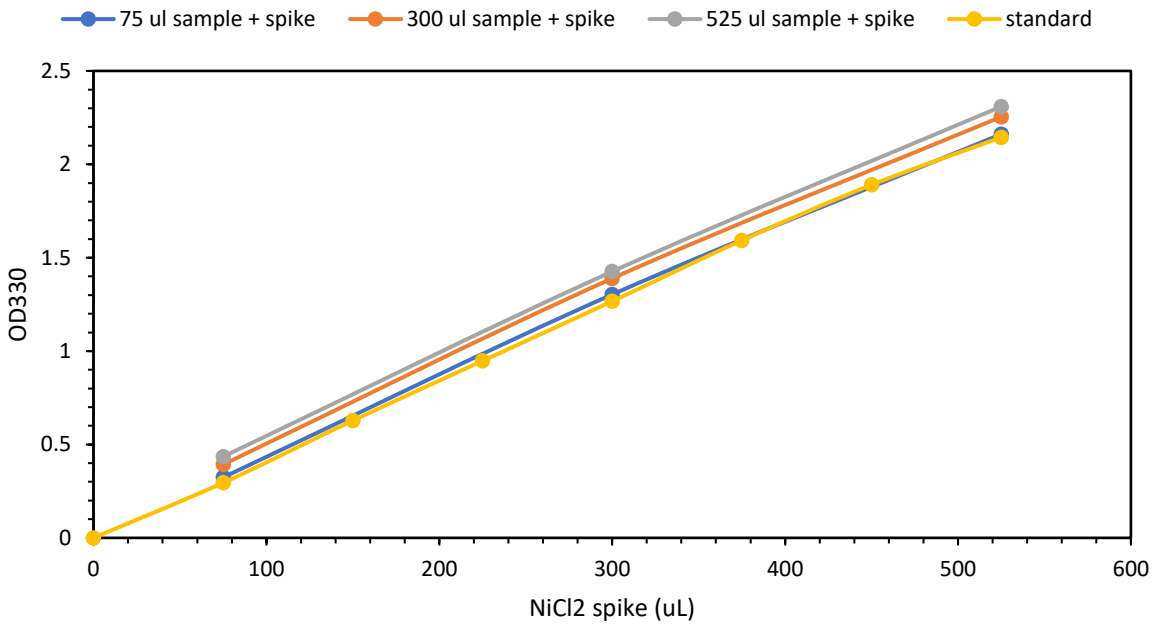

Figure A.9 Awaruite leachate sample 19A spiked Ni results. Varying volumes of leachate sample were spiked with $NiCl_2$ standard. The x-axis represents the concentration of the nickel spike, where points plotted at a value of 0.00 nmol do not contain excess nickel. The absorbance was measured at a wavelength of 330 nm. The nickel standard curve is plotted for reference.

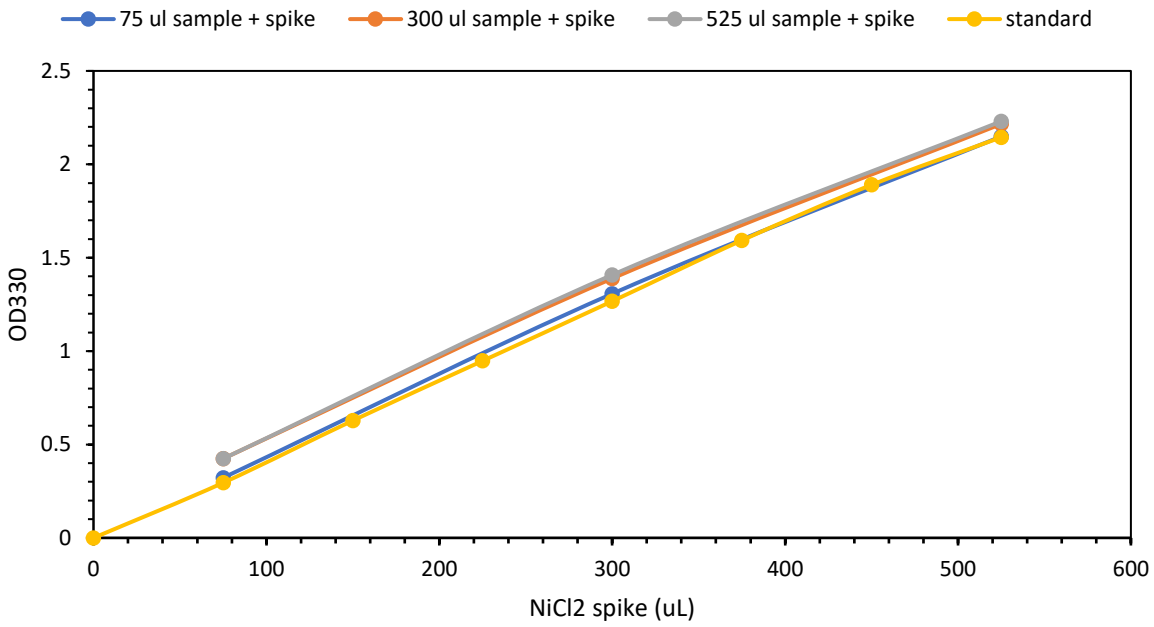

Figure A.10 Sample 20C spiked Ni results. Varying volumes of leachate sample were spiked with $NiCl_2$ standard. The x-axis represents the concentration of the nickel spike, where points plotted at a value of 0.00 nmol do not contain excess nickel. The absorbance was measured at a wavelength of 330 nm. The nickel standard curve is plotted for reference.

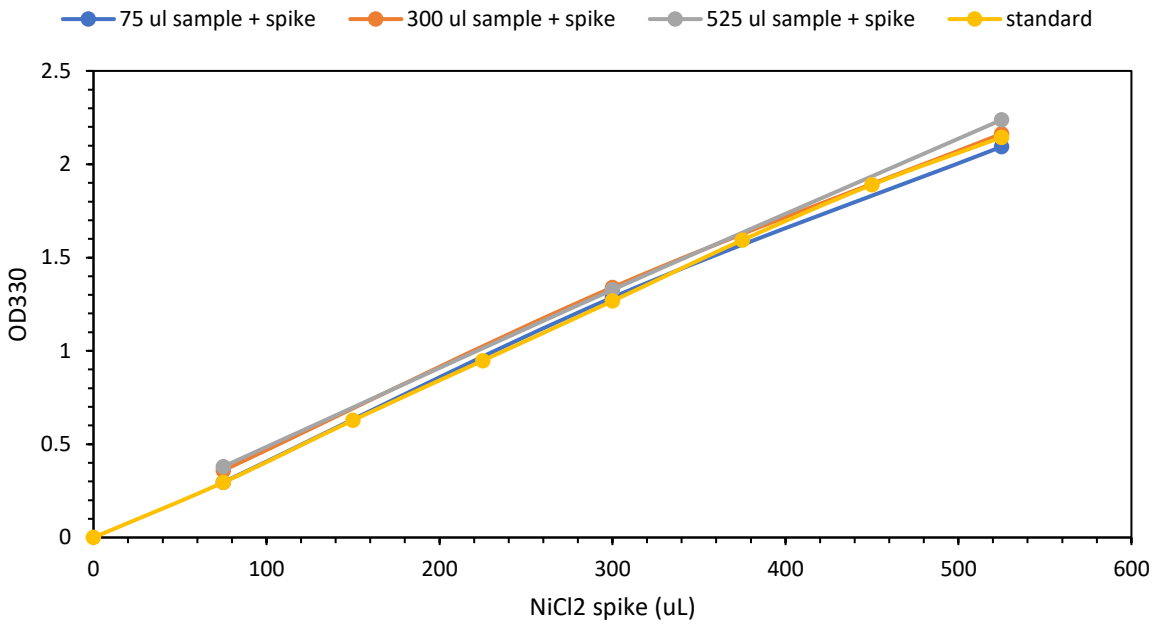

Figure A.11 Sample 4B spiked Ni results. Varying volumes of leachate sample were spiked with $NiCl_2$ standard. The x-axis represents the concentration of the nickel spike, where points plotted at a value of 0.00 nmol do not contain excess nickel. The absorbance was measured at a wavelength of 330 nm. The nickel standard curve is plotted for reference.

Table 9A. pH measurements for traditional leachate samples across leaching conditions investigated. The initial pH measured for the 75 mM and 105 mM standards were 5.97 and 6.03, respectively.

Particle Size (μm)	**Gluconic Acid (mM)**	**Time (days)**	**Average pH**	**pH Error**
75-125	75	0	5.97	0.00
75-125	75	1	7.35	0.05
75-125	75	3	7.36	0.05
75-125	75	5	7.27	0.04
75-125	105	0	6.03	0.00
75-125	105	1	7.24	0.01
75-125	105	3	7.39	0.07
75-125	105	5	7.35	0.01
212-300	75	0	5.97	0.00
212-300	75	1	8.52	0.01
212-300	75	3	8.28	0.01
212-300	75	5	8.18	0.02
212-300	105	0	6.03	0.00
212-300	105	1	8.08	0.01
212-300	105	3	8.12	0.10
212-300	105	5	7.88	0.01
425-500	75	0	5.97	0.00
425-500	75	1	8.70	0.04
425-500	75	3	8.44	0.03
425-500	75	5	8.44	0.04
425-500	105	0	6.03	0.00
425-500	105	1	8.16	0.01
425-500	105	3	8.12	0.12
425-500	105	5	8.01	0.06